Benemérita Universidad Autónoma de Puebla

Facultad de Ciencias Físico Matemáticas

Monte Carlo study of ion collisions from RHIC to LHC energies

Tesis presentada a:

Posgrado en Física Aplicada
de la Facultad de Ciencias Físico Matemáticas

como requisito parcial para obtener el grado de:

Doctor en Ciencias (Física Aplicada)

presenta:

Jesús Ricardo Alvarado García

Asesores:

Dr. Irais Bautista Guzmán (FCFM-BUAP, México),
Dr. Arturo Fernández Téllez (FCFM-BUAP, México)

Puebla Pue.

Julio de 2023

Monte Carlo study of ion collisions from RHIC to LHC energies

Thesis submitted in partial fulfillment of the requirements for the degree

of

Doctor of Philosophy (Applied Physics)

by

Jesús Ricardo Alvarado García
219570427

Under the supervision of

Dr. Irais Bautista Guzmán & Dr. Arturo Fernández Téllez

FACULTAD DE CIENCIAS FÍSICO MATEMÁTICAS

BENEMÉRITA UNIVERSIDAD AUTÓNOMA DE PUEBLA

DECLARATION

Project Title	Monte Carlo study of ion collisions from RHIC to LHC energies
Author	*Jesús Ricardo Alvarado García*
Student ID	219570427
Supervisors	Dr. Irais Bautista Guzmán & Dr. Arturo Fernández Téllez

---

I declare that this thesis entitled *Monte Carlo study of ion collisions from RHIC to LHC energies* is the result of my own work except as cited in the references. The thesis has not been accepted for any degree and is not concurrently submitted in candidature of any other degree.

Jesús Ricardo Alvarado García
219570427

Facultad de Ciencias Físico Matemáticas
Benemérita Universidad Autónoma de Puebla

Date: July 7, 2023

Title: Monte Carlo study of ion collisions from RHIC to LHC energies
Author: Jesús Ricardo Alvarado García

COMMITTEE

President	*Secretary*
Dr. Toscano Chávez, J. Jesús FCFM-BUAP	Dr. Tavares Velasco, Gilberto FCFM-BUAP
Spokesmember	*Supply member*
Dr. Avilez López, Ana Aurelia FCFM-BUAP	Dr. Novales Sánchez, Héctor FCFMP-BUAP
External member	*External member*
Dr. Vergara Quispe, Indira IFLP-UNLP	Dr. Cartas Fuentevilla, Roberto IFUAP-BUAP

Advisors:

Dr. Fernández Téllez, Arturo	Dr. Bautista Guzmán, Irais
FCFM-BUAP	FCFM-BUAP

ACKNOWLEDGEMENTS

I would like to express my deep and sincere gratitude to all the individuals who have accompanied me throughout my scientific journey.

First and foremost, I am grateful to my supervisors, *Dr. Irais Bautista Guzmán* and *Dr. Arturo Fernández Téllez* , who provided me with the opportunity to delve into research work and supported me throughout my academic career. Their guidance and support have been instrumental in shaping my knowledge and skills.

I extend my heartfelt thanks to my professors who witnessed my dynamic growth from an undergraduate student to a graduate student. They have played a crucial role in my understanding of physics, and I express my sincere gratitude to all the professors at the *Facultad de Ciencias Físico Matemáticas* of the *Benemérita Universidad Autónoma de Puebla*.

To my parents, I am immensely grateful for their unwavering love and the sacrifices they made to provide me with education and prepare me for my future. My father, *Pedro Alvarado*, taught me the fundamentals of discipline, while my mother, *Sara García*, taught me the importance of analytical thinking. I also thank my brother, *Eduardo Alvarado*, for his constant support.

I extend my gratitude to all the individuals who directly or indirectly supported me in completing my project work. This includes my colleagues at CERN, my fellow students in physics schools and conferences, and my peers at the faculty. I am grateful to my friends outside the realm of science, as well as my friend, *Ezly*.

I would like to express my special appreciation to *J. E. Ramírez* for our fruitful discussions and valuable advice. I am grateful to *P. Fierro* for accompanying me throughout my academic journey.

Lastly, I want to extend my thanks to *Lizbeth Beciez Bedolla* for her tremendous support and for being an inspiration to me in persevering and moving forward.

Jesús Ricardo Alvarado García
Benemérita Universidad Autónoma de Puebla
Date: July 7, 2023

This work was supported by CONAHCYT under the graduated fellowship grant number 645654.

Contents

ABSTRACT

Attempts to describe nuclear matter under extreme pressure and energy conditions are explored in this work. Different Monte Carlo studies are proposed to study the initial conditions in collisions of ions at relativistic energies where non-perturbative quantum chromodynamics phenomena become relevant.

The structure of the medium formed in heavy ion collisions is examined within a model framework. The analysis focuses on the radial distribution function of the transverse representation of model-dependent color flux tubes, aiming to understand the medium's structure. The findings reveal that the Color String Percolation Model (CSPM) exhibits ideal gas behavior. At the same time, its modified version, known as the core-shell CSPM (CSCSPM), induces a transition from a gas-like to a liquid-like structure. Similarly, the Color Glass Condensate (CGC) framework produces systems that resemble non-ideal gases for AuAu central collisions at RHIC energies and liquid-like structures for PbPb central collisions at LHC energies.

On the other hand, the shear and bulk viscosity to entropy density ratios are calculated in the CSPM framework, the effects of system size, which deviate significantly from the thermodynamic limit, are considered. The results indicate that the interplay between viscosity components suggests a system where the bulk viscosity transitions from a gas-like state to one where fluctuations become more prominent near the critical temperature. This behavior can be interpreted as a non-equilibrium phase transition that characterizes small collision systems. To understand the influence of initial state conditions, a modification of the color reduction factor in the CSPM is considered. A universal global color reduction function is proposed, applicable across proton-proton to nuclear collisions.

The results align with computations from Lattice QCD and Bayesian methods, supporting the notion of a strongly interacting medium formation similar to nuclear collisions but with a phase transition occurring beyond the thermodynamic limit.

Keywords: Quark-Gluon Plasma, Color String Percolation Model, QCD Phase transition, Small Collision Systems, Heavy Ion Collision

RESUMEN

En este trabajo se exploran los estudios sobre la materia nuclear bajo condiciones de presión y energía extremas. Desde simulaciones Monte Carlo se estudian las condiciones iniciales en colisiones de iones a energías relativistas donde los fenómenos de cromodinámica cuántica no perturbativa adquieren relevancia.

La estructura del medio formado en colisiones de iones pesados se examina en el marco de distintos modelos. El análisis se centra en la función de distribución radial de la representación transversal de los tubos de flujo de color dependientes modelo-dependientes. Los hallazgos revelan que el Modelo de Percolación de Cuerdas de Color (CSPM) exhibe un comportamiento de gas ideal, mientras que su versión modificada, llamada CSCSPM induce una transición de una estructura similar a un gas a un líquido. El Color Glass Condensate (CGC) produce sistemas que se asemejan a gases no ideales para colisiones centrales de AuAu a energías de RHIC y estructuras similares a líquidos para colisiones centrales de PbPb a energías del LHC.

Por otro lado, las relaciones de viscosidad sobre densidad de entropía se calculan en el marco del CSPM, se consideran los efectos del tamaño del sistema que se desvían significativamente del límite termodinámico. Los resultados indican que la interacción entre los componentes de la viscosidad sugiere un sistema en el que la viscosidad global sufre una transición de un estado similar al de un gas en el que las fluctuaciones se vuelven más prominentes cerca de la temperatura crítica. Este comportamiento se puede interpretar como una transición de fase en un sistema fuera del equilibrio, como los que caracterizan a los sistemas pequeños que no alcanzan a termalizar. Para comprender la influencia de las condiciones del estado inicial, se considera una modificación del factor de reducción de color en el CSPM. Se propone una función de reducción de color universal, aplicable a desde colisiones protón-protón hasta nucleos pesados.

Los resultados obtenidos son consistentes con los cálculos de Lattice QCD y los métodos bayesianos, lo que respalda la noción de una formación media de interacción fuerte similar a las colisiones nucleares pero con una transición de fase que ocurre fuera del límite termodinámico.

Introduction

High Energy Physics (HEP) searches through the most massive science experiments and attempts to confirm the proposed theories, like The Standard Model of particle physics, one of the field's most valuable successes.

One of the major unsolved problems of modern physics is explaining how the hadrons acquire mass. In the study of this phenom, we found us while the universe was in its earliest stages, the Quark–gluon plasma or QGP, which was theoretically proposed to study the properties of matter under conditions of extreme temperature and pressure (temperatures of hundreds of MeV, of the order of 10^{12} degrees Kelvin), and thus restore approximate symmetries in the theory of strong interactions. This state of matter is studied from the point of view of phenomenological models and with the help of simulations.

Since the 80s, minimal bias proton-proton collisions were used as the basis for comparison, where the absence of QGP was assumed to understand the systems created in nuclear collisions. Recently, the analysis of proton-proton collisions as a function of the number of particles produced per event has revealed new phenomena of collectivity. This fact has given rise to new discussions and proposes a change in the heavy ion paradigm. For this community, it is crucial to understand the origin of the similarities between the systems created in collisions pp, pA, and AA.

To introduce the problem specifically, it is necessary to review the theory behind it; The Standard Model of elementary particles is one of the most important motivations for experiments since it provides a description of the objects that participate in the interactions studied experimentally. On the other hand, the physics behind particle accelerators is necessary for the proposal of effective models that describe the properties of the systems present in hadron collisions since they must be based on direct measurements from experiments; this includes understanding transverse

momentum and multiplicity spectra, particle abundance, as well as correlations between observables. Measurements in proton-proton collisions are required for all experiments and serve as a reference for the correct interpretation of the results coming from collisions between heavy ions. This is why deeply understanding the signals measured in this type of collision is necessary.

In this doctoral thesis, a phenomenological study is carried out through Monte Carlo simulation techniques to study the initial conditions of the medium created in collisions of ions at relativistic energies, where it is expected to find signs of the re-establishment of chiral symmetry.

For this, the thesis is structured as follows: in Chapter I, the theoretical foundations that are a source of motivation for model developments are reviewed. Chapter II presents some of the notable phenomena of non-perturbative QCD, specifically the general aspects of heavy ion physics and the different approaches used to study the phenomena present there, among which I highlight the models of strings. In Chapter III, I describe the color string percolation model, which is the basis of the study of this thesis. In chapter IV, I present the results of the study of the structure of the medium described from certain models; in chapter V, I present the results of the thermodynamic quantities predicted by the model and the respective considerations that I discuss in previous chapters. Finally, a chapter of conclusions is presented.

Chapter 1

Theoretical Fundamentals

1.1 Standard Model

The Standard Model of elementary particles and fundamental interactions describes what is known about the phenomenology of particle physics and is the quantum-relativistic, effective, and renormalizable theory of strong, weak, and electromagnetic interactions; it is built on the basis of the gauge symmetry of the group $SU_C(3) \times SU_L(2) \times U_Y(1)$ which unifies these 3 interactions [1,2]. The gauge group of the Standard Model is divided into three subgroups:

1. For $SU_C(3)$ eight gluonic fields are associated with it G^a_μ.
2. For $SU_L(2)$ three connectors denoted as W^i_μ.
3. For $U_Y(1)$ one is associated with it, the hypercharge field B_μ.

The symmetry group identified as $SU_L(2) \times U_Y(1)$ composed by the Special Unitary matrices of 2×2 with isospin (L) and the hypercharge group (Y) unifies electromagnetic interactions, the Quantum Electrodynamics (QED), and the weak nuclear interactions. The color group, formed by Special Unitary matrices 3×3, denoted as $SU_c(3)$, is the object of study of Quantum Chromodynamics (QCD) that characterizes strong interactions. While gluons mediate the strong interaction, the weak interaction results from the exchange of massive gauge bosons (after the spontaneous symmetry breaking) $W^\pm_\mu$ and Z^0_μ, while the electromagnetic interaction is mediated by the photon field A_μ. Elementary particles are of two types: fermions and bosons.

1.1.1 Fermions

Fermions are the fundamental constituents of matter; they are described as 1/2-spin material particles in the fermionic sector.

- *Leptons*: are light particles classified as:
  - Charged: the electron, the muon, and the tau (e, μ, τ), all with charges $-e$ (minus the fundamental electric charge).
  - Neutrals: the corresponding neutrinos of the electron, muon, and tau $(\nu_e, \nu_\mu, \nu_\tau)$, that are electrically neutral.
- *Quarks*: also classified into two types and differentiating them by their family (flavor) :
  - Type *up*: the quarks *up* (u), *charm* (c), *top* (t), with charge $2e/3$.
  - Type *down*: these are the quarks *down* (d), *strange* (s), *bottom* (b), with charge $-e/3$.

  The stable bound states of quarks (particles composed of quarks) are called hadrons which can be classified into mesons and baryons depending on whether they are grouped into antiquark quark pairs $(q\bar{q})$ for the inns or if they are made up of three quarks (qqq).

Fermions respect the Pauli exclusion principle and are described by the Fermi statistic and the quantization rule given by the anti-commutation rule:

$$\{\psi(\mathbf{r}), \Pi(\mathbf{r}')\} = i\hbar\delta(\mathbf{r} - \mathbf{r}'), \tag{1.1}$$

where $\Pi_\mu = \frac{\partial \mathcal{L}}{\partial(\partial_\mu \psi)}$ is their corresponding conjugate moment.

1.1.2 Bosons

Known as mediating particles of interactions (Fig. 1.1), given according to the exchange in the corresponding interaction, as well as to the quantization of the respective field, they are divided into the gauge bosons (vector) and scalar boson:

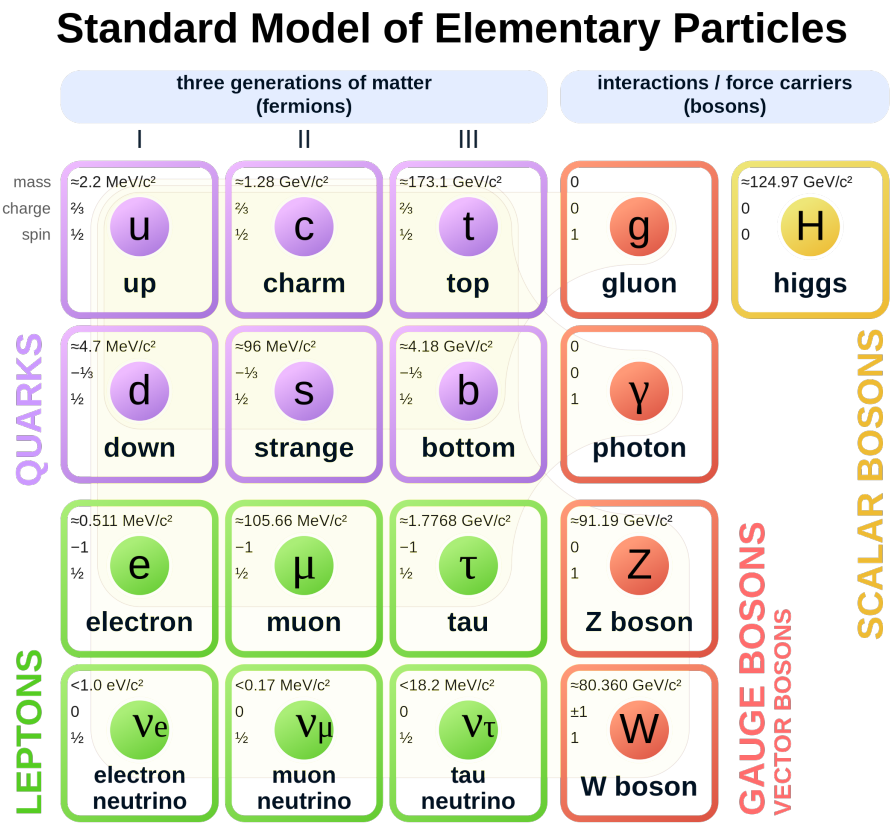

Figure 1.1: Elementary particles according to the Standard Model: the 12 fermions and 5 fundamental bosons. The background of different shades of brown indicates which bosons can be coupled with the different fermions. The image is from public domain.

- The electromagnetic interaction, which is of infinite range produced by the electric charge, is associated with a bosonic field whose boson is the photon, with spin 1.
- A weak nuclear interaction, which is in the range of 10^{-18} m produced by the *weak charge*, is associated with three bosonic fields whose bosons are the W^+, the W^- and the Z^0; all with spin 1.
- To the strong nuclear interaction, which is of range $\leq 10^{-15}$ m produced by the *color charge*, 8 gluon fields are associated with it, and all of them with spin 1.

- The Higgs boson, which is scalar in nature, which gives particles mass through spontaneous symmetry breaking and the Higgs mechanism.

The bosons do not respect the Pauli exclusion principle and are described by the Bose-Einstein statistic and the quantization rule given by:

$$[\phi(\mathbf{r}), \pi(\mathbf{r}')] = i\hbar\delta(\mathbf{r} - \mathbf{r}'), \tag{1.2}$$

where $\pi_\mu = \frac{\partial \mathcal{L}}{\partial(\partial_\mu \phi)}$ is their corresponding conjugate moment.

1.1.3 Gauge Symmetry

As mentioned above, gauge invariance allows us to build the theory. An introductory example is to consider the quantum-relativistic Lagrangian of a free Dirac particle:

$$\mathcal{L} = \bar{\psi}(i\gamma^\mu \partial_\mu - m)\psi, \tag{1.3}$$

if ψ describes the field of a free electron, the gauge transformation we consider is

$$\psi \to \psi' = \exp[iq\alpha(x)]\psi, \tag{1.4}$$

where $\alpha(x)$ is a function, q is the electron charge associated with the gauge group $U(1)$. Then a vector field is considered A_μ associated with the photon, which is transformed:

$$A_\mu \to A'_\mu = A_\mu - \partial_\mu \alpha(x). \tag{1.5}$$

So that the Lagrangian of the equation 1.3 is invariant under these transformations it is introduced D_μ defined:

$$D_\mu = \partial_\mu + iqA_\mu, \tag{1.6}$$

whence the Lagrangian of the electron in QED remains as:

$$\mathcal{L} = \bar{\psi}(i\gamma^\mu D_\mu - m)\psi = \bar{\psi}(i\gamma^\mu \partial_\mu - m)\psi - q\bar{\psi}\gamma^\mu A_\mu \psi, \tag{1.7}$$

what is the free Lagrangian plus an interaction

$$\mathcal{L} = \mathcal{L}_0 - j^\mu A_\mu, \quad j^\mu = q\bar{\psi}\gamma^\mu \psi. \tag{1.8}$$

This suggests that the gauge symmetry determines the interaction. To obtain the complete Lagrangian of QED, the invariant term that describes the free electromagnetic field is introduced:

$$-\tfrac{1}{4}F^{\mu\nu}F_{\mu\nu}, \quad F_{\mu}\nu = \partial_{\mu}A_{\nu} - \partial_{\nu}A_{\mu}. \tag{1.9}$$

the mass term $m_{\gamma}^{2}A^{\mu}A_{\mu}/2$ breaks the group invariance, so the mass of the photon is considered $m_{\gamma} = 0$. So the full QED Lagrangian is:

$$\mathcal{L}_{QED} = -\frac{1}{4}F^{\mu\nu}F_{\mu\nu} + \bar{\psi}(i\gamma^{\mu}D_{\mu} - m)\psi. \tag{1.10}$$

1.2 Quantum Chromodynamics

In 1953 the physicists Murray Gell-Mann and Kazuhiko Nishijima classified particles not only by their charge and isospin but also by their strangeness [3–5], later in 1961, Gell-Mann and Yuval Neeman classified hadrons into groups with similar properties and masses using "octuplets" [6]. Two years later, in 1963, Gell-Mann himself and George Zweig (in addition to Petermann, published a few years later) proposed that the group structure could be explained by the existence of three flavors of small particles within hadrons: the quarks [7–9].

Color quantum numbers are the characteristic charges of the strong interaction and are not involved in electrical interactions. They were discovered as a consequence of the classification of the quark model, when it was appreciated that the baryon Δ^{++} with charge $2e$ and with spin and isospin of $3/2$ required three up quarks, of the same electric charge, with parallel spins and zero orbital angular momentum. For this reason, the baryon Δ^{++} could not have an antisymmetric wavefunction[1] unless there was an additional quantum number. In 1965 this problem was solved when Oscar Greenberg suggested that quarks have one more degree of freedom, later called color charge and that quarks interact via an octet of vector gauge bosons, the gluons, which is the theory that is used today [10–12].

QCD assigns a color state to each quark, which must be conserved during strong interactions; the quantum states for quarks are (red, blue, and green), while for antiquarks, they are (anti-red, anti-blue, and anti-green). Hadrons should be colorless,

[1] The quantum numbers considered at that time occupied the same value, which is not allowed by the Pauli exclusion principle.

achieved by combining the colors of the quarks that compose it; for example, a meson can contain red and anti-red quarks to produce a neutral color. The typically named "baryon" is made up of the three quarks in their red, blue, and green states, whose total vector sum also forms the neutral color [13].

The dynamics of quarks and gluons are controlled by the Lagrangian of QCD after the spontaneous symmetry breaking and Higgs mechanism that give mass to the quarks

$$\mathcal{L}_{\text{QCD}} = \sum_f \bar{\psi}_j^{(f)} \left(i(\gamma^\mu D_\mu)_{jk} - m_f \delta_{jk} \right) \psi_k^{(f)} - \frac{1}{4} G_{\mu\nu}^a G_a^{\mu\nu}, \tag{1.11}$$

where $\psi(x)^{(f)}$, are triplets in the fundamental representation of the gauge group $SU(3)$ and represent the fields of the different flavors of quarks ($f = u, d, s, c, t, b$), the components of the triplet correspond to the independent addresses in the color space, which are indexed by j, k; D_μ is the covariant derivative of the group; γ^μ are Dirac matrices that connect the spinor representation with the vector representation of the Lorentz group [14]. Analogous to the electromagnetic field strength tensor, $F_{\mu\nu}$, the symbol $G_{\mu\nu}^a$ represents the intensity tensor of the gluonic field, which is given by:

$$G_{\mu\nu}^a = \partial_\mu \mathcal{A}_\nu^a - \partial_\nu \mathcal{A}_\mu^a + g_s f^{abc} \mathcal{A}_\mu^b \mathcal{A}_\nu^c, \tag{1.12}$$

where $\mathcal{A}_\mu^a(x)$ are the eight fields associated with each gluon in the attached representation of the group $SU(3)$, indexed by $a, b, \ldots$; y f^{abc} are the structure constants of $SU(3)$. The rules for raising or lowering the color index a, b, or c are trivial $(+, \cdots, +)$ so that $f^{abc} = f_{abc} = f_{bc}^a$, while for the indices μ o ν, we have the relativistic rules corresponding to the metric of flat Minkowski space-time $(+, -, -, -)$. Variables m_f y g_s correspond to the masses of the quarks and the coupling constant of the theory, respectively [14]. The gauge transformations of these objects are:

$$\begin{aligned} \psi_j^{(f)} \to \psi'^{(f)}_j &= \exp[i g_s \alpha^a(x) T_a] \psi_j^{(f)}, \\ \mathcal{A}_\mu^a \to \mathcal{A}'^a_{\mu\nu} &= \mathcal{A}_{\mu\nu}^a - \partial_\mu \alpha^a(x) - g_s f_{bc}^a \alpha^b(x) \mathcal{A}_\mu^c, \end{aligned} \tag{1.13}$$

together with the covariant derivative:

$$D_\mu = \partial_\mu + i g_s T_a \mathcal{A}_\mu^a, \tag{1.14}$$

where T_a are the generators of $SU(3)$, arrays 3×3 null trace satisfying Lie algebra $[T_a, T_b] = i f_{abc} T_c$ [14]. At this level, the most relevant difference between QCD and

QED is that the gauge group $SU(3)$ is non-abelian, unlike $U(1)$, the fact that is reflected in the construction of the curvatures $G^a_{\mu\nu}$ and $F_{\mu\nu}$, this difference is crucial to describe the behavior of the coupling constants theoretically.

1.2.1 Asymptotic freedom and confinement

Asymptotic freedom is a fundamental property in non-abelian gauge theories, where the interactions between particles become asymptotically weaker as the energy scale increases and the corresponding length scale decreases.

Asymptotic freedom in QCD was discovered in 1973 by David Gross and Frank Wilczek [15], and independently by David Politzer in the same year [16]. This phenomenon implies that in high-energy scattering, quarks move within hadrons as free particles that do not interact. Quarks interact weakly at high energies, so perturbative calculations are useful on this scale; However, the confinement of quarks and gluons within hadrons is a phenomenon that occurs at low energies, so its study involves non-perturbative QCD tools. The variation of the intensity

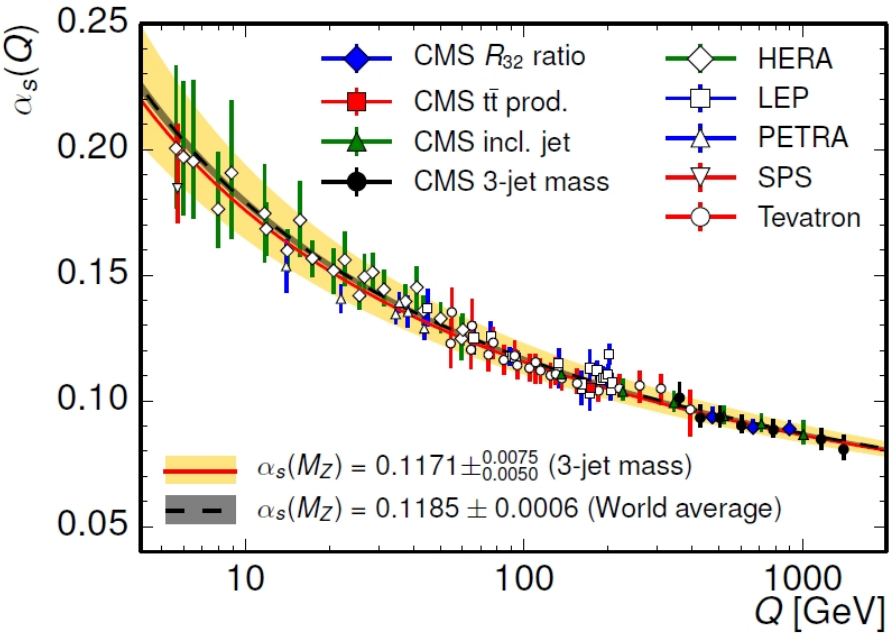

Figure 1.2: Behavior of the strong coupling constant according to the measurement of the inclusive cross section in production of 3-*jet* in collisions pp to 7 TeV [17] .

of the interactions under variations of scale can be understood qualitatively as the

effect of the excitation of the quantum vacuum, from which interacting particles emerge, decreasing or increasing this intensity; that is, in the vicinity of a charge, the vacuum becomes polarized: virtual particles of opposite charge are attracted to the charge and virtual particles of similar charge are rejected. Thus, the field is partially canceled at any finite distance. The effect of the vacuum decreases, and the effective charge increases as we get closer to the source. In QCD, virtual quark-antiquark pairs appear, which tend to shield the color charge (classically, the effective potential energy of this effect is the Yukawa potential and is given by: $V(r) = -\frac{g_s}{4\pi r} e^{\frac{mcr}{\hbar}}$). However, an additional fact does not exist in QED: the force-carrying particles, gluons, have a color charge. Each gluon carries a charge of the color and an anti-color charge (of a different color). The net effect of virtual gluon polarization in a vacuum is not to shield the field but to increase it and affect its color. Approaching a quark decreases the effect of *anti shielding* of the surrounding virtual gluons; therefore, the contribution of this effect is to weaken the effective color charge of a quark with a decrease in distance.

Since virtual quarks and virtual gluons contribute opposite effects, the prevailing effects depend on the number of flavors of quarks. Because there are 3 known families of quarks (and no more than 8, which would facilitate matching these contributions), anti-shielding prevails and the theory is asymptotically free.

The coupling constant g is a number that determines the intensity of an interaction. The Callan-Symanzik beta function, $\beta(g)$, determines the variation of the coupling constant and is defined by the relation:

$$\beta(g) = \mu \frac{\delta g}{\delta \mu}, \tag{1.15}$$

where μ is the energy scale of a physical process given [18–20][2], the coupling constant of QCD decreases logarithmically at high energies, which can be observed from the solutions to different orders of the equation in terms of $\alpha_s = g^2/4\pi$ [21]:

$$\frac{da}{d \ln \mu^2} = \beta(a) = -\sum_{n=0}^{\infty} \beta_n a^{n+2}, \quad a = \frac{\alpha_s(\mu)}{4\pi}. \tag{1.16}$$

[2]The mass of the boson is regularly used Z^0, M_Z, to define the renormalization scale from where the coupling starts to vary.

Depending on the number quarks $n_f = 6$, the first terms of the beta function are [20–22]:

$$\beta_0 = 11 - \frac{2}{3}n_f, \quad \beta_1 = 102 - \frac{38}{3}n_f, \quad \beta_2 = \frac{2857}{2} - \frac{5033}{18}n_f + \frac{325}{54}n_f^2,$$

$$\beta_3 = \tfrac{149753}{6} + 3564\zeta_3 - \left(\tfrac{1078361}{162} + \tfrac{6508}{27}\zeta_3\right) n_f + \left(\tfrac{50065}{162} + \tfrac{6472}{81}\zeta_3\right) n_f^2 + \tfrac{1093}{729}n_f^3, \tag{1.17}$$

where $\zeta_3 \cong 1.202056903$ denotes Riemann zeta function evaluated at 3. The behavior of the coupling constant in QCD is mainly due to the presence of self-interactions of the gauge bosons. This behavior of the coupling constant implies the two most important properties of QCD. For high values of transferred moment $Q^2 \sim \mu^2$, the coupling constant becomes small; this gives the property of asymptotic freedom. The coupling constant diverges for small values of Q^2. This qualitative property is known as "color confinement" and is the reason why we can never observe free quarks and gluons in nature, instead, they form "singlets" of color known as hadrons. As this feature is not fully understood from an analytical point of view, there are different methods that describe different domains of QCD. At small distances (high values of Q^2), perturbative QCD (pQCD) methods can be applied, while phenomenological models are used at long distances (Q^2 little). An example in non-perturbative QCD is the numerical calculations in Lattice QCD, which allowed us to know the mass of the hadrons [23], where it is shown that more than 95% of the mass of a hadron is due to the strong interaction and not to the masses of the quarks that constitute them.

1.2.2 Symmetries in QCD

In addition to the aforementioned gauge symmetry, there are various symmetries in QCD that give rise to relevant phenomena within the heavy ion area.

1.2.2.1 Isoespin Symmetry

When considering the Lagrangian of QCD for light quarks u and d, we see that if the masses of the two quarks were equal, $m_u = m_d$, the Lagrangian of QCD would be invariant under the transformations.

$$\begin{array}{l} u \to \alpha u + \beta d, \\ d \to \gamma u + \delta d, \end{array} \quad \text{Det}\begin{pmatrix} \alpha & \beta \\ \gamma & \delta \end{pmatrix} = \text{Det}V = 1, \tag{1.18}$$

namely, $V \in SU(2)$. u and d form an isospin doublet (the rest of the quarks s, c, b, t are isoespin singlets). Actually, $m_u < m_d$, and the isospin group is only approximate symmetry. The piece of the Lagrangian that breaks symmetry is the mass term, which we can write

$$m_u \bar{u}u + m_d \bar{d}d = \frac{1}{2}(m_u + m_d)(\bar{u}u + \bar{d}d) + \frac{1}{2}(m_d - m_u)(\bar{d}d - \bar{u}u) \tag{1.19}$$

The member's first term to the right of Eq. 1.19 is invariant under $SU(2)$, but the second term breaks the symmetry. The mass difference $m_d - m_u$ plays the role of breaking the parameter of symmetry. The existence of nearly degenerate isospin multiplets implies that the second term is a small disturbance and, therefore the difference $m_d - m_u$ is small. The invariance of the strong interactions against the isospin in QCD is explained by the fact that the difference between the masses of the quarks u and d it is almost nil.

1.2.2.2 Chiral Symmetry

In considering the case where $m_u = m_d = 0$, not only is an invariance obtained against isospin symmetry but also with respect to chiral transformations [24], that is, isospin independent rotations of the positive (right) and negative (left) helicity components of u y d.

$$\begin{pmatrix} u_R \\ d_R \end{pmatrix} \to V_R \begin{pmatrix} u_R \\ d_R \end{pmatrix}, \quad \begin{pmatrix} u_L \\ d_L \end{pmatrix} \to V_L \begin{pmatrix} u_L \\ d_L \end{pmatrix}, \quad V_R, V_L \in SU(2). \tag{1.20}$$

The corresponding symmetry group is the direct product of the two isospin groups $SU(2)_L \times SU(2)_R$. The group generators are the three ordinary isospin operators $\vec{I}$ plus the three chiral isospin operators $\vec{I}_5$. Both the components of $\vec{I}(I^+, I^-, I^3)$ as the $\vec{I}_5(I_5^+, I_5^-, I_5^3)$ they are conserved. Within this context, it is verified that:

1. Energy levels form degenerate multiplets, resulting in multiplets of hadrons of equal mass.

2. Operators $\vec{I}$ generate transitions within multiplets, for example a neutron $|n\rangle$ is transformed into a proton $|p\rangle$ for I^+, $I^+|n\rangle = |p\rangle$.

3. The fundamental state $|\Omega^-\rangle$ (Ω^- is composed of three quarks s) is a singlet of isospin, $\vec{I}|\Omega^-\rangle = 0$.

If chiral symmetry is respected, the states must be grouped into degenerate multiplets of the group $SU(2)_L \times SU(2)_R$. Like operators $\vec{I}_5$ carry negative parity, multiplets should contain members with opposite parity, but there is no evidence that this occurs in nature. In general, if a transformation S of a group leaves the void invariant, that is, $S|\Omega\rangle = |\Omega\rangle$,

$$S|\Omega\rangle = e^{i\epsilon Q}|\Omega\rangle \simeq (1 + i\epsilon Q)|\Omega\rangle = |\Omega\rangle, \tag{1.21}$$

and therefore $Q|\Omega\rangle = 0$. But in our case, $\vec{I}|\Omega\rangle = 0$ and $\vec{I}_5|\Omega\rangle \neq 0$, so we say that the vacuum breaks the symmetry, or that the symmetry is spontaneously broken. Then, as the Hamiltonian of QCD commutes with the generators $\vec{I}_5$, the three states $\vec{I}_5|\Omega\rangle$ have the same energy as a vacuum, $\vec{I}_5$ it takes no time and $|\Omega\rangle$ has zero moment, then there must be three particles with zero mass, which is a fact due to the theorem of Goldstone [25] which says that, in general, spontaneous symmetry breaking gives rise to the same number of non-massive particles (Goldstone bosons) as generators of the broken symmetry group. The quantum numbers of $\vec{I}_5|\Omega\rangle$ will be zero spin, negative parity and $I = 1$, that matches the set (π^+, π^0, π^-), so it is natural to identify

$$I_5^+|\Omega\rangle = |\pi^+\rangle, \quad I_5^3|\Omega\rangle = |\pi^0\rangle, \quad I_5^-|\Omega\rangle = |\pi^-\rangle. \tag{1.22}$$

Given the $m_u, m_d \neq 0$, the chiral symmetry of the Lagrangian of QCD is broken so that the Hamiltonian can be written as an invariant part H_0 and the term with masses that breaks the symmetry:

$$\begin{gathered} H = H_0 + H_{sb}, \quad H_{sb} = \int d^3x (m_u \bar{u}u + m_d \bar{d}d), \\ \text{where} \qquad\qquad [H_0, \vec{I}] = 0 = [H_0, \vec{I}_5], \end{gathered} \tag{1.23}$$

since chiral symmetry only involves quarks u and d, the rest of the quarks are singlets, and their corresponding mass terms are in H_0.

1.2.2.3 Scale Symmetry

When considering transformation

$$x \to \lambda x, \quad \psi_j^{(f)} \to \lambda^{3/2}\psi_j^{(f)}, \quad \mathcal{A}_\mu^a \to \lambda \mathcal{A}_\mu^a, \tag{1.24}$$

We find that the Lagrangian of QCD is invariant except only for the mass term of the quarks, so it is part of the set of approximate symmetries of QCD [26, 27]. This approximate scale symmetry is respected at the classical level, but it breaks due to quantum corrections, since the renormalization process involves a scale [26, 27]. By Noether's theorem, we know that any continuous transformation defines an associated current, and we know that if this transformation is a symmetry, the corresponding current is conserved. The current associated with the scale transformations can be calculated 1.24, giving as resulting [28]:

$$\partial_\mu s^\mu = T^\mu_\mu = \frac{\beta(g_s)}{2g_s^3} G^a_{\mu\nu} G^{\mu\nu}_a + [1+\gamma(g_s)] \sum_f m_f \delta_{jk} \bar{\psi}^{(f)}_j \psi^{(f)}_k \tag{1.25}$$

where $\gamma(g_s)$ is the anomalous dimension acquired by the mass of the quarks in the renormalization process, and the function $\beta(g_s)$ defined in section 1.2.1, A which indicates how the coupling constant varies. The second term in the equation 1.25 shows what is expected: quark masses explicitly break the symmetry. The first term, however, is unexpected: it shows that the scale invariance is also broken by the fact that the function β of QCD is not zero. The function β it is an intrinsic quantum effect, and this result illustrates that the scale symmetry is anomalous; it is an approximate symmetry of the classical theory that is explicitly broken by fluctuations of the quantum vacuum of QCD.

The trace of the energy tensor moment of matter, T^μ_μ, plays a very important role at finite temperature near the QCD phase transition. In a broader context, the elements of the energy-moment tensor trace are the observable characteristics of a fluid from the hydrodynamic description since the expected value of its components is related to the thermodynamic observables in the macroscopic limit [29]:

$$\sum_i \langle T_{ii} \rangle = 3P, \quad \langle T_{00} \rangle = \varepsilon, \tag{1.26}$$

with ε energy density and P the pressure. The expected value of the trace of the energy-moment tensor of QCD provides a thermodynamic description of the systems that reach the phase transition, or in other words, this observable characterizes the collective properties that are appreciated in these systems since:

$$\left\langle T^\mu_\mu \right\rangle = \varepsilon - 3P, \tag{1.27}$$

the behavior of this quantity shows a maximum in the critical temperature region, so it is a quantity very sensitive to the phase transition between hadronic matter and deconfinement [29], the collective properties of these systems will be discussed in detail in subsequent chapters.

Chapter 2

QCD Matter

In 1974, T. D. Lee and G. Wick proposed the possibility of finding new physics by distributing the nuclear matter energy density in a finite volume; in this way, it would be possible to restore broken symmetries of the physical vacuum and create new abnormal states of dense nuclear matter [30]. Asymptotic freedom in QCD was found to imply the existence of a very dense form of nuclear matter made up of deconfined quarks and gluons [31–33], which was later called Plasma of Quarks and Gluons [34]. You can understand the phase transition between ordinary nuclear matter and a "gas" quarks and free gluons as a change in the number of degrees of freedom [35], between a free hadron gas (HG) to $T \ll T_c$ and a gas of quarks and free gluons for $T \gg T_c$:

$$\begin{aligned} \varepsilon_{\mathrm{HG}} &= \frac{\pi^2}{30} 3T^4 \simeq T^4 \\ &\Downarrow \\ \varepsilon_{\mathrm{QGP}} &= \frac{\pi^2}{30}\left[2\times 8+\frac{7}{8}\times 2(3)\times 2\times 2\times 3\right] T^4 = \frac{\pi^2}{30}\left[16+21(31.5)\right] T^4. \end{aligned} \tag{2.1}$$

For the energy density of a Hadron gas ($\varepsilon_{\mathrm{HG}}$), The Bose-Einstein statistic was considered, where factor 3 corresponds to the three states of the pions (π^+, π^0, π^-) despising their masses. On the other hand, in the energy density of the QGP ($\varepsilon_{\mathrm{QGP}}$), the 8 color states of the gluons were considered, each of them with 2 possible states of helicity, and 2 (3) classes of quarks and antiquarks, each of them with two spin states and 3 colors. The 7/8 factor is due to the fermionic character of quarks and antiquarks.

Rough estimates of the energy density achieved in central nuclear collisions (AA with impact parameter $b = 0$), using Bjorken's formula [36]

$$\varepsilon = \frac{\langle p_T \rangle \left. \frac{dN}{dy} \right|_{\eta=0}}{\tau_0 \pi R_p^2 A^{2/3}}, \tag{2.2}$$

for a while τ_0 =1 fm/c after the collision, at the highest energies studied at CERN's Proton Supersynchrotron (SPS) and at BNL's Relativistic Heavy Ion Accelerator (RHIC), for collisions PbPb y AuAu respectively, find values above the critical energy density for the phase transition obtained in Lattice QCD [37, 38]:

$$\varepsilon_c \approx 0.5 \, \text{GeV/fm}^3. \tag{2.3}$$

2.1 Lattice QCD and phase diagram

In the finite temperature network of QCD (Lattice QCD), the deconfinement order parameter is provided by the vacuum expectation value of the *loop* from Polyakov $L(\vec{x})$ defined in Euclidean space

$$L(\vec{x}) = \text{Tr} \prod_{t=1}^{N_t} A_4(\vec{x}, t), \tag{2.4}$$

$L(\vec{x})$ is the ordered product of the temporal gauge variables of $SU(3)$, $A_4(\vec{x}, t)$, in a fixed spatial position, where N_t, is the number of points of the network in the direction of time and Tr denotes the trace over the color indices [39]. The *loop* Polyakov corresponds to a static source of quarks, and its vacuum expectation value is related to free energy F_q single quark

$$L(\vec{x}) \propto \exp\left(-F_q/T\right). \tag{2.5}$$

Below the critical temperature, T_c, quarks are confined y F_q is infinite, which implies $\langle L(\vec{x}) \rangle = 0$. In an unconfined environment F_q becomes finite, therefore for $T > T_c$, $\langle L(\vec{x}) \rangle \neq 0$. Chiral symmetry breaking is controlled by chiral condensate $X(T) \equiv \langle \bar{\psi}\psi \rangle \propto M_q$, which measures the masses of the constituent quarks obtained from a Lagrangian with massless quarks. At high temperatures, this mass is "melted", therefore

$$\begin{aligned} X(T) &> 0, \quad T < T_x, \\ X(T) &= 0, \quad T > T_x. \end{aligned} \tag{2.6}$$

T_x defines another critical temperature so that for $T > T_x$, it is possible to reestablish the broken symmetries due to the presence of the masses in the Lagrangian of QCD [29,39]. The corresponding derivatives with respect to T from $\langle L \rangle$ and X, the susceptibilities have been studied in Lattice at finite temperature in a low baryon number, showing a sharp peak that defines respectively T_c and T_x, that, within the errors, coincide. The reported value of T_c it is 154±9 MeV [40–42].

A phase transition in the strict sense of Statistical Mechanics requires a discontinuity in the energy density or in one of its derivatives at the limit of infinite volume. Based on the calculations in Lattice QCD, the phase transition to QGP appears to be a *cross-over*, that is, a rapid change without discontinuity, although this conclusion has a strong dependence on the number of flavors introduced and the value of the masses. The energy density has been studied in detail in Lattice, with 2 and 3 light flavors, or in the most realistic case, $2 + 1$ flavors, two light and one heavy. These results show that energy density grows rapidly from an initial low-density state to saturation in a high-density region, as would be expected in such a phase transition [39]. As we will see in later chapters, Lattice predicts energy density values below those of Eq. 2.1, for $T/T_c = 1/3$; this indicates that only at temperatures much higher than the critical temperature will the almost free QGP that predicts the asymptotic freedom of QCD be obtained, for moderate temperatures, Lattice QCD points to a QGP with strong residual interactions (called sQGP). Many of the properties of the system, determined by the equation of state, behave similarly to what would occur in a strict phase transition. In particular, in the phase transition, the pressure shows a continuous increase without abrupt change, increasing slowly in a region where the energy density increases by an order of magnitude. The speed of sound $c_s^2 = dP/d\varepsilon$, is very low in that region (as we will see later). This fact, the "smoothing" of the equation of state around the phase transition, is a key fact to study when a collective flow of the system occurs when the Plasma expands.

Calculations in Lattice QCD suggest that QCD could have a first-order phase transition for high baryon densities μ_B and low temperature, while at high temperature and low baryon density, it would be the *cross-over* already mentioned. Therefore, a critical point must be indicated in Fig. 2.1. In this region of QCD, the masses of the quarks can be neglected (u, d, s), and the system has chiral symmetry, despite the fact that both quarks and gluons acquire collective masses, $m \sim g_s T$. At temperatures below the critical temperature, the quarks and gluons are confined

in the hadrons, and the chiral symmetry of QCD breaks spontaneously. In this way, the QGP search [43] is important not only because it is the form of the high temperature or high baryon density QCD matter that was present during the first microseconds after the *Big-Bang* and that it can exist in neutron stars, but because it provides us with information about the origin of most of the ordinary mass and about the confinement of quarks and gluons.

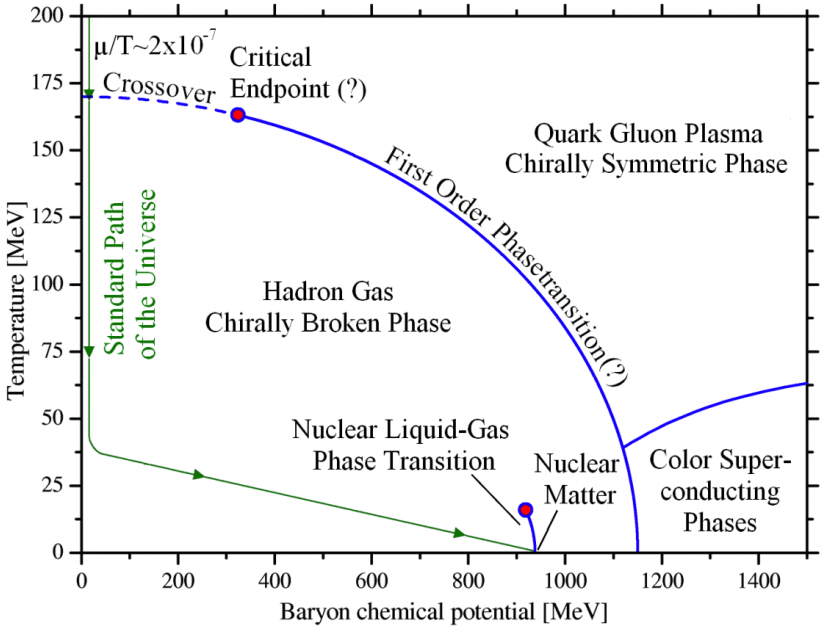

Figure 2.1: Schematic of the possible phase diagram in QCD of [44].

The best description of the system is currently being sought, which implies having a phase diagram in QCD as detailed as possible. Fig. 2.1 exposes the fundamental ideas in a schematic way, the regions explored by the experiments and what is described by the simulations in Lattice QCD are illustrated; It should be mentioned that for the dates in which this work is presented, the critical point has not yet been found.

2.2 Heavy ion collisions

The simple description of a nuclear collision at the LHC is as follows: a pair of heavy nuclei hurtle towards each other, circling in opposite directions around the 27-kilometer ring of the LHC. Stripped of their electrons, the positively-charged ions have been accelerated to nearly the speed of light by the collider's powerful electromagnetic field. Due to relativistic length contraction, they resemble nearly-flat disks.

Upon collision, the disks collide, transferring their kinetic energy to a nucleus-sized area and generating temperatures of approximately $T \sim 300$ MeV, equivalent to about 3×10^{12} K—over 100,000 times hotter than the core of the Sun (1.6×10^{7} K). Approximately 1 fm/c (femtosecond per speed of light) after the collision, the quarks and gluons that originally constituted the protons and neutrons within the lead nuclei have broken free, forming an extremely hot and dense state of matter with fluid-like properties known as the QGP.

Previously mentioned, QCD suggests that its constituents become deconfined under conditions of high temperatures and density. In the modern era, superdense celestial objects like neutron stars potentially harbor a phase similar to the QGP, yet their remote location from Earth poses challenges in studying them comprehensively. In laboratory settings, high-energy nuclear collisions serve as the sole means to replicate such extreme conditions. The idea of conducting these collisions to explore a state characterized by free quarks and gluons, hot and dense, traces back to the 1970s.

In a high-energy collision involving heavy nuclei, the Lorentz-contracted nuclei move away from each other along the z-axis, leaving behind a created droplet of QGP. Bjorken provided a fundamental description of the spacetime evolution of these collisions in 1982. The QGP is initially located near the origin and expands hydrodynamically in both the transverse $(x - y)$ plane and the longitudinal (z) direction. At any given position along the z axis, the fluid exhibits an approximate longitudinal velocity of z/t. As the nuclei continue to move apart, the fluid forms at later times at locations further away from $z = 0$, approximately following the trajectory of a spacetime hyperbola determined by a constant "proper time".

$$\tau \equiv \sqrt{t^2 - z^2} \sim 1 \text{ fm/c}. \tag{2.7}$$

The counterpart to proper time is the spacetime rapidity, denoted as η_s, which is defined as:

$$\eta_s \equiv \frac{1}{2} \log \left(\frac{t+z}{t-z} \right). \tag{2.8}$$

This variable determines the position along the hyperbolic trajectories of proper time. Spacetime rapidity is a useful kinematic quantity as Lorentz boosts simply combine when expressed in terms of rapidity. In other words, a boost of η_s^A followed by a subsequent boost of η_s^B is equivalent to a single boost of $\eta_s^A + \eta_s^B$.

The system exhibits approximate Lorentz boost invariance near central rapidity ($\eta_s \sim 0$) due to the extreme boosts of the nuclei (Lorentz factor $\gamma > 1000$ at the LHC) according to Bjorken's argument. This implies that the collision dynamics appear similar in all near-center-of-mass frames, resulting in a central plateau structure in the density distribution with respect to rapidity. Additionally, particle production remains constant per unit rapidity within the plateau region. This approximation, known as "boost-invariance," is supported by experimental data, as demonstrated in the following section, and serves as a crucial simplification for hydrodynamic models.

As the QGP expands and cools down, the strong force rapidly becomes dominant, leading to the recombination of quarks and gluons into hadrons. Recent calculations indicate that this conversion occurs through a crossover phase transition around $T \sim 145$–165 MeV at zero net baryon density, where the matter and antimatter components are in equal proportions. Simultaneously, a first-order phase transition occurs from normal nuclear matter to a color superconductor at zero temperature and high baryon density.

Drawing on these insights, the schematic phase diagram of QCD, as presented in the previous section, begins to take shape and align with (2.1).

Following the established convention, the phase diagram is depicted as a function of temperature T and baryon chemical potential μ_B, which represents the net baryon density, where positive μ_B indicates an excess of baryons over antibaryons. Given the observed crossover at zero μ_B and the first-order transition at zero temperature, it is natural to represent the phase boundary as a first-order transition terminating at a critical point corresponding to a specific combination of (T, μ_B). However, the existing experimental evidence for the presence of a QCD critical point remains inconclusive.

Our understanding of the crossover phase transition at zero μ_B is primarily derived from lattice QCD calculations of the equation of state, which establishes the connection between various thermodynamic quantities such as temperature, pressure, and energy density. At sufficiently high collision energies, the value of μ_B becomes small enough to approximate it as zero, as is the case at the LHC, for instance.

Heavy-ion collisions traverse different trajectories in the phase diagram, starting as a QGP at high temperatures and gradually cooling down into a hadron gas. The transition can be either a crossover or a first-order phase transition, depending on the value of μ_B. Higher energy collisions correspond to higher initial temperatures and lower baryon chemical potentials, enabling the exploration of distinct regions within the phase diagram.

The conversion of the system back into particles, known as hadronization, is completed at a proper time of $\tau \sim 10$ fm/c. At this stage, the system transforms into a hadron resonance gas (HRG), primarily composed of pions, the lightest hadrons, along with protons, neutrons, and numerous other species, including various unstable resonances. The gas continues to expand and cool as particles scatter and resonances decay into stable species. Following hadronization, the decay and other chemical interactions come to a halt, resulting in the freezing of the system's composition, known as "chemical freeze-out." As the temperature reaches approximately $T \sim 120$ MeV, the system becomes dilute enough for scatterings to cease, thereby fixing the particle momenta in a process referred to as "kinetic freeze-out." After a few nanoseconds, the particles stream into the experimental detector, where their tracks are recorded and subsequently processed to obtain observable quantities.

This provides an overview of ultra-relativistic heavy-ion collisions. However, direct observation of the system is not feasible due to its small and fleeting nature, as well as the QCD color confinement preventing the direct detection of free quarks and gluons. Consequently, much of our knowledge is inferred by comparing computational collision models with experimental observations. The primary objective of this work is to systematically perform this model-to-data comparison and provide quantitative insights into the physical properties of the QGP and the intricate dynamics occurring in heavy-ion collisions. In the following sections of

this chapter, I will introduce the key experimental observations essential for this comparison and outline the properties that we aim to measure.

2.3 Experimental Observations

There are two particle accelerators with ongoing heavy-ion programs: the Relativistic Heavy-ion Collider (RHIC) at Brookhaven National Lab in Upton, NY, and the aforementioned Large Hadron Collider (LHC), operated by the European Organization for Nuclear Research (CERN) near Geneva, Switzerland (the accelerator ring intersects the French-Swiss border).

RHIC has been operational since 2000, colliding assorted combinations of nuclear species, including gold, uranium, copper, aluminum, protons, deuterons, and helium-3 at center-of-mass energies ranging from $\sqrt{s}$ = 7.7 to 200 GeV per nucleon-nucleon pair. The LHC, which turned on in 2009, runs proton-proton, proton-lead, and lead-lead collisions. Although the LHC focuses on proton-proton, the lead-lead collisions, at energies of $\sqrt{s}$ = 2.76 and 5.02 TeV, are the most relevant to this work. The two facilities are complementary: While the LHC achieves higher energy, RHIC can run more collision systems over a wide energy range—crucial for exploring the QCD phase diagram.

For heavy-ion collisions, size is the principal difference among the various projectile species; the larger the nucleus, the higher the produced QGP. Most nuclei used in collisions are approximately spherical, the notable exception being uranium, whose deformed spheroidal shape has some interesting consequences for the collision dynamics.

Both colliders have several experimental detectors distributed around their accelerator rings, each optimized for studying certain phenomena of high-energy collisions. In this work, I use data from ALICE (A Large Ion Collider Experiment) at the LHC, which specializes in heavy-ion collisions. The ALICE Collaboration has published consistent data for pp $\sqrt{s}$ = 0.9 and 13 TeV suitable for direct comparison with computational models. The other heavy-ion experiments at the LHC are ATLAS and CMS; at RHIC, there is STAR, PHENIX, PHOBOS, and BRAHMS (although these all stand for something, most are fairly contrived, and the acronyms are used almost exclusively).

2.3.1 Particle production

The most straightforward measurable quantities in high-energy collisions are the particle multiplicity (number of produced particles) and the energy yield. Despite their simplicity, these observables should not be underestimated, as they provide crucial insights into the thermal properties of the QGP and serve as important constraints for computational models.

Typically, particle and energy yields are reported per unit of rapidity y or pseudorapidity η. It is important to note that pseudorapidity η and spacetime rapidity η_s have similar mathematical forms but operate on different quantities. The rapidity, defined as

$$y \equiv \frac{1}{2}\log\left(\frac{E+p_z}{E-p_z}\right), \tag{2.9}$$

depends on the particle's total energy or mass, which may not always be directly measurable in experiments.

On the other hand, the pseudorapidity is sometimes more accessible as it solely relies on the polar angle of the momentum vector relative to the beam axis ($\cos\theta = p_z/|\mathbf{p}|$). It is given by

$$\eta \equiv -\log\left[\tan\left(\frac{\theta}{2}\right)\right] = \frac{1}{2}\log\left[\frac{|\mathbf{p}|+p_z}{|\mathbf{p}|-p_z}\right]. \tag{2.10}$$

In the ultra-relativistic limit ($p \gg m$), the rapidity and pseudorapidity become equivalent.

Particles emitted perpendicular to the beam, known as midrapidity (near $\eta = 0$), represent the purest sample of matter produced in the collision.

Fig. 2.2 illustrates the charged particle multiplicity per unit pseudorapidity, $dN_{ch}/d\eta$, in the central rapidity unit ($\eta < 0.5$) from ALICE measurements of lead-lead collisions at $\sqrt{s}$ = 2.76 and 5.02 TeV, as well as proton-proton and proton-lead collisions for comparison. The multiplicities are plotted as a function of the number of participating nucleons, N_{part}, and scaled by participant pair, $N_{\text{part}}/2$. In this context, a "participant" refers to a nucleon that engages in inelastic collision processes, while a spectator continues unaffected along the beam pipe. Collisions classified as "central," meaning those with a small impact parameter and significant nuclear overlap, have a larger number of participants, while "peripheral" collisions with large impact parameters have fewer participants. The maximum number of participants in a ^{208}Pb nucleus collision is 416.

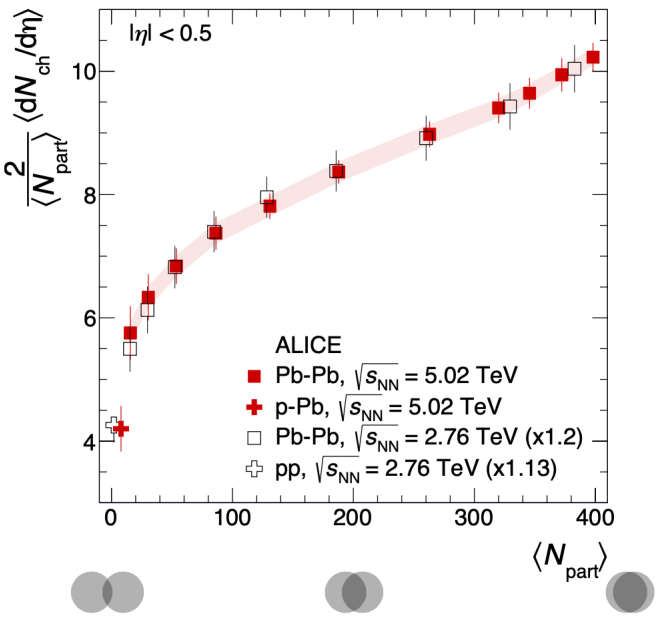

Figure 2.2: Charged-particle multiplicity at midrapidity per participant pair as a function of the number of participants. The circle diagrams show the approximate nuclear overlap of the collision depending on N_{part} [45–48].

Due to the high collision energy, a substantially greater number of particles are produced compared to the initial number of nucleons. In the most central collisions with the highest number of participants ($N_{\text{part}} \sim 400$), approximately 10 charged particles are produced per participant pair, resulting in approximately $dN_{ch}/d\eta \sim$ 2000 total particles within the central rapidity unit alone at 5.02 TeV. However, particle production is not directly proportional to the number of participants. Central collisions exhibit a higher efficiency in particle production per participant compared to peripheral collisions. This trend is consistent at both beam energies, with 5.02 TeV collisions generating approximately 20% more particles than 2.76 TeV collisions in a uniform manner.

Another commonly used measure of the produced matter is the transverse energy, denoted as E_T. It is computed as the sum of the total energy, E_i, multiplied by the sine of the angle, θ_i, with respect to the beam, for each particle i. The transverse energy is closely related to charged-particle production and exhibits a similar dependence on N_{part}. Figure 2.3 illustrates the average transverse energy per charged particle at midrapidity for lead-lead collisions at 2.76 TeV and RHIC

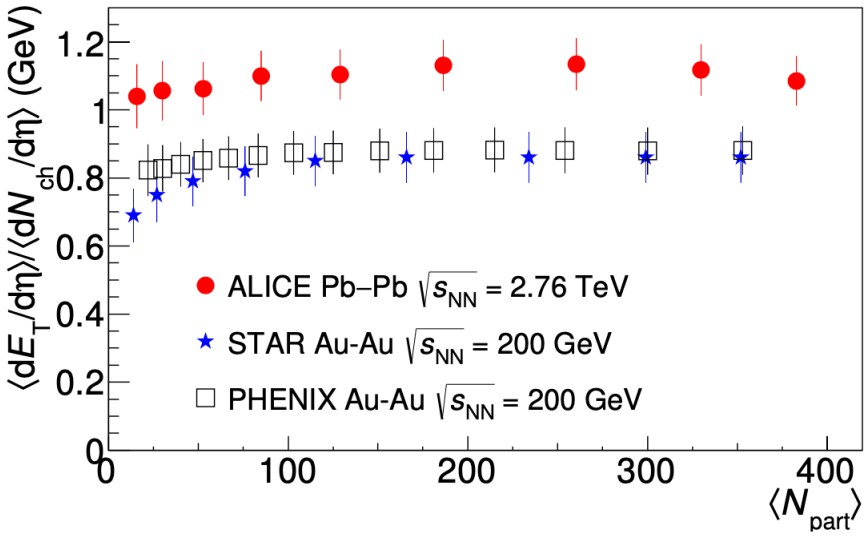

Figure 2.3: Average transverse energy per charged particle at midrapidity as a function of the number of participants [49–52].

AuAu collisions at 200 GeV. The ratio remains constant within the uncertainty as a function of N_{part}, but it is evident that higher-energy collisions produce more transverse energy per particle.

In previous discussions, I have introduced the concept of centrality and its association with N_{part}. However, as the primary classifier of heavy-ion collision events, centrality deserves a dedicated explanation. Centrality categorizes events based on a final-state observable that quantifies the amount of matter produced in the collision, such as N_{ch} (charged particle multiplicity) or E_T. By establishing a connection between these observables and the underlying geometric properties of the initial state, such as N_{part} and the impact parameter b, centrality estimation allows for the characterization of events using a geometric initial condition model, even though N_{part} and b themselves are not directly measurable.

In the last decades, many experiments have been carried out to create QGP in the laboratory. Starting with the ISR experiments at CERN and AGS at BNL, and later at SPS and RHIC, which reached energies of $\sqrt{s} = 200$ GeV. In 2010 the LHC at CERN reached the energies of $\sqrt{s} = 2.76$TeV for Lead-Lead collisions. RHIC data shows very strong suppression of particles with high transverse momentum in collisions *Au-Au* with respect to the expected number, given by the product of the

number of nucleon-nucleon collisions with the proton-proton production, which is what would be expected from the application of the factorization theorem.

In addition, the central collision data *Au-Au* show that when a *jet* in a given direction, there is a deletion of the *jet* expected in the opposite direction, contrary to what is seen in collisions *p-p* where both jets are clearly visible. On the other hand, a strong suppression of the number of particles produced has been observed that leads to a saturation of the multiplicity per nucleon participating in the collision and an elliptical flow whose behavior and dependence on the mass of the particles is consistent with hydrodynamic calculations that assume that the system created in the collision is isotropic very quickly [53–56]. All these results point to the creation of high-density matter, with partonic degrees of freedom [57]. The initial state of the collision could be described by parton saturation models such as the one called *Color Glass Condensate* (CGC), hydrodynamically described as an almost perfect fluid (very low viscosity). Due to the existence of this medium constituted by an almost perfect partonic fluid of very high density, the propagation of particles with high transverse momentum is strongly modified with respect to its propagation in a vacuum.

2.3.2 Thermalization and Elliptical Flow

Matter produced in ultrarelativistic ion collisions in RHIC is believed to be thermalized, and such thermodynamic equilibrium is reached very soon. This is deduced from the abundance of the different classes of hadrons, the distribution of the particles produced at low transverse momentum, and the elliptical flow.

The production of foreign particles allows us to verify if thermalization has been achieved. In collisions e^--e^+ y p-$\bar{p}$, the abundances of the different types of hadrons are reasonably well described by statistical models [58, 59]. Due to the small size of the system, in these cases, the production of strangeness is suppressed. The strangeness suppression factor can quantify the degree of equilibrium, $\gamma_s = 2(s+\bar{s})/(u+\bar{u}+d+\bar{d})$, which describes the ratio between the number of particles with the quarks or the antiquark $\bar{s}$ and the number of non-strange particles with quarks and antiquarks u, $\bar{u}$, d, $\bar{d}$, $\gamma_s = 1$ indicates a complete balance. Experimental data on collisions *Au-Au* a $\sqrt{s} = 200$GeV by nucleon show that the ratios K^+/π^+, K^-/π^-, p/π^+, $\bar{p}/\pi^-$ they increase rapidly in peripheral collisions until they are saturated in semi-central and central collisions. Comparisons with the

grand canonical statistical model obtain a value of γ_s very close to 1. Therefore, the strangeness is balanced at RHIC energies, consistent with the chemical equilibrium obtained before hadronization [60].

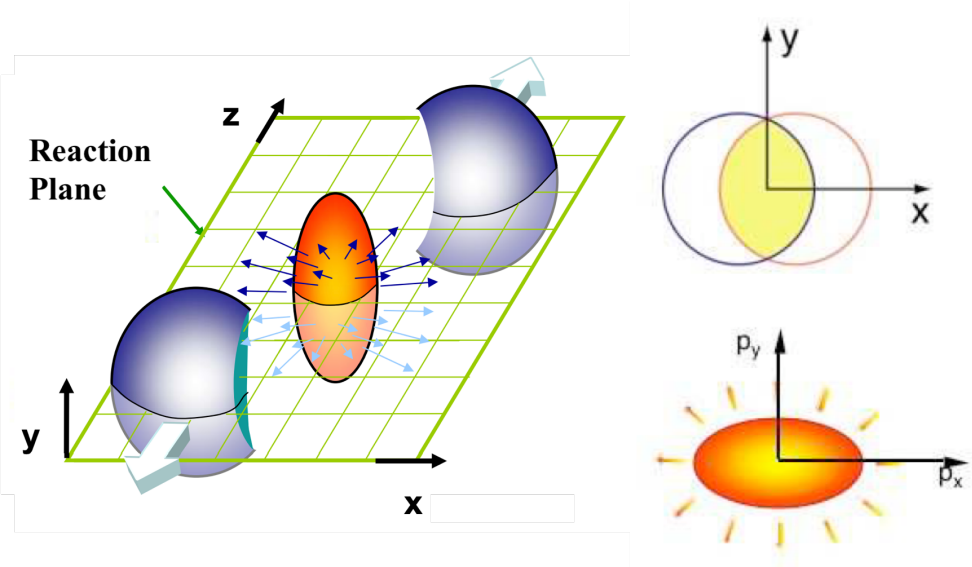

Figure 2.4: Overlap of two nuclei in the plane perpendicular to the collision axis z, and spatial and momentum asymmetries in the collision [61].

When two nuclei collide that impinge on each other in the direction z, the spatial distribution of the overlap is an ellipsoid. Any strong interaction in this initial state of the collision converts this spatial anisotropy into an anisotropy at moments, which is observed as an elliptical flow of the produced particles. Since the pressure gradient is greatest on the smallest axis of the ellipsoid, axis x, the spatial asymmetry disappears quickly since the highest moments of the produced particles will be in the direction of the gradient unless, in the initial state of the collision, there is a very strong interaction between the produced particles. This interaction could be partonic or hadronic, although experimental data point to a strong partonic interaction.

The collective flux is quantified in terms of the first coefficients of the Fourier series expansion of the azimuth angle distribution [62]. The inclusive cross-section of particle production k quickly y[1] transverse momentum p_T and azimuth angle ϕ

[1]Speed is usually denoted by the same letter as one of the spatial coordinates, y.

(measured from a fixed angle ϕ_R) is given by

$$\frac{dN_k}{dydp_t^2d\phi} = \frac{dN_k}{dydp_t^2}\frac{1}{2\pi}\left[1 + 2v_1\cos(\phi - \phi_R) + 2v_2\cos 2(\phi - \phi_R) + \cdots\right], \quad (2.11)$$

being v_1 radial flow and v_2 the elliptical flow,

$$v_1 = \langle\cos(\phi - \phi_R)\rangle = \left\langle\frac{p_x}{p_T}\right\rangle, \quad v_2 = \langle\cos 2(\phi - \phi_R)\rangle = \left\langle\frac{p_x^2 - p_y^2}{p_T^2}\right\rangle, \quad (2.12)$$

that depends on the detected particle k, its speed, its transverse momentum, and the degree of centrality of the collision. If the elliptical flow reflects an initial spatial anisotropy expressed by eccentricity (written in terms of the coordinates x y y):

$$\epsilon = \left\langle\frac{y^2 - x^2}{y^2 + x^2}\right\rangle \quad (2.13)$$

that requires, so that it does not disappear, an interaction between the formed matter, it would be expected that v_2 was proportional to the eccentricity and the density of interactions. The latter will be proportional to the density of charged particles produced per unit of speed y, namely,

$$v_2 \sim \frac{\epsilon}{S}\frac{dN_{ch}}{dy}, \quad (2.14)$$

where S is the transverse area of the ellipsoid formed in the collision. The proportionality given by Eq. 2.14 it has been verified for AGS, SPS and RHIC energies, and for a very wide range of projectiles and targets. At energies lower than AGS of 11.8 GeV per nucleon, v_2 no longer verifies Eq. 2.14 and it is even negative. The reason for this is that at low energy, non-participating nucleons (called spectators) prevent the "output" of the interacting matter by the shortest axis of the ellipsoid, with which there is a greater production of particles along the longest axis, where there are no nucleons. Also, it has been experimentally seen that the flux is higher for light particles [57].

Predictions from hydrodynamic models are consistent with experimental measurements [63]. The existence of an asymmetric collective flow velocity field is proposed, common to all particles: pions, kaons, protons, lambdas, etc. Agreement is obtained only when an equation of state is entered "soft", that is, with speed of sound c_s^2 very small, as shown by the Lattice QCD result close to critical temperature T_c previously mentioned.

There is a scale law that has been verified with a very good approximation, v_2/n in function of $E_T/n = \left(\sqrt{p_T^2 + m^2} - m\right)/n$, with n the number of quarks or antiquarks of the particle. This law was predicted by various models that assume a medium formed by partons [64].

In fluid dynamics, the different characteristics of flows are classified by dimensionless numbers. Thus, low viscous fluids are characterized by a large Reynolds number, $R_e = \varepsilon L v_f/\eta_s$, where ε, v_f y η_s are respectively the energy density, the fluid velocity and the shear viscosity (*shear viscosity*), while L is the longitudinal scale of the system. Similarly, the Mach number $M_a = v_f/c_s$ quantifies the difference between incompressible fluids, $M_a \ll 1$, and compressible, $M_a \sim 1$. Finally, the Knudsen number, $K_n = \lambda/L$, where λ is the mean free path, it marks the difference between systems with a low number of collisions per particle of the medium, that is, large K_n as in the case of freely flowing gases, and liquid-type systems where there are many collisions per particle, $K_n \ll 1$. These three numbers are related since $\eta_s = \varepsilon c_s \lambda$ and therefore, $M_a = R_e \times K_n$. As matter formed in collisions between heavy ions expands, the corresponding flow is compressible and $M_a \sim 1$. So, $R_e \simeq 1/K_n$, implying yes K_n it is small, the viscosity is small.

As a function of the inverse of the Knudsen number, K_n^{-1}, the expected dependence of the elliptical flow is the one represented in Fig. 2.5. Indeed, it is natural to expect that the elliptical flow increases with the number of interactions, and that it disappears in the absence of these. The opposite case is the limit of the ideal fluid in which v_2 it is finite. For larger values of K_n^{-1}, v_2 it remains constant according to the scale invariance in the ideal fluid description. This behavior means that if we have an ideal fluid, thermalized and with low viscosity, a curvature must appear that causes the increasing behavior of the elliptical flow against the multiplicity [65] lead to expected saturation.

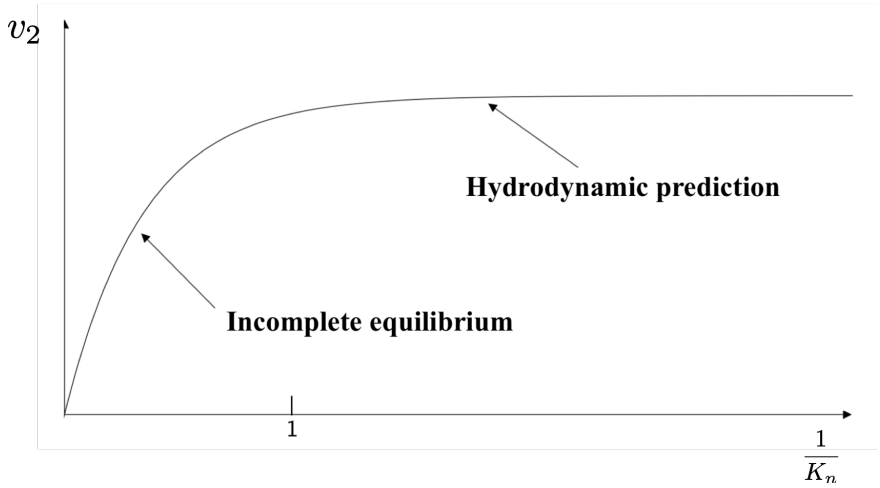

Figure 2.5: Behavior of the elliptical flow coefficient v_2 against the inverse of the Knudsen number K_n^{-1}

The possibility that the partonic matter formed is an ideal low-viscosity liquid has been of interest to physicists in string theory. The Anti-de Sitter correspondence in conformal field theory (AdS / CFT) allows calculating the properties of a supersymmetric Yang-Mills theory with $\mathcal{N} = 4$ in terms of gravity in a curved space. The strong coupling limit (great constant of 't Hooft, $g^2 N_c \to \infty$) corresponds to the weak coupling of gravity. In the supersymmetric Yang-Mills theory with $\mathcal{N} = 4$, the ratio of viscosity to entropy density satisfies $\eta_s/s \geq 1/4\pi$, approaching the limit of the dimension when the coupling becomes infinite [66]. Although supersymmetric theories with $\mathcal{N} = 4$ do not correspond to the physical world, it has been argued that this bound could be a consequence of the strong coupling in QCD. The limit is reached when the mean free path of a particle equals its de Broglie wavelength. Below this limit, the "amusement" and scattering are suppressed by quantum coherence.

2.3.3 Jet Quanching

Suppression of particles with high transverse momentum (*Jets*) due to the effect of the loss of energy due to the interaction with a dense medium, it is a prediction due to Bjorken in 1982 [67]. The disappearance of the *jets* in opposite directions when one of them escaped crossing a small distance in the middle and the other

was absorbed by traveling a great distance in it. The observable with which this suppression is measured is known as *jet quenching*, the nuclear suppression factor in collisions A-B for a particle k:

$$R^k_{AB}(y, p_T) = \frac{\dfrac{dN^k_{AB}}{dydp_T}}{\langle N_{coll} \rangle \dfrac{dN^k_{pp}}{dydp_T}}. \tag{2.15}$$

The numerator in this expression is the quantity measured in the nuclear collision. The denominator is the quantity that would be expected if there were no nuclear effect: the rate of production in proton-proton collisions multiplied by the number of nucleon-nucleon collisions for a given centrality of the nuclear collision, $\langle N_{coll} \rangle$. The Glauber model calculates this last quantity, which contains information on nuclear geometry. Thus, in the absence of nuclear effects, $R^k_{AB} = 1$. There are initial state effects, that is, not due to the creation of a medium after the collision but to the fact that the partonic densities in the nucleons of the colliding nuclei are different from those in a proton, for reasons of both isospin and genuinely nuclear effects [68]. These effects could cause $R^k_{AB} \neq 1$ even in the absence of a medium. Control experiments, and the study of particles whose propagation is not affected by the medium, such as photons not coming from decays of other particles (direct photons), as seen in Fig. 2.6, have allowed us to conclude that the suppression, of approximately a factor 5 for $p_T > 7$GeV, It is due to the creation of a medium in the collision between heavy ions. This is repeated for other strongly interacting particles, such as protons, which, however, show a different behavior at a lower transverse moment [53–56].

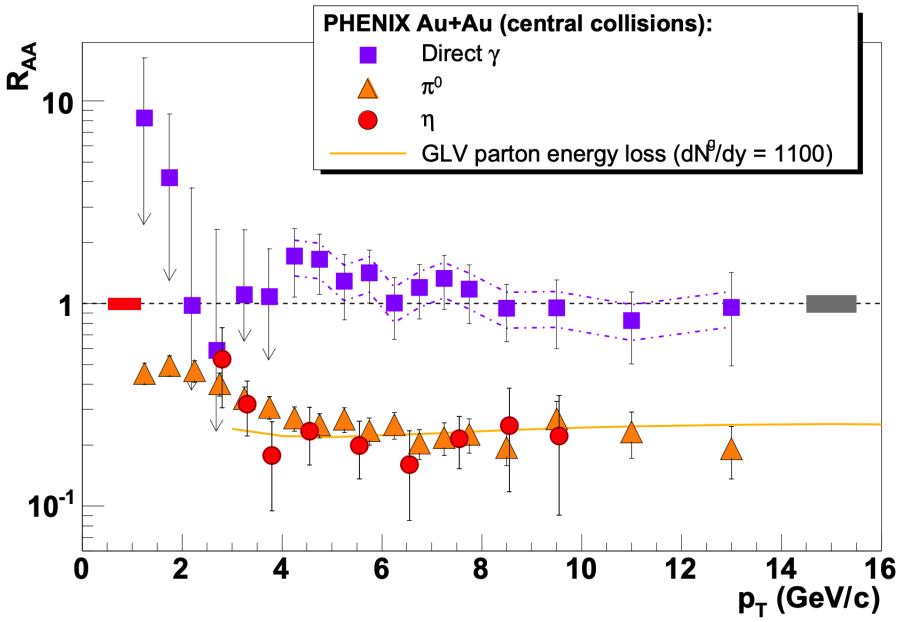

Figure 2.6: Nuclear suppression factor at central speed, measured in collisions *Au-Au* central at 200 GeV per nucleon, for direct photons, π^0 y η [69].

The absence of suppression in direct photons and the large suppression for other particles, in addition to the suppression of correlations between particles in one direction and particles in the opposite direction, show that the medium created in the collision is very opaque and dense. The fact that two particles whose fragmentation is as different as π^0 or η show the same suppression, and their persistence until the highest measured transverse moments, suggests that this phenomenon is due to something that happens before fragmentation, that is, at the partonic level, while the projection of the partons on final hadrons takes place out of the middle. Hence the conclusion drawn at RHIC is that a dense partonic medium is produced that lasts long enough to very strongly disturb the propagation of the particles that pass through it.

Other evidence found in RHIC appears when studying the azimuthal correlations at central speed $y = 0$ between the particles produced with respect to a high transverse moment. Considering that the highest particle p_T of the event establishes the *trigger* and marks the azimuthal angle 0, it would be expected to observe a peak at 180 degrees by compensation of transverse momentum, as it is observed in collisions *p-p*. What is measured is that if a particle is studied *trigger*

of very high momentum and associated high momentum particles, the peak that would be expected at 180 degrees disappears. On the other hand, if associated low momentum particles are studied, a flat structure appears or even with a depression at 180 degrees that is not yet understood, and may be associated with the lost energy of the *jet* or to the disturbance of the environment when a very energetic particle passes through it.

The usual explanation for this phenomenon is radiation losses induced in a medium [70–72], although other collisional mechanisms or at the hadronic level cannot be excluded for the suppression of particles containing heavy quarks c y b. Induced gluon radiation occurs due to gluon auto-coupling in QCD. The study of this radiation, together with the phenomena of finite coherence length (Landau-Pomeranchuk-Migdal effect), leads to the following result for energy loss ΔE of a very energetic parton:

$$\Delta E \sim \alpha_s \hat{q} C_R L^2 \tag{2.16}$$

with L the length of the medium and C_R the color charge of the radiating parton. That is, the energy loss is independent of the energy of the parton, proportional to its color charge, and proportional to the square of the length of the medium. This last feature is peculiar to QCD and does not appear in QED. Finally, the energy loss is proportional to a transport coefficient of the medium, $\hat{q}$, which is proportional in turn to the density of the medium by the effective section of *scattering* between the middle and the parton that crosses it.

The LHC experiments have extended the study of flux to the other harmonics, confirming that the medium formed in nuclear collisions strongly interacts [73–77]. Currently, the LHC results point to the creation of a strongly interacting medium even in pPb and pp collisions [78–81].

2.4 Color Glass Condensate

There are reasons to think that the initial state of the matter formed in the collision has its origin in the saturation of partons, forming in the nuclei that collide with colored condensates (*Color-Glass Condensate*) [82, 83]. Such condensates, after crossing, develop longitudinally extended color flux tubes. These coherent color fields form the so-called "glasma", within the string models, of forming a *cluster* formed by overlapping strings when they reach a critical density (percolation of strings).

This type of model allows us to understand both the behavior of multiplicities with energy and the amount of nuclear matter involved in the collision, and they offer a framework in which to calculate the distribution of particles and their dynamics prior to thermalization.

When considering a projectile that interacts with a nucleus A at high energies, small values of x (the fraction of momentum of the hadron carried by a parton), due to the uncertainty principle, the interaction develops over large longitudinal distances $\sim (mx)^{-1}$, where m is the mass of the nucleon. The projectile cannot distinguish between nucleons located forward and backward in the nucleus and all partons within a transverse area for distances greater than nuclear size $\sim 1/Q^2$ they participate in the interaction consistently.

The density of partons in the transverse plane is

$$\rho_A \simeq \frac{sG_A(x,Q^2)}{\pi R_A^2} \sim A^{1/3}. \tag{2.17}$$

The projectile interacts with the partons of the nucleus with a cross-section $\sigma \simeq \alpha(Q^2)/Q^2$. According to A, Q y x there are two regions:

a) $\sigma\rho_A \ll 1$, the usual regime of dilute partons and incoherent interaction.

b) $\sigma\rho_A \gg 1$, dense regime where the interaction is coherent.

The border between the two regimes, given by the condition $\sigma\rho_A = 1$, determines the so-called saturation scale Q_s:

$$1 \simeq \frac{\alpha_s(Q_s^2)}{Q_s^2}\frac{xG_A(x,Q_s^2)}{\pi R_A^2}. \tag{2.18}$$

Note that the gluon density, xG_A, results inversely proportional to α_s from this equation, which is the typical behavior of a condensate.

In Fig. 2.7 the low and high-density regions are shown, as well as the behavior of the gluon distribution as a function of x at various values of resolution Q (equivalent to the size of gluons $1/Q$). As indicated in the figure, there is an increase in the number of gluons with increasing energy and making smaller values of x and larger than Q. This growth is due to the linear multiplicative effect in QCD; gluons generate more gluons producing exponential growth. However, for gluons measured at a fixed resolution, a saturation effect limits their growth. The gluons

are packed very close to each other, forming a highly coherent state, the CGC. Since the typical gluon spacing is very small, Q_s is big, and $\alpha_s(Q_s^2) \ll 1$. Although the coupling constant is small, since the system acts coherently (in the same way that the gravitational interaction is weak, but there is an overlap of the gravitational forces of the individual particles), the resulting fields are very large. A *glass* is a messy system but it evolves very slowly compared to natural timescales. In this case, the high-momentum gluons (high x) radiate low-momentum gluons, and this is the scale of natural evolution. At saturation, the low-momentum gluons are out of order, producing a classical field that evolves very slowly relative to the radiation times of the high-momentum gluons.

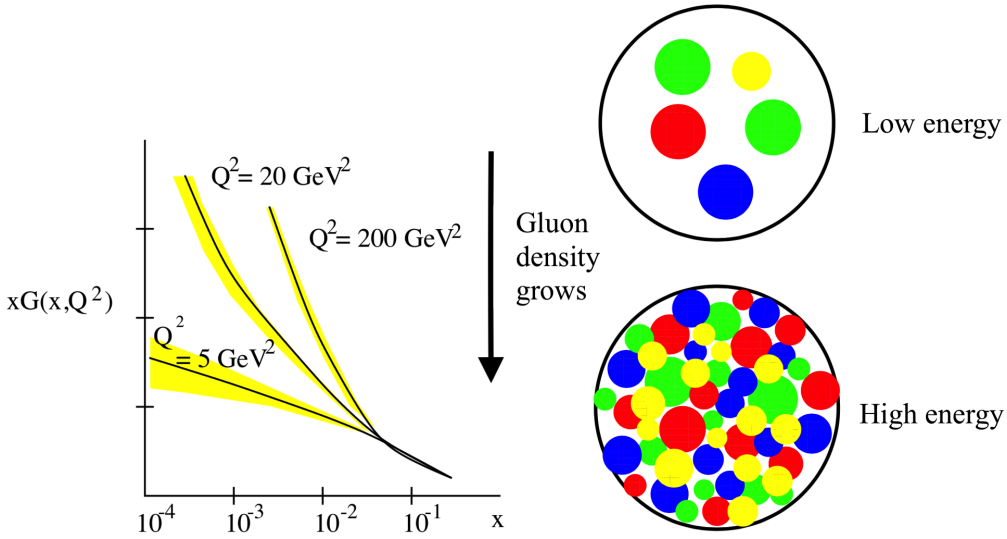

Figure 2.7: Behavior of gluon density within a hadron at different energy scales [57].

The dimensionless density of gluons ρ (the number of gluons per unit phase space) can be characterized by the number of particles produced with rapidity y and transverse momentum p_T, normalized to the area of a collision (central) πR_A^2. This density is saturated at the value $1/\alpha_s(Q_s^2)$, namely:

$$\rho \simeq \frac{1}{\pi R_A^2} \frac{d^3N}{dyd^2p_T} \propto \frac{1}{\alpha_s(Q_s^2)}, \tag{2.19}$$

the saturation scale $Q_s(x, A)$ controls gluon occupancy number $1/\alpha_s(Q_s^2)$, that being tall allows the use of semi-classical methods. The behavior of the density

described in Eq. 2.19 is only valid for $p_T < Q_s$. For wavelengths $1/p_T$ smaller than $1/Q_s$, we are outside the saturation region, and since the coupling constant is even smaller, we can use the usual perturbative methods.

Eq. 2.19 indicates that the number of particles produced in collisions A-A per unit area, or equivalently per pair of participating nucleons, hardly depends on the centrality of the collision, that is, on the number of participating nucleons [84]. The only dependence of Eq. 2.19 in this number comes through dependence on α_s en Q_s, and of this in the nuclear size A. This dependence originates only a logarithmic behavior with the number of participants that agrees with the experimental data [53–56]. The CGC has also been successful in describing experimental data such as the scaling law observed in *scattering* electron-hadron [85, 86].

In CGC, a collision between two nuclei can be thought of as the collision between two CGC disks. At the center of mass of the collision, they appear as thin disks at ultrarelativistic energies due to the Lorentz contraction. Due to the large number of gluons, these can be treated as classical fields that are in the plane perpendicular to the axis of the collision. It can be shown that the fields change rapidly from transverse to longitudinal because the collision generates opposite chromo-electromagnetic charges on the two disks. These coherent longitudinal fields form the so-called glasma [87], due to the overlap of the strings formed by the color fields joining the projectile and target partons once the critical string density (which is related to the saturation scale) is exceeded.

The CGC can provide the initial conditions needed to estimate the transport coefficients and bulk properties of the strong-interacting matter created in heavy ion collisions [88]. The strong coherent gluon fields lead to parton saturation controlled by a dynamically generated transverse momentum scale, the saturation scale Q_s [89–99]. The high gluon densities correspond to strong classical fields, and their quantum corrections are incorporated via nonlinear renormalization group equations. The nonlinear density-dependent terms in the CGC evolution equations can be identified as gluon recombination processes that saturate the increment in gluon densities below Q_s. The value of Q_s sets the scale of gluon field fluctuations that can describe the bulk multiplicity and its fluctuations depending on the considered colliding system [100–102]. The particle multiplicity distributions are intrinsically dependent on event-by-event fluctuations of the incoming nuclear wave functions.

Within the Color Glass Condensate (CGC) framework, the Impact Parameter (IP) Glasma model is utilized to capture the characteristics of the systems under study. This model combines the IP saturation dipole model [103] with the nonlinear dynamics of gluon fields [102, 104]. The distribution of Q_s^2 (saturation scale) can be employed to sample various color field configurations within the proton, following the McLerran-Venugopalan (MV) model [82, 105].

The IP-Glasma model incorporates fluctuations in the positions of static large-x color charges at the nuclear and sub-nuclear level. These fluctuations contribute to the dynamical small x modes within the CGC effective field theory [106, 107]. The occupation probabilities of the QCD fields vary, resulting in global fluctuations in observables such as energy density in the transverse plane of the collision. These fluctuations, in turn, influence the fluctuations in charged hadron flow harmonics during the system's dynamical evolution [108].

It has been proposed that in each event, the value of Q_s^2 at every point in the transverse plane fluctuates according to a probability distribution given by [109,110].

$$P\left[\ln\left(\frac{Q_s^2}{\langle Q_s^2\rangle}\right)\right] = \frac{1}{\sqrt{2\pi\varsigma^2}}\exp\left[-\frac{1}{2\varsigma^2}\ln^2\left(\frac{Q_s^2}{\langle Q_s^2\rangle}\right)\right]. \tag{2.20}$$

The chosen distribution of $Q_s/\langle Q_s\rangle$ results in a skewed distribution centered around 1. To describe heavy ion collisions ranging from AuAu to PbPb, we adopt the value of $\varsigma = 0.6$ as reported in [111].

In addition to the skewness, the saturation scale Q_s exhibits dependence on the size and energy of the colliding nuclei. Previous studies have indicated that Q_s grows with the size of the nuclei as $\sim A^{1/3}$ [82, 105, 112], where A represents the nucleon number. Furthermore, Q_s increases with energy following a power law $\sim \sqrt{s}^{\lambda}$ (in the midrapidity region) with $\lambda = 0.252$ [113]. For AuAu collisions at $\sqrt{s} = 130$ GeV, the chosen value for the saturation scale is $\langle Q_s^2\rangle = 2$ GeV^2 [84]. Utilizing the aforementioned scaling laws, we estimate the saturation scales for central AuAu collisions at $\sqrt{s} = 200$ GeV and central PbPb collisions at $\sqrt{s} = 2760$ and 5020 GeV to be 2.23, 4.399, and 5.114 GeV^2, respectively. These estimated values are utilized in the subsequent analysis of heavy ion collisions.

2.4.1 String Models

Most of the string models coincide in the dependence of the energy with the centrality given by the Glauber-Gribov model, then there is a difference that classifies the string models in those with color exchange between the partons of the projectiles or fixed targets, among these models stand out *Dual Parton Model* (DPM) [114–116], *Quark Gluon String Model* (QGSM) [117], VENUS [116], EPOS [118] y DPMJET [119]. On the other hand, there are models without color exchange such as HIJING [120], PYTHIA [121], AMPT [122], HSP and URQMD [123]. For this work, the exchange of color is considered, and the DPM based on expansion is taken as motivation $1/N_c$ of QCD that goes according to the calculations of the Gribov Reggeon.

A valid approach to studying the phase transition and the phenomena of collectivity in QCD is the percolation of strings, which is the central theme of this thesis. The percolation is not sourced directly from QCD but is inspired by the aforementioned string models. In string percolation, particle production is described in terms of colored strings stretched along the line joining the projectile partons and targets in heavy ion collisions; these strings decay in pairs q-$\bar{q}$ y qq-$\overline{qq}$ then hadronizing, producing the observed hadrons [124–128].

Due to confinement, the color of these chords is confined to a small region of the transverse plane $S_0 = \pi r_0^2$, with $r_0 = 0.2$fm. With increasing power or system size[2], the number of strings increases and they agglomerate, forming the so-called *clusters*, very similar to 2-dimensional disk percolation. Given a critical density, a *cluster*macroscopic appears crossing the total area of the collision, this marks the geometric phase transition that defines the percolation [129].

The basic elements of percolation are the strings, so to have a complete description of the system, it is necessary to know their total number, their extension in the speed coordinate, how they fragment, and their spatial distribution. All of this requires modeling and simulation, as do many of the QCD-inspired models, which provide results consistent with theoretical model-independent predictions, as well as being in accordance with experimental measurements.

The percolation of strings and the image of *Glasma* are related [130], at the high-density limit there is a correspondence between the physical quantities that are estimated in both parts. The number of color flow tubes in the image of *Glassma*,

[2]In nuclear collisions, this is determined by the centrality of the event.

$Q_S^2 R^2$, has the same dependence on energy and collision centrality as the effective number of *clusters* of ropes in percolation. In both approximations, a negative binomial distribution is obtained, where the parameter k, which controls width, has the same energy dependence and centrality. The role of the occupation number $1/\alpha_s$ in CGC is to play as the fraction of the total available surface covered by the strings formed in the collision. The anisotropy of the color field in CGC results in a reduction in the expected multiplicity. Similarly, the anisotropy of the color field of the n group strings stipulates that the resulting field strength is not n times the strength of the individual color field but $\sqrt{n}$. This reduction also implies a reduction in the multiplicity of particles produced in the collision. Due to all these similarities in both approaches, the predictions for different physical observables are very similar. String percolation is able to also explore the region where the high-density limit has not been reached.

Chapter 3

Color String Percolation Model

Multiparticle production at high energies can be described by the formation of color string and the subsequently breaking that gives rise to hadronization processes [115–117, 131–133]. The mechanism of particle creation bears a strong resemblance to the well-known Schwinger mechanism of pair creation, where a constant electric field pervades the entire space, with the exception that in the current scenario, the space is finite in the transverse plane. Notably, pair creation divides the space filled with the chromoelectric field into two parts, with each part connected to one of the initial and one of the created particles. Consequently, the evolution of string dynamics involves progressive fragmentation, giving rise to multiple interconnected strings. So the creation of particles goes via emission of q-$\bar{q}$ pairs. Is important to mention that, in the color string picture, the emitted partons have average transverse momenta determined by the strength of the chromoelectric field and do not depend on the transverse dimension of the string [127].

At low collision energies and when the atomic numbers of the colliding nuclei are small, the presence of strings with finite dimensions has negligible impact on the results, the color flux tubes are positioned at significant distances from each other, and particle creation is not influenced by their interaction. However, as the energy or atomic number of the colliding particles increases, the number of strings also increases. When the strings acquire a nonzero dimension in the transverse space, they begin to overlap, leading to the formation of a spanning cluster across the interaction area.

Percolation theory governs the geometric arrangement of string clusters, but to observe its implications, clustering dynamics must be introduced to describe string interactions. These interactions refer to the behavior of a cluster formed by

multiple overlapping strings. A naive assumption would be that nothing happens when strings overlap; in other words, they continue to independently emit particles without being influenced by their overlapping neighbors. However, this scenario of non-interacting strings contradicts the notion that strings represent regions of the transverse space filled with color field and, consequently, energy. In areas of overlap, the energy should logically increase. In another limiting case, it is possible to assume that a cluster formed by several overlapping strings behaves as a single string with a correspondingly increased color field, often referred to as a "color rope" [134]. This fusion scenario was proposed in [135–137] and later implemented as a Monte Carlo algorithm. The model predicts a decrease in total multiplicities and forward-backward correlations (FBC), as well as an enhancement in strange baryons, which is in reasonably good agreement with the observed experimental trends.

It is important to note that the previously discussed scenarios represent limiting cases. In typical situations, strings only partially overlap, making it unlikely for them to fuse into a single string-like object, particularly when the overlap is minimal. Instead, the transverse space occupied by a cluster of overlapping strings is divided into distinct areas, where varying numbers of strings overlap, including regions where no overlapping occurs at all. In each of these areas, the color fields originating from the overlapping strings combine. As a result, the overall cluster area is divided into domains with different strengths of the color field.

As an initial approximation, if we neglect the interaction at the boundaries between domains, we can assume that the emission of q-$\bar{q}$ pairs within each domain proceeds independently, governed by the field strength (referred to as "the string tension") specific to that domain. This perspective implies that the clustering of strings actually leads to their proliferation rather than fusion since each individual overlap can be considered as a separate string. It is important to note that the newly formed regions not only differ in color but also in their transverse areas.

Taken all of these ideas into account, let me explain the basics ideas of the the Color String Percolation Model (CSPM).

3.1 Basics of the CSPM

The CSPM uses the two dimensional percolation theory [138–140] to study the geometrical phase transitions of $SU(3)$ semi-classical fields, which is useful to characterize the medium formed in ultra-relativistic ion collisions from small systems to heavy nuclei [127, 141–152].

In the picture of the CSPM, the interaction between colliding nucleons is represented by the formation of extended color flux tubes which are stretching among the colliding partons and carry a fraction of the partons momentum, as pictorially illustrated in Fig. 3.1.

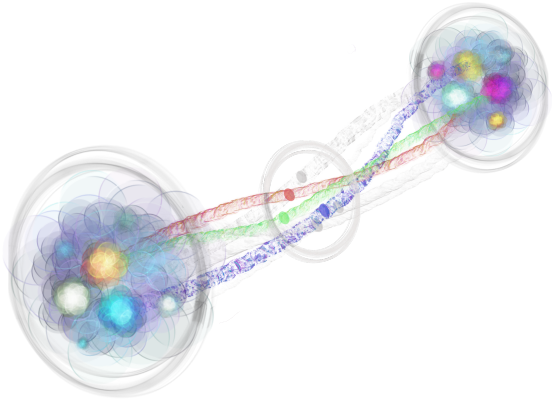

Figure 3.1: Sketch of two colliding protons where a set of color flux tubes is formed representing the interaction between partons.

The color flux tubes project their transversal areas into an interaction area over the impact parameter plane, the transverse strings formed are represented by fully penetrable disks (as seen in Fig. 3.1), and we estimate the effective projection area of disks from the parton-parton cross section ~ 3.5 mb [127, 136, 141, 153], in fact, each string has a radius $r_1 \approx 0.2385$ fm[1].

A certain number of transverse strings (N) are created in the collision event and each of them is placed over the total interaction area S as depicted in Fig. 3.2.

[1]For simplicity, all the color strings are considered of the same area S_1.

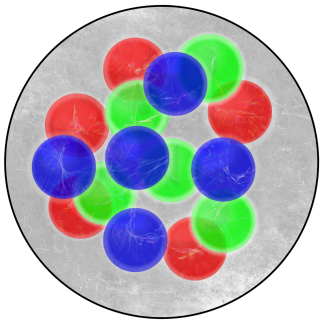

Figure 3.2: Scheme of ($N = 15$) transverse color strings over interacting (gray) area S.

3.2 Clustering of color sources

In the CSPM, the color field interaction in relativistic particle collisions are described from the clustering of the color flux tubes projections. Since each individual color string carries a semi-classical color field arbitrarily oriented $\mathbf{Q}_1$ with color field intensity Q_1. Whit this considerations, it is possible to define a color density $\rho_Q = Q_1/S_1$. Every initial string produces particles at the final state, from this assumption, each string has associated a multiplicity in a pseudorapidity interval μ_1 and average squared transverse momentum $\langle p_T^2 \rangle_1$ of particle distribution, both are proportional to the string tension [127, 141, 153] as I show below.

3.2.1 Overlapping of two strings

The overlapping of strings gives rise to several overlapping regions named color sources, with physical quantities that depend on the overlapping phenomena. To illustrate this let me discuss, for example, the cluster formed of two overlapping strings [154]. As depicted in Fig. 3.3 there are three different color sources: green (1), cyan (2), and blue (3) of areas $S^{(1)}$, $S^{(2)}$ and $S^{(3)}$ respectively.

In principle, (1) and (3) are two independent color sources with equal area $S^{(3)} = S^{(1)}$, such that $S^{(1)} = S_1 - S^{(2)}$ where the contributions of color fields sum one another. The main idea is that each color source produces charged particles, it means, each region has associated a certain color density which produces particle multiplicity and transverse momentum distribution. Is easy to identify the color

charge on the regions with no overlapping, from the color density ρ_Q the color sources (1) and (3) has color charge:

$$Q^{(1)} = \rho_Q S^{(1)} = Q_1(S^{(1)}/S_1), \tag{3.1a}$$

$$Q^{(3)} = \rho_Q S^{(3)} = \rho_Q S^{(1)} = Q^{(1)}. \tag{3.1b}$$

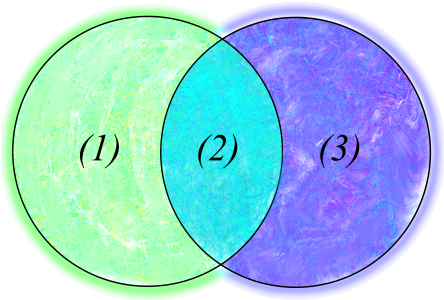

Figure 3.3: Sketch of the interaction between two color sources.

For the overlapping region (2), the two strings has an equal vectorial contribution to the color source, whit magnitude $\rho_Q S^{(2)} = Q_1(S^{(2)}/S_1)$. Thus the color charge $Q^{(2)}$ of (2)is the vector sum considering that color sources (1) and (3)are of equal color field intensity and in average $\langle \mathbf{Q}_1, \mathbf{Q'}_1 \rangle = 0$ [134, 148, 155]. From where:

$$Q^{(2)} = \sqrt{2}\rho_Q S^{(2)} = \sqrt{2}Q_1(S^{(2)}/S_1). \tag{3.2}$$

The ratio of multiplicity $\mu^{(j)}$ over its corresponding color charge of a color source is proportional to the string's according to [127, 141, 153]:

$$\frac{\mu^{(j)}}{Q^{(j)}} = \frac{\mu_1}{Q_1}, \tag{3.3}$$

with $j = 1, 2, 3$. Therefore, the total multiplicity of the cluster formed by 2 strings can be expressed as the contribution of the individual color source [127, 141, 153]:

$$\begin{aligned} \mu &= \mu^{(1)} + \mu^{(2)} + \mu^{(3)} \\ &= 2\mu^{(1)} + \mu^{(2)} \\ &= 2Q^{(1)}\frac{\mu_1}{Q_1} + Q^{(2)}\frac{\mu_1}{Q_1} \\ &= 2\mu_1\frac{S^{(1)}}{S_1} + \sqrt{2}\mu_1\frac{S^{(2)}}{S_1}. \end{aligned} \tag{3.4}$$

The average squared transverse momentum contribution of every color source is weighted by the multiplicity as [127, 141, 153]:

$$\begin{aligned}\langle p_T^2\rangle &= \frac{\mu^{(1)}\langle p_T^2\rangle^{(1)} + \mu^{(2)}\langle p_T^2\rangle^{(2)} + \mu^{(3)}\langle p_T^2\rangle^{(3)}}{\mu} \\ &= \frac{2\mu^{(1)}\langle p_T^2\rangle^{(1)} + \mu^{(2)}\langle p_T^2\rangle^{(2)}}{\mu} \\ &= 2\frac{\mu_1}{\mu}\frac{S^{(1)}}{S_1}\langle p_T^2\rangle_1 + \sqrt{2}\frac{\mu_1}{\mu}\frac{S^{(2)}}{S_1}\sqrt{2}\langle p_T^2\rangle_1. \end{aligned} \tag{3.5}$$

By using Eq. (3.4) and Eq. (3.5) and taking into account that $S^{(1)} + S^{(2)} = S_1$ a natural relation between multiplicity and transverse momentum emerges [127, 141, 153]:

$$\begin{aligned}\frac{\langle p_T^2\rangle}{\langle p_T^2\rangle_1} &= \frac{2(S^{(1)}/S_1) + 2(S^{(2)}/S_1)}{2(S^{(1)}/S_1) + \sqrt{2}(S^{(2)}/S_1)} \\ &= \frac{2}{2(S^{(1)}/S_1) + \sqrt{2}(S^{(2)}/S_1)} = 2\frac{\mu_1}{\mu}. \end{aligned} \tag{3.6}$$

3.2.2 Overlapping of N strings

Now lets explain the general case of N strings in a cluster, where M color sources are formed (as can be illustrated as an example in Fig. 3.2). μ and $\langle p_T^2\rangle$ are given by the general case of Eq. 3.4 and Eq. 3.5 respectively [127, 141]:

$$\mu = \sum_{i=1}^{M}\mu^{(i)} = \sum_{i=1}^{M}\frac{\sqrt{n_i}S^{(i)}}{S_1}\mu_1, \tag{3.7}$$

$$\langle p_T^2\rangle = \frac{1}{\mu}\sum_{i=1}^{M}\mu^{(i)}\langle p_T^2\rangle^{(i)} = \frac{\sum_{i=1}^{M}\left(\frac{n_i S^{(i)}}{S_1}\right)}{\sum_{i=1}^{M}\left(\frac{\sqrt{n_i}S^{(i)}}{S_1}\right)}\langle p_T^2\rangle_1. \tag{3.8}$$

The number of color sources M coincides with the number of regions $S^{(i)}$ in where there exists n_i partial overlapping of strings. Note that the case $n_i = 1$ corresponds to the remnant fraction surfaces with no overlapping (as regions (1) and (3)in Fig. 3.3). By using the relations (3.8) and $\sum_{i=1}^{M} n_i S^{(i)} = NS_1$ it is establish the relation between $\langle p_T^2\rangle/\langle p_T^2\rangle_1$ and μ/μ_1, the general case of Eq. (3.6):

$$N = \frac{\mu}{\mu_1}\frac{\langle p_T^2\rangle}{\langle p_T^2\rangle_1}, \tag{3.9}$$

Eq. (3.9) can be interpreted as a conservation law for the transverse momentum of the produced particles given the total multiplicity of the event [127, 141, 153].

Identifying the overlapping regions is a complicated task at a practical level, so it is convenient to rewrite the expressions that involve sums in the number of color sources of a cluster M in terms of the number of initial strings N. Eq. (3.7) can be split as a sum of terms with fixed n_i, where S_n^{tot} is identify as the sum of all regions that has $n = n_i$ overlapped disks. Therefore:

$$\begin{aligned}\frac{\mu}{\mu_1} &= \sum_i^M \frac{\sqrt{n_i} S^{(i)}}{S_1} \\ &= \frac{\sqrt{1}}{S_1} \sum_{i,n_i=1} {S^{(i)}}_{n_i=1} + \frac{\sqrt{2}}{S_1} \sum_{i,n_i=2} {S^{(i)}}_{n_i=2} + \cdots + \frac{\sqrt{N}}{S_1} \sum_{i,n_i=N} {S^{(i)}}_{n_i=N} \\ &= \sum_{n=1}^N \frac{\sqrt{n}}{S_1} \sum_{i,n_i=n} {S^{(i)}}_{n_i=n} = \sum_{n=1}^N \frac{\sqrt{n}}{S_1} S_n^{\text{tot}},\end{aligned} \tag{3.10}$$

and from Eq.(3.9) [127, 141, 153]:

$$\frac{\langle p_T^2 \rangle}{\langle p_T^2 \rangle_1} = N \frac{\mu_1}{\mu} = \frac{N}{\sum_{n=1}^N \frac{\sqrt{n}}{S_1} S_n^{\text{tot}}}. \tag{3.11}$$

As the small disks are distributed on a large surface uniformly, Eq. (3.10) becomes

$$\frac{\mu}{\mu_1} = \frac{\langle \sqrt{n} \rangle}{S_1} S = N \frac{\langle \sqrt{n} \rangle}{\xi}, \tag{3.12}$$

where

$$\xi = N \frac{S_1}{S}, \tag{3.13}$$

is the string density or filling factor, which describes the occupation of N strings of area S_1 over the total interaction area S. And the average on the number of strings is taken from a Poisson distribution [127, 141, 153]:

$$P_n = \frac{\xi^n}{n!} \exp(-\xi), \tag{3.14}$$

where the fraction of the total area covered by disks is $1 - \exp(-\xi)$ [127]. From Eq. (3.12) a damping on multiplicity appears and is given by a term named Color Suppression Factor $F(\xi)$:

$$F(\xi) = \frac{\mu}{N \mu_1} = \frac{\langle \sqrt{n} \rangle}{\xi}, \tag{3.15}$$

this geometric scaling emerges naturally from cluster formation [156]. For a fixed ξ and with $N \to \infty$, it means the Thermodynamic Limit (TL), $F(\xi)$ becomes [127, 141, 153]:

$$\frac{1}{F^2(\xi)} = \frac{\xi}{1 - e^{-\xi}}, \tag{3.16}$$

which is very close to the exact calculation using the filling factor over the area covered by disks [141]. By using left term in Eq. (3.12) and Eq. (3.9) the multiplicity and squared average transverse momentum are expressed as a function of the color suppression factor [157]:

$$\mu = \mu_1 N F(\xi), \tag{3.17}$$

$$\langle p_T^2 \rangle = \langle p_T^2 \rangle_1 / F(\xi). \tag{3.18}$$

I verified the value of $\mu_1 \sim 0.63$ of Eq. (3.17) from fit over data [158–166] shown in Fig. 3.6 (also with considering a specific geometry shape described below).

To calculate the filling factor ξ in terms of F, it is necessary to solve Eq. (3.16), the solution can be expressed in terms of the principal branch of the Lambert function W [154]:

$$\xi(F) = \frac{1}{F^2} + W\left(-\frac{\exp(-1/F^2)}{F^2}\right). \tag{3.19}$$

3.3 Energy dependence

The multiplicity dependence on the center of mass collision energy $\sqrt{s}$ is completely specified once the average number of strings in a pp collision is determined (see Eq. (3.17)). At very low energies, the number of string is ~ 2. Then, the number of strings N escalates with $\sqrt{s}$ for a minimum bias distribution as a power law [149]:

$$N = 2 + 4\frac{S_0}{S}\left(\frac{\sqrt{s}}{m_p}\right)^{2\lambda}, \tag{3.20}$$

with m_p the proton mass and $\lambda = 0.196 \pm 0.005$ a fit parameter determined as shown in Fig. 3.6.

For a large number of strings in an event, it is required to have a large number of partonic interactions which can be achieved at high collision energies or at a large number of colliding partons.

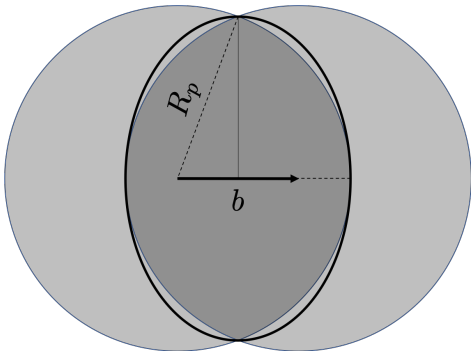

Figure 3.4: Elliptical interaction area in a pp collision with non-zero impact parameter $\vec{b}$, the major and minor semiaxes are $D = \sqrt{R_p^2 - (b/2)^2}$ and $d = R_p - b/2$ respectively.

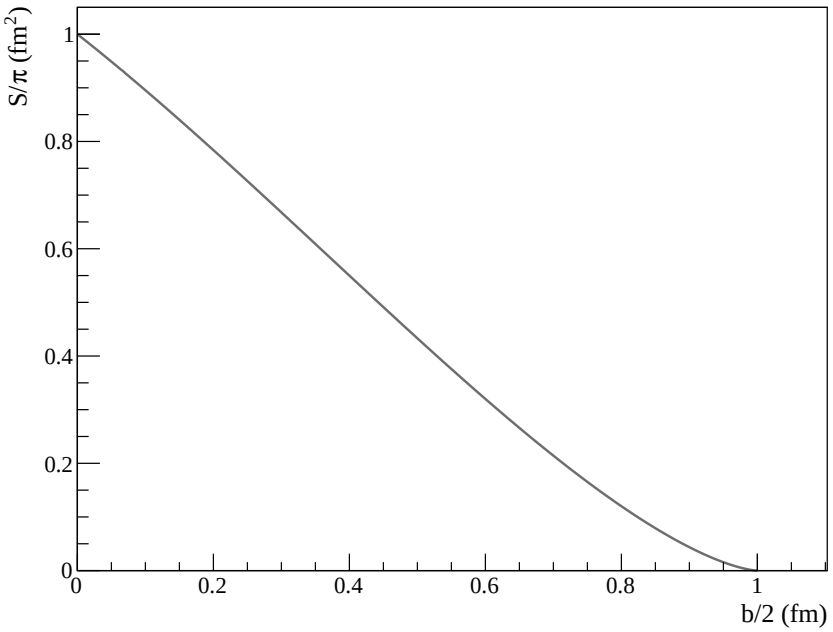

Figure 3.5: Dependence of the elliptical interaction area as a function of the impact parameter b.

In pp collisions the areas S and S_0 can be described in terms of the radii $r_0 \simeq 0.2385$ fm (the radius of a single disk [167–170]) and $R_p \simeq 1$ fm (the radius of a proton). However, to have a more precise description of the overlapping area, I define it as an ellipse in terms of an effective impact parameter b as seen in Fig. 3.4.

The interaction elliptical area in terms of b is:

$$S = \pi \left(R_p - \frac{b}{2} \right) \sqrt{R_p^2 - \left(\frac{b}{2} \right)^2}. \tag{3.21}$$

For $b \to 0$, Eq. (3.21) recovers the area of a circle $S \simeq \pi R_p^2$, the transverse size of a proton.

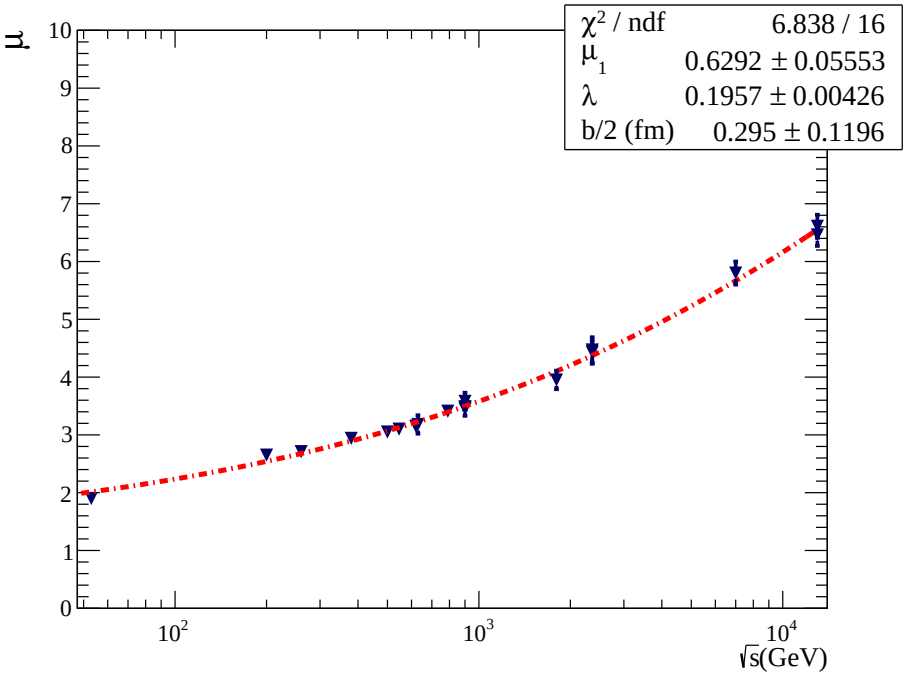

Figure 3.6: Fit over experimental data for multiplicity measured on minumum bias pp collisions from 53 MeV to 13 TeV [158–166].

3.4 Finite size effects on the CSPM

To make predictions for small collision systems, the parameter $F(\xi)$ is obtained from experimental measurements, assuming TL [149–152]. This approach has proven useful for predicting collective effects in small collision systems. However, it is important to note that these systems are still far from reaching thermalization and TL. In order to provide a more realistic description of the system, it is necessary to consider size effects [171]. Consequently, studies have been conducted to investigate

finite-size effects and various initial state conditions [156, 172, 173], which will be further explained below.

The classical CSPM picture considers a continuous plane with periodic boundary conditions to resemble an infinite surface, where, for a fixed string density and $N \to \infty$ the $F(\xi)$ dependence with ξ is [127, 141, 157]:

$$F(\xi) = \sqrt{\frac{1 - e^{-\xi}}{\xi}}, \tag{3.22}$$

The percolation threshold that marks the geometrical phase transition and the area covered by disks can be determined using Monte Carlo methods [172].

As I mentioned in the previous section, a deeper step in precision is to consider a finite interaction surface whose geometric shape is described by an ellipse parameterized by the effective impact parameter b. The eccentricity of the ellipse ϵ can be expressed in terms of b from:

$$\epsilon = \sqrt{1 - \frac{d^2}{D^2}} = \sqrt{\frac{b}{R_p + b/2}}, \tag{3.23}$$

which corresponds to $\epsilon = 0.675 \pm 0.055$ for the fit to pp minimum bias data.

To determine percolation thresholds, the critical density at which spanning cluster formation occurs must be estimated. The main percolation threshold in CSPM corresponding to TL is $\xi_c = 1.128$ [174]. But when different types of geometries began to be considered, the percolation parameter had to be estimated from Monte Carlo simulation. The first results of considering different distribution profiles, elliptical bounded systems and finite number of strings showed that there are shifts in the percolation thresholds [172].

3.4.1 Percolation threshold

The Monte Carlo results reveal notable finite-size effects when a non-periodic boundary is applied to the system, particularly when the number of strings is small. In this case, the percolation threshold exhibits a strong dependence on the eccentricity E for small values of N. This dependency arises from the cross-over length approaching the string diameter at eccentricities greater than 0.7. Additionally, the percolation threshold for elliptically bounded systems is observed to shift towards

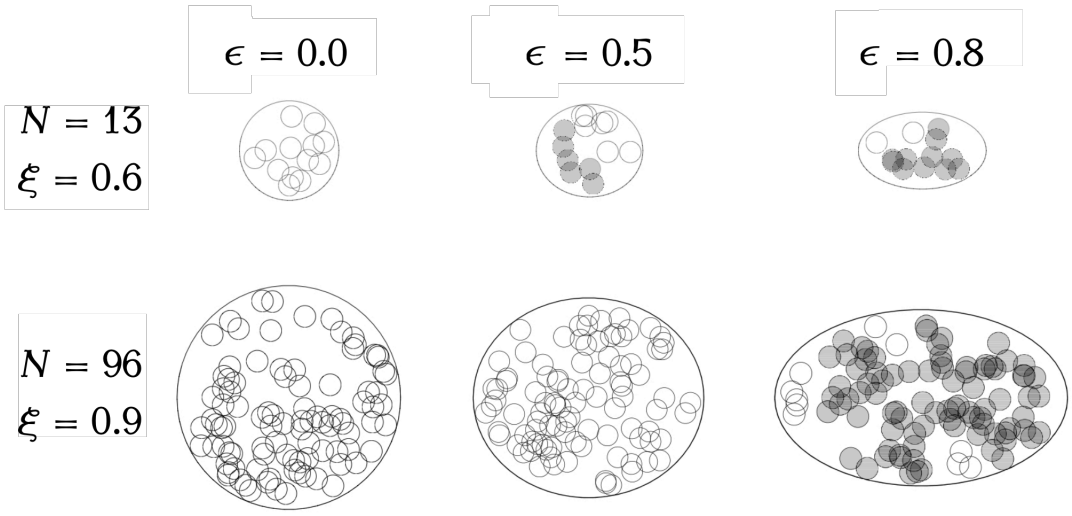

Figure 3.7: Spanning cluster as a function of the eccentricity for $N = 13$, 96 and different filling factor for uniform density profile. The filled circles are strings belonging to the spanning cluster (image taken from [172]).

smaller values compared to the case of a circular boundary. Moreover, at higher eccentricities, the system requires shorter distances to achieve percolation [172].

Furthermore, for small systems, there are no significant differences in the percolation threshold between the uniform and Gaussian profile distribution models. This can be attributed to the similarities in the spatial distribution of the disks inside the ellipse. However, in highly populated systems (large N values), the system becomes independent of the eccentricity as it approaches the TL. In the case of string percolation systems with a uniform density profile, the percolation threshold converges closer to the value of approximately 1.13, which has been reported for continuum percolation in the TL. Conversely, in Gaussian profile models, the spanning cluster consists of a larger number of strings compared to the Uniform model, given the same filling factor and eccentricity conditions [172], the samples of elliptical bouded systems are shown in Fig. 3.7.

3.4.2 Area covered by disks

The next crucial quantity to evaluate is the coverage area occupied by disks, given by $1 - \exp(-\xi)$ in the case of TL. To determine the fraction of the overall area covered by disks in string systems, it is necessary to generate percolating systems with

specific boundary conditions and density profiles. This is achieved by constructing an imaginary square lattice with a spacing of $2r_1$, centered on the geometric center of the boundary, as the examples of Fig. 3.8. This lattice facilitates the mapping of the string system onto a matrix representation. Subsequently, the fraction of the lattice cell area covered by disks is estimated using Monte Carlo integration [173].

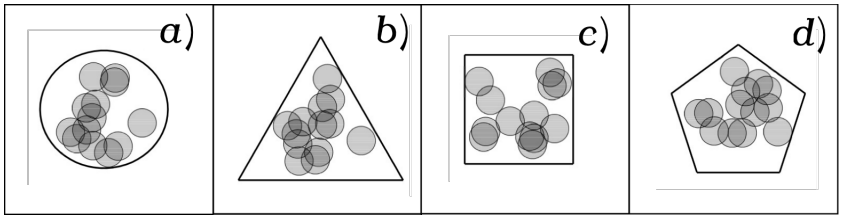

Figure 3.8: Samples of string percolating system at $\xi = 0.7$ with small number of disks ($N = 13$) for uniform density profile and different boundary shape condition (image taken from [173]).

The MC results reveal a clear dependence of the fraction of area covered by the disks on factors such as the number of disks, boundary shape, and density profile, particularly in small systems. However, as the number of disks, N, increases, the percolation system loses this dependency. This is because the behavior of the system becomes indistinguishable between very large circles (compared to the disk size) and other large geometric shapes such as ellipses or regular polygons. In essence, the system approaches behavior akin to the thermodynamic limit [173].

Modifications in the fraction of area covered by the disks in small and bounded systems introduce corrections to the color suppression factor, constituting a secondary contribution to color-damping arising from finite size and contour effects. Interestingly, this effect becomes more pronounced as deviation from circular geometries appears, with triangular systems exhibiting maximum suppression and even greater effects observed in highly eccentric ellipses ($\epsilon \to 1$). Although the color suppression factor exhibits small deviations from its thermodynamic limit value, even for systems populated by $N = 13$, it is crucial to consider the finite effects of size and shape for all relevant quantities when calculating observables [173]. These considerations lead to significant deviations from thermodynamic limit determinations, as elucidated in the subsequent sections.

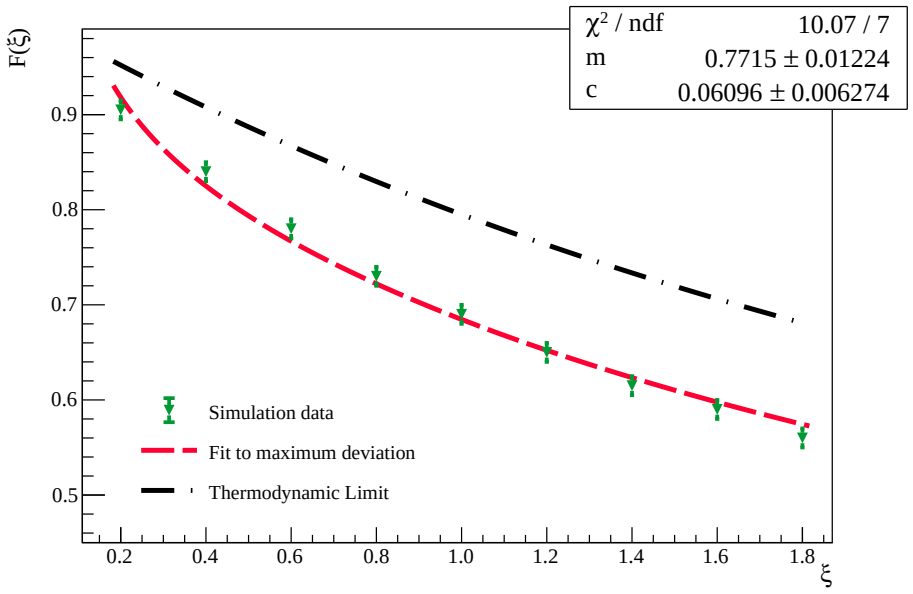

Figure 3.9: Color reduction factor as a function of ξ. The values that corresponds to the maximum deviation from thermodynamic limit obtained from MC clustering are shown in red marks, the fit of $F_s(\xi)$ is shown in blue dotted line, compared with $F(\xi)$ in green dotted line.

3.4.3 Color reduction factor not in the thermodynamic limit

To consider the maximum departure effect with respect to TL on $F(\xi)$ based on [173] I propose a modification to the color reduction factor adding an additional damping term that describes the effects found by analyzing the fraction of the area covered by disks considering finite size effects:

$$F_s(\xi) = m\sqrt{\frac{1-\exp(-\xi)}{\xi}} + c\sqrt{\frac{1+\exp(-\xi)}{\xi}}, \tag{3.24}$$

where $m = 0.7714731 \pm 0.01468$ is a weight parameter of the TL contribution to $F(\xi)$, the usual percolation model, and $c = 0.0609589 \pm 0.007527$ is the corresponding weight parameter of the deviation from nonTL in the percolating system. Notice that in the equation Eq. (3.24) when $c = 0$ (no extra damping from finite size effects is considered) and $m = 1$ the TL is recover Eq. (3.22).

$F_s(\xi)$ has a larger suppression effect above critical string density, though for regions right below critical string density which is a similar deviation to that reported in [151, 175].

Thus, it is now possible to explain the effects on a broader set of multiplicity experimental data [165, 176–183] and it can give a more precise description of the transport coefficients and bulk properties for temperature region below the critical temperature for nonTL systems, as I will show in the next chapter.

By utilizing a linear interpolation method, I estimated the effective region of $F(\xi)$ for such systems that are found between TL and nonTL. Moreover, such effective region was estimated by an uncertainties propagation method for the model-dependent observables.

3.5 Core-shell-color string percolation model

In [148] was proposed a hybrid core-shell model together with the traditional CSPM, called CSCSPM. The idea was to take into account an excluding or repulsive interaction between strings. To be precise, the authors introduced a concentric region of exclusion into the strings (core region, the rest of the string area is called the shell region) of diameter $\lambda\sigma$ ($0 \leq \lambda \leq 1$, σ denotes the diameter of the strings). They also introduced a probability q_λ that determines whether a string can overlap with another string in its core region, classifying strings as soft or hard depending on whether they permit such overlaps. It is important to note that this overlap condition applies solely to core-core interactions, as core-shell and shell-shell overlaps are permitted.

In the same way that their predecessor, the CSCSPM model explains particle production in collision physics through the formation of string clusters (same strings as in the CSPM). Notice that the hard strings act as a fluid of hard disks of diameter $\lambda\sigma$, while the soft ones are still ideal particles. Moreover, the parameter q_λ modules the number of hard strings distributed in the system. However, the structures and phenomenology of the system depend on the combinations of both parameters. For example, if $\lambda = 1$ and $q_\lambda = 0$, the system recovers the picture of a fluid of hard disks [184], which may exhibit a liquid structure for densities above a particular string density. This condition prevents the formation of clusters, and then each string should produce charged particles individually, but on average, their transverse momentum squared will be the corresponding of one string divided by the multiplicity. This mechanism inhibits the formation of charged particles with higher transverse momentum. Also, if $q_\lambda = 0$, the model reproduces the continuum

percolation of disks with hard cores [185, 186]. Finally, If $\lambda = 0$ or $q_\lambda = 1$, the system corresponds to traditional 2D continuum percolation [174, 187], which is the geometric picture of the CSPM.

It was found in Ref. [148] that combinations of parameter values exist such that, at the same time, allow the system the clustering of color strings and the formation of coordination shells, the main indications of the changes in the structure of the system.

Chapter 4

Structure of the medium formed in heavy ion collision

As mentioned previously, the QGP is a state of matter believed to have existed shortly after the Big Bang in the early universe. The concept of QGP was first proposed in the 1970s [34–36] as a way to understand the behavior of high-energy collisions involving atomic nuclei. In the late 1990s, experimental evidence emerged supporting the creation of QGP. The collision of heavy ions, such as AuAu at RHIC, produced a "liquid" state composed of quarks and gluons. This liquid exhibited an unusually low ratio of shear viscosity to entropy density compared to any other known material [53,56,57]. These findings were later confirmed in PbPb collisions at the LHC [73,75,188]. Similar properties have also been observed in other collision types, including pp and pA collisions at the LHC [80], as well as dAu and ^{3}HeAu collisions at RHIC [189].

In this chapter, I explore the structure of the medium created in ion collisions using the CSPM [124,127,141,153], its core-shell modified version (CSCSPM) [148], and the CGC framework [190,191]. Specifically, I demonstrate how these models successfully predict the liquid-like behavior of the QGP.

One way to analyze the physical structure of a system is by examining the radial distribution function (RDF), denoted as $g(r)$, which describes the variation in average particle count as a function of distance r from a given point. This function is commonly used to evaluate packing structures and provides valuable information about long-range correlations and particle organization [192]. The structure of a system can be inferred from $g(r)$ as follows:

- A flat function indicates an ideal gas structure.

- The presence of a peak signifies a non-ideal gas with more ordered behavior.
- Multiple peaks in $g(r)$ indicate a liquid-like structure with increasingly smaller peaks.

4.1 Simulation results

To estimate the RDF, the following steps were employed:

1. Generation of System Samples: Simulations were performed by generating square boxes of size $L = 8\sigma_\circ$, where $\sigma_\circ$ represents the characteristic diameter of the objects distributed in the transverse plane of each model. These boxes serve as representative samples of the systems under investigation.

2. Generation of Suitable Configurations: Appropriate configurations of the system were generated to satisfy the conditions specific to each model. These configurations account for the relevant properties and interactions within the system, ensuring that they align with the corresponding model's requirements.

3. Calculation of the Radial Distribution Function: This function provides insights into the structure of matter by analyzing variations in the positions of its constituents, specifically the average local density of objects at a distance r from a reference object. The RDF serves as a quantitative measure of the organization and spatial arrangement of particles within the simulated system.

By following these steps, it can estimates the radial distribution function, which played a crucial role in characterizing the structural properties of the investigated systems.

The radial distribution function is estimated as follows

$$g(r) = \frac{n(r)L^2}{N(2\pi\Delta r(r + 0.5\Delta r) + \pi\Delta r^2)}, \tag{4.1}$$

where $n(r)$ is the average number of objects at a distance between r and $r + \Delta r$ from a trial disk allocated on the center of the square box, and N is the number of objects distributed on the square box.

In the subsequent analysis, I delve into the intricacies of the simulation process and the structures observed within the CSPM, CSCSPM, and CGC. To facilitate a comprehensive comparison between the models, the RDF is computed over a range of distances, specifically from 0 to 3.5 times the characteristic diameter $\sigma_\circ$, with increments of $\Delta r/\sigma_\circ = 0.035$.

By examining $g(r)$ within this distance range, it can gain valuable insights into the spatial arrangement and correlations among the constituents of the simulated systems. This approach allows for a detailed assessment of the unique characteristics exhibited by each model and enables meaningful comparisons between their respective structural properties.

Note that by performing these computations and analyzing the resulting $g(r)$ values, a comprehensive understanding of the simulated systems and discern the distinguishing features of the CSPM, CSCSPM, and CGC models can establish.

4.1.1 CSPM structure

In the previous chapter, I discussed the nature of the CSPM where strings are treated as fully penetrable disks. This representation is analogous to a classical ideal gas, and its influence is reflected in the RDF.

In the CSPM simulations, the framework of two-dimensional continuum percolation of disks is followed. This means that color strings are uniformly and randomly distributed within a square box, without any restrictions on overlapping between them. Once a total of N disks have been added to the system, the radial distribution function is computed using equation (4.1), as described in previous work [148].

Interestingly, regardless of the string density, the analysis has revealed that $g(r)$ exhibits a flat function in the CSPM. This observation is demonstrated in Figure 4.1, which presents the results of $g(r)$ for the CSPM with different string densities.

The flat behavior of $g(r)$ in the CSPM indicates a homogeneous distribution of strings throughout the system. It suggests that the CSPM, resembling an ideal gas, lacks any discernible long-range correlations or structural organization beyond the random placement of color strings.

Further investigation and analysis of $g(r)$ within the CSPM framework have provided valuable insights into the characteristics of the model and its implications for the distribution and arrangement of color strings in the simulated systems.

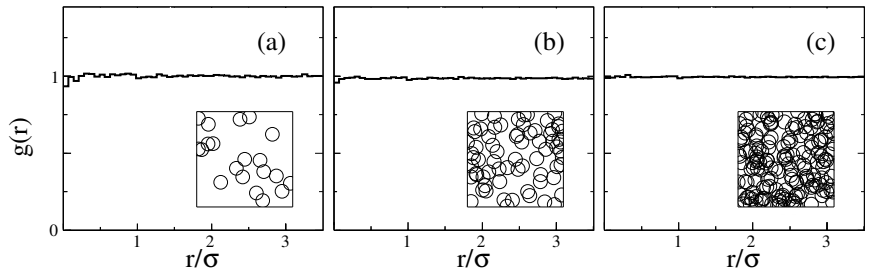

Figure 4.1: Radial distribution function for CSPM systems [193].

The ideal gas structure of the Color String Percolation Model (CSPM) arises due to the fully overlapping strings, which prevent the formation of coordination shells or any distinct structural organization. However, it is important to note that the overlapping between strings gives rise to the distinctive phenomenology observed in the CSPM, as well as in the Core-Shell modified CSPM (CSCSPM).

It is worth mentioning that considering the CSPM as an ideal gas with a very low density would not provide meaningful results due to the absence of color string clusters. In an ideal gas scenario, where the particles are widely separated, the relevant effects and phenomena associated with color string interactions and clustering would not be captured.

Notably, other researchers have also predicted the ideal gas behavior of the CSPM in their studies. For example, the finite-size analysis of the speed of sound, which inspires the extra damping term in the CRF [173], the investigation of the electrical and thermal conductivity of the QGP [194, 195], and their findings supported an ideal gas description of the system.

The consistency of these findings from multiple studies reinforces the understanding of the CSPM as an ideal gas-like system, emphasizing its unique characteristics and highlighting its suitability for investigating various properties and phenomena associated with color string interactions and the QGP.

4.1.2 CSCSPM structure

As mentioned earlier, the CSPM exclusively represents systems with an ideal gas structure due to the fully penetrable nature of the color strings. However, by introducing a repulsive interaction between the strings, other structures such as

non-ideal gas or liquid-like behavior can be observed, as demonstrated in the Core-Shell modified CSPM (CSCSPM).

In the CSCSPM, the configurations are generated using the random sequential addition algorithm, which involves adding disks one by one. In each step of the algorithm, a test string is randomly placed within the square box and designated as either soft or hard. The acceptance or rejection of the test string, along with its neighboring strings, is determined by the values of λ and q_λ, ensuring the validity of the configuration. If the test string does not satisfy the conditions, it is rejected, and the process repeats with a new test string. This procedure continues until the system is filled with the desired number of N strings. Once the CSCSPM configuration is generated, the radial distribution function $g(r)$ is computed using equation (4.1).

Figure 4.2 showcases samples of core-shell-color string systems created using the aforementioned algorithm, along with their corresponding radial distribution functions. To obtain the radial distribution function, the results over 10^6 realizations is averaged, allowing to capture the characteristic behavior of the system.

This analysis of the CSCSPM provides valuable insights into the structural properties and correlations of core-shell modified color string systems, highlighting the diverse range of behaviors that can be observed by incorporating a repulsive interaction between the strings.

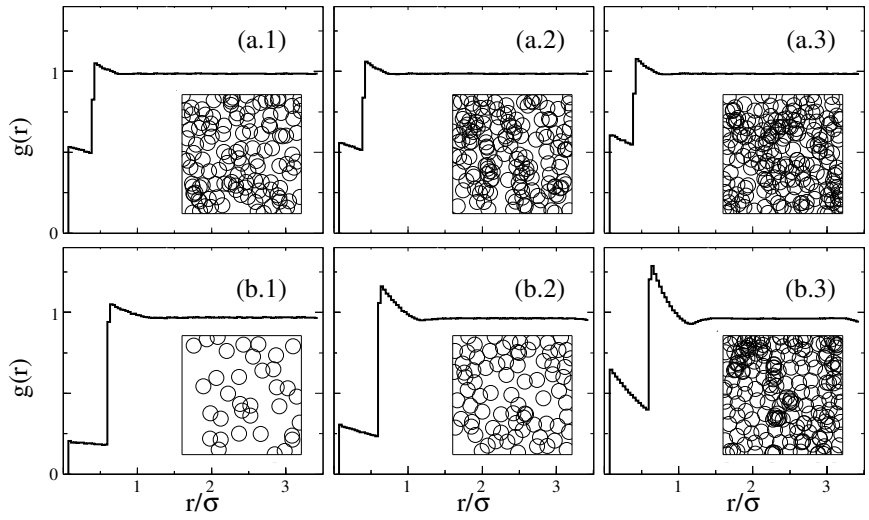

Figure 4.2: Samples of systems for the CSCSPM along with their corresponding radial distribution function. Note that in (b.2) and (b.3), it is observed a transition from non-ideal gas to liquid-like structures [193].

The CSCSPM offers the advantage of allowing for more complex structures beyond the ideal gas behavior. In a previous study [148], it was discovered that specific values of λ and q_λ result in the formation of liquid-like structures within the systems, as depicted in Figure 4.2 (b.3). This finding highlights the model's ability to capture the emergence of non-ideal gas behavior.

Furthermore, it is worth noting that the CSCSPM predicts that the structural and geometrical transitions occur almost simultaneously, with only a slight temperature difference of 1 MeV. This indicates a close relationship between the formation of specific structures and the system's thermodynamic properties. Figure 4.3 provides a representative sample of a CSCSPM system, showcasing its liquid-like structure along with the presence of a spanning cluster.

By elucidating the connection between the values of λ and q_λ, the emergence of different structures, and the associated thermodynamic transitions, the CSCSPM offers valuable insights into the complex behavior and phase transitions within core-shell modified color string systems.

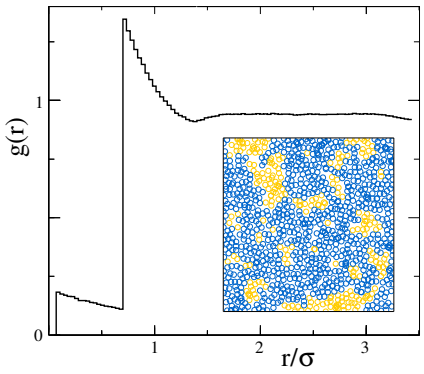

Figure 4.3: Sample of a system that shows a liquid-like structure together with the spanning cluster. This occurs with a difference in transition temperatures (configurational and geometric) lower than 1 MeV [193].

4.1.3 CGC structure

To investigate the structural properties of systems described by the CGC model, it is crucial to understand the distribution of the saturation scale Q_s^2 and the running coupling α_s. These quantities dictate the initial conditions for the distribution of gluons and their interactions. In the analysis, it was consider that Q_s^2 follows a Log-normal distribution, as described by Eq. (2.20).

To simulate the values of Q_s^2, the normal distribution was used. Each value of Q_s^2 is obtained as $Q_s^2 = \langle Q_s^2 \rangle e^x$, where x is a random number drawn from a normal distribution $\mathcal{N}(0,1)$. Here, $\langle Q_s^2 \rangle$ represents the average value of Q_s^2. The determination of $\langle Q_s^2 \rangle$ involves analyzing experimental data, which allows us to calibrate and adjust the model accordingly.

To compute the values of the running coupling α_s at zero order, the modified minimal subtraction scheme ($\overline{MS}$) is employed. This scheme provides a systematic and well-defined approach for evaluating the values of α_s in the CGC model.

By incorporating these techniques, we gain insights into the structural properties of the CGC systems and their behavior under different conditions. The interplay between the distribution of Q_s^2 and the running coupling α_s elucidates the underlying dynamics and helps to explain various experimental observations. Thus

$$\alpha_s(Q_s^2) = \frac{4\pi}{\beta_0 \ln(Q_s^2/\Lambda_{\text{QCD}}^2)}, \tag{4.2}$$

with $\beta_0 = 11 - 2n_f/3$, and Λ_{QCD}^2 being the QCD scale.

To determine the value of β_0, I consider a flavor number of $n_f = 3$ and take $\Lambda_{\mathrm{QCD}} = 0.332$ GeV [196]. It is worth noting that Λ_{QCD} acts as a cutoff for the Q_s values, as lower values of Q_s lead to nonphysical values of α_s.

In Figure 4.4, I present a sample of Q_s values and their corresponding α_s values computed using (4.2). Additionally, I provide histograms to visualize the distribution of Q_s and α_s. This analysis allows us to understand the relationship between Q_s and α_s and provides insights into the behavior of these quantities within the CGC framework.

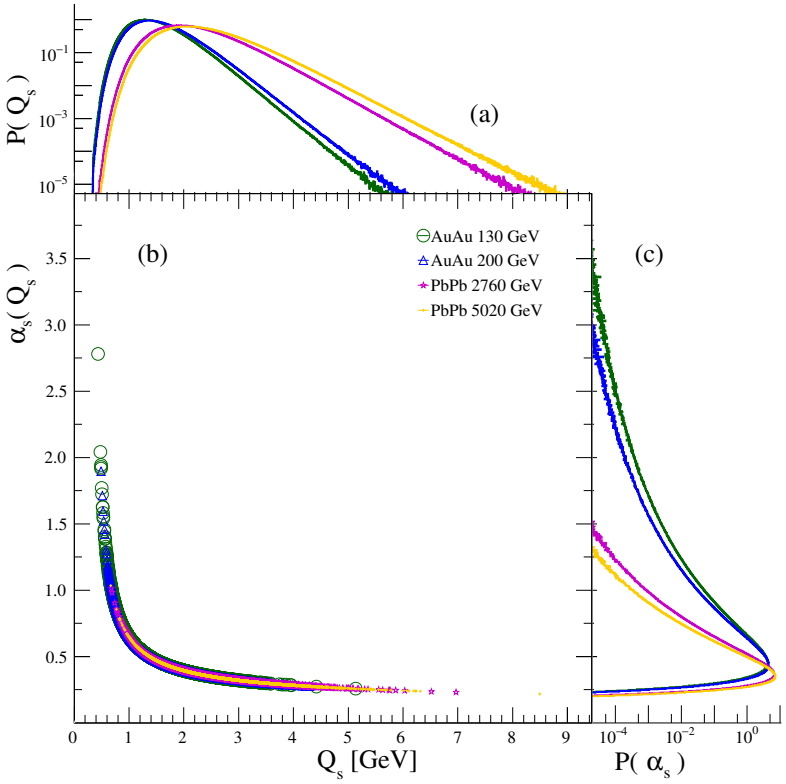

Figure 4.4: (a) Probability density function of Q_S. (b) Sample of α_s-values as a function of Q_s. (c) Probability density function of α_s of the systems under study: AuAu at $\sqrt{s} = 130$ GeV (green lines and circles), AuAu at $\sqrt{s} = 200$ GeV (blue lines and triangles), PbPb $\sqrt{s} = 2760$ GeV (magenta lines and stars), and PbPb $\sqrt{s} = 5020$ GeV (yellow lines and crosses.) [193].

The Lorentz-contracted nuclei in a nuclear collision confine the partons to a flat region on the transverse plane. The Glasma fields that emerge from these collisions are assumed to be proportional to the number of particles produced in a

central pseudorapidity region at the saturation scale [113]. In the low transverse momentum regime, the saturation scale is given by SQ_s^2/α_s [84, 107], where S represents the overlapping area of the nuclei. From these relations, the gluon density can be expressed as:

$$\rho = \frac{Q_s^2}{\alpha_s}. \tag{4.3}$$

Considering the saturation scale and the running coupling as random variables, the gluon number density is expected to exhibit random fluctuations, as illustrated in Figure 4.5 (a). Consequently, the average minimum distance between gluons, computed from the gluon cross section, denoted as $\xi = 1/\sqrt{\rho}$, is also a random variable, as depicted in Figure 4.5 (b).

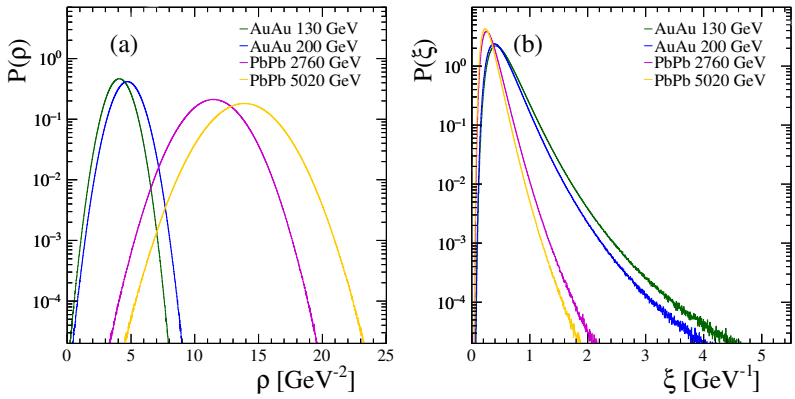

Figure 4.5: Probability density function for (a) the gluon density and (b) the minimum distances between gluon centers [193].

For the simulations, it is assume that the system is homogeneous and isotropic in AA central collisions (0-6% centrality). As a length scale, the average value of the gluon diameter is used, which is given by $\sigma = 2\langle r_g \rangle = 2\langle 1/\sqrt{\pi\rho} \rangle$.

Following the same procedure as in the CSPM and the CSCSPM, a square box with a side length of $L = 8\sigma$ is construct. Therefore, the number of gluons in the system is given by $N_g = 64\sigma^2\rho$.

Furthermore, the probability of observing a system with exactly N_g gluons is calculated as usual:

$$P(N_g) = \int_X P(\rho) d\rho, \tag{4.4}$$

where X represents the interval of ρ-values that satisfy $\lfloor L^2\rho \rfloor = N_g$. Figure 4.6 (a) displays the probability mass distribution for the gluon number obtained from the

simulations. This distribution takes into account all the fluctuations arising from the conditions of the CGC model and is crucial for computing the average of the radial distribution function.

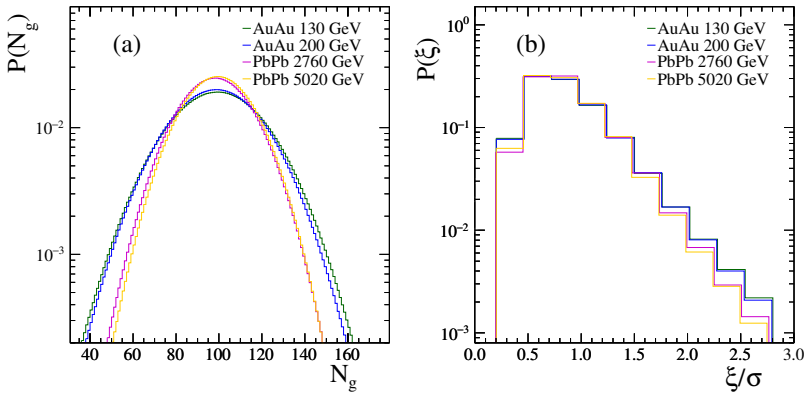

Figure 4.6: Used histograms for simulation (a) the number of gluons in the square and (b) classes of minimum distances among gluons normalized by the average diameter of a gluon [193].

To ensure valid configurations of gluon positions in the simulations, a criterion based on the probability density function of the minimal distance between nearest neighbor gluons is employed. Similar to the number of gluons N_g, the discretized probability density function is used as follows. The interval of ξ-values for which $P(\xi) > 0.01$ is considered. In the systems analyzed in this manuscript, this event has a probability of occurrence of 0.9968, 0.9971, 0.9985, and 0.9986, respectively. The interval is then divided into ten equally sized sub-intervals, where the probability of observing the i-subdivision is given by

$$P(i) = \frac{\int_{X_i} P(\xi) d\xi}{\int_{\bigcup_{i=1}^{10} X_i} P(\xi) d\xi}, \tag{4.5}$$

which produces the histograms depicted in Fig. 4.6 (b). This approach imposes two restrictions on the random variable ξ with zero probability, namely, (i) $\xi/\sigma < 0.2$, and (ii) $\xi/\sigma > 2.8$.

The simulation is initialized by placing a trial gluon at the center of a square box with a side length of $L = 8\sigma = 16\langle r_g \rangle$. Then, $N - 1$ gluons are added one by one, ensuring that the minimal distance between nearest neighbor gluons satisfies $0.2 < \xi/\sigma < 2.8$. After the addition of the N gluons, the system is thermally

equilibrated by performing moves on individual gluons (excluding the trial gluon). For each test gluon, a virtual random position is generated within a neighborhood of the actual position, taking into account periodic boundary conditions. The distance ξ' to the nearest gluon is calculated, and a uniformly random number within the interval $(0, 1)$ is generated. The virtual position is accepted if $P(\xi') > x$, where $P(\xi')$ is obtained from the distribution in Fig. 4.6 (b). If the position is rejected, the process is repeated for another gluon. This procedure is repeated for 10^4 moves per particle.

After thermalization, the number of particles $n(r, N)$ within a distance between r and Δr is measured from the trial gluon, considering a system with N particles. Samples of the systems after thermalization for AuAu and PbPb collisions at $\sqrt{s} =$ 130 GeV, $\sqrt{s} = 200$ GeV, $\sqrt{s} = 2760$ GeV, and $\sqrt{s} = 5020$ GeV are shown in Fig. 4.7. To maintain consistency, the same parameters used for the CSPM and CSCSPM models in constructing the plot of $g(r)$ are employed.

New valid configurations are generated by moving a random gluon as described before and measuring $n(r, N)$ again after 100 moves per gluon. Finally, the average of the number of gluons $n(r, N)$ is computed over 10^4 simulation runs.

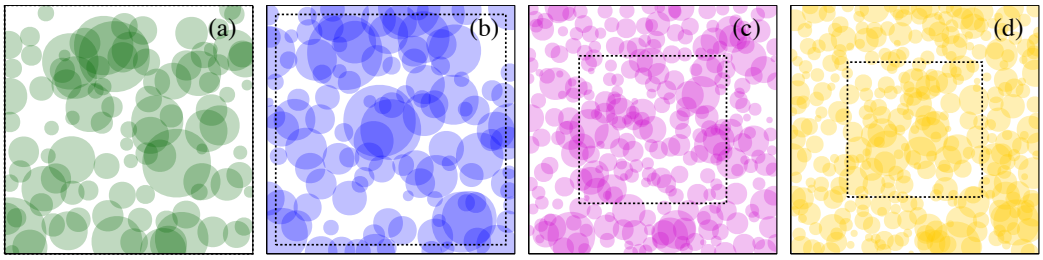

Figure 4.7: Samples of generated systems in the picture of the CGC after the thermalization for (a) AuAu collisions at $\sqrt{s}$ =130 GeV, (b) AuAu collisions at $\sqrt{s}$ =200 GeV, (c) PbPb collisions at $\sqrt{s}$ =2760 GeV, and (d) PbPb collisions at $\sqrt{s}$ =5020 GeV. These systems correspond to a square box of around 1fm^2. The inner dashed square is the size of the simulated system for the purposes of the computation of the radial distribution function [193].

The number of gluons in the system exhibits fluctuations depending on various factors such as center-of-mass energy, centrality classification, pseudorapidity, and nucleon number. To account for these fluctuations, the average of the radial

distribution function is determined using the following expression:

$$g(r) = \frac{\sum_{N=N_{\min}}^{N_{\max}} \frac{L^2 n(r,N)}{N(2\pi\Delta r(r+0.5\Delta r)+\pi\Delta r^2)} P(N)}{\sum_{N=N_{\min}}^{N_{\max}} P(N)}, \tag{4.6}$$

where $P(N)$ corresponds to the distribution of the number of gluons shown in Fig. 4.6 (a). The values of $N_{\min}$ and $N_{\max}$ are determined as $N_{\min} = \lfloor \langle N_g \rangle \rfloor - 3 \left\lfloor \sqrt{\text{var}(N_g)} \right\rfloor$ and $N_{\max} = \lfloor \langle N_g \rangle \rfloor + 3 \left\lfloor \sqrt{\text{var}(N_g)} \right\rfloor$ respectively.

Figure 4.8 provides a summary of the results for the radial distribution function in AuAu and PbPb central collisions at $\sqrt{s} = 130$ GeV, 200 GeV, 2760 GeV, and 5020 GeV respectively.

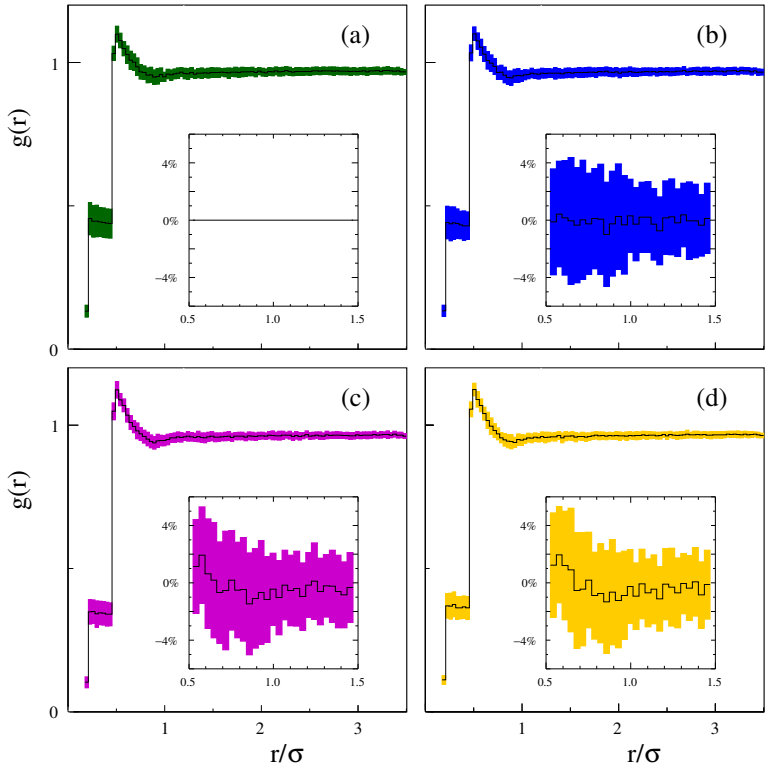

Figure 4.8: Radial distribution function of systems in the picture of the CGC for (a) AuAu collisions at $\sqrt{s}$ =130 GeV, (b) AuAu collisions at $\sqrt{s}$ =200 GeV, (c) PbPb collisions at $\sqrt{s}$ =2760 GeV, and (d) PbPb collisions at $\sqrt{s}$ =5020 GeV. The inner plots correspond to the percentage of deviation of the radial distribution function from the one obtained for AuAu collisions at $\sqrt{s}$ =130 GeV [193].

By adopting three different models, CSPM, CSCSPM, and CGC, the structure

of the medium formed in heavy-ion collisions can be investigated. The radial distribution function of the distributed transverse representation of color flux tubes was examined within each model.

The color string percolation model, due to the complete overlap condition of the strings, exhibits a structure resembling that of an ideal gas. However, the introduction of repulsive-like interactions between strings in the CSCSPM leads to the emergence of more complex structures, resembling a gas of interacting particles or a liquid-like fluid. The CSCSPM introduces two new characteristics of color strings: a concentric core region and a probability for core-core interactions. This results in a classification of strings as soft or hard, acting like ideal particles or hard disks with a diameter of $\lambda\sigma$, respectively.

Through fine-tuning of the CSCSPM parameters (λ, q_λ), the system undergoes a structural phase transition simultaneous with a geometrical phase transition. The former corresponds to a transition from a gas-like structure to a liquid-like one, while the latter signifies the formation of the spanning cluster of color strings, which can be interpreted as the onset of quark-gluon plasma formation. The CSCSPM predicts that these transitions occur almost simultaneously, with a temperature difference of 1 MeV.

Another aspect investigated is the color glass condensate, where the stochastic CGC framework accounting for fluctuations in the saturation scale Q_s^2 is employed. This leads to fluctuations in the running coupling as well as in other characteristics of the CGC, including density, gluon size, and minimal distances between nearest neighbor gluons. For AuAu central collisions at RHIC energies (130 and 200 GeV), the distribution of gluons corresponds to a gas of interacting particles. In contrast, evidence of a liquid-like structure is observed for PbPb central collisions at LHC energies (2760 and 5020 GeV). However, further simulations are necessary to smooth the radial distribution function shown in Fig.4.8 and apply a similar analysis to the $g(r)$ function as described in Ref. [148].

It should be noted that while the simulated system representations assume homogeneity and isotropy at the center of the transverse plane during collisions, the system may become diluted towards the edges. As a result, the radial distribution function may resemble that of a diluted non-ideal gas, and possibly exhibit characteristics of an ideal gas (flat function).

Chapter 5

Model thermodynamical quantites

5.1 Thermal Distribution

The initial state properties can be described by introducing the local thermodynamic quantities in terms of $F_s(\xi)$. ξ rules the cluster distribution, and in consequence, the behavior of all thermodynamic quantities, such as temperature which involves the Schwinger mechanism for non-massive particles. The strings with higher tension x will break producing $q\bar{q}$ and qq-$\bar{q}\bar{q}$ pairs which later on will combine and hadronize. So, the transverse momentum distribution of charged particles is given by [197]:

$$\frac{dN}{dp_T^2} \sim \exp\left(-\pi\frac{p_T^2}{x^2}\right). \tag{5.1}$$

The mean tension of the string $\langle x^2\rangle$ fluctuates around its mean value describing a Gaussian distribution of the fluctuations which convolutes with (5.1) giving a thermal-like distribution characterized by the mean transverse momentum of a single string $\langle p_T^2\rangle_0 = \langle x^2\rangle F(\xi)/\pi$ [141, 167]:

$$\frac{dN}{dp_T^2} \sim \exp\left(-p_T\sqrt{\frac{2F_s(\xi)}{\langle p_T^2\rangle_0}}\right), \tag{5.2}$$

from where I estimate the temperature:

$$T(\xi) = \sqrt{\frac{\langle p_T^2\rangle_0}{2F_s(\xi)}}. \tag{5.3}$$

The critical string density depends on the system's characteristics [156, 172, 173]. I consider the critical temperature in terms of critical string density ξ_c = 1.128 [174]

in the same way as [149, 198], where $T_c = T(\xi_c)$, so that, in TL:

$$\frac{T}{T_c} = \sqrt{\frac{F(\xi_c)}{F(\xi)}} = \frac{0.879947816}{\sqrt{F(\xi)}}. \tag{5.4}$$

Furthermore, I also see a shift in the critical temperature, now reached at lower ξ for $F_s(\xi)$. I consider the critical temperature $T_c = 154 \pm 9$ [41], and its respective deviations with ξ to estimate an effective area of the observables in function of T/T_c.

5.2 Energy density

Energy density ε is an order parameter in the phase transition from Hadron Gas (HG) to QGP, so it is natural to think that there is a direct relation between string density ξ and energy density ε, given that ε is the order parameter that characterizes phase transitions in AA collisions and ξ is the local order parameter in the SPM geometric phase transition [141].

In references [141, 199, 200], energy density from the Bjorken boost invariant 1D hydrodynamics formula [36] is found to be proportional to ξ. Given that each initial state string can be interpreted as the extended fields among the interacting partons, which has a direct contribution to energy density. This key idea holds for small collision systems [149, 150]. Consequently, we use the following relation to estimate energy density:

$$\varepsilon = \varsigma\xi, \tag{5.5}$$

where we found in the same way as [199] that $\varsigma = \varepsilon_c/\xi_c = 0.5601$ GeV/fm^3, and see a shift in the critical temperature $T_c(F_s)/T_c(F) = 1.096$ with respect to the TL scenario.

As we can see in Fig. 5.1, the behavior of the energy density over T^4 as a function of T/T_c agrees with Lattice's calculations [202].

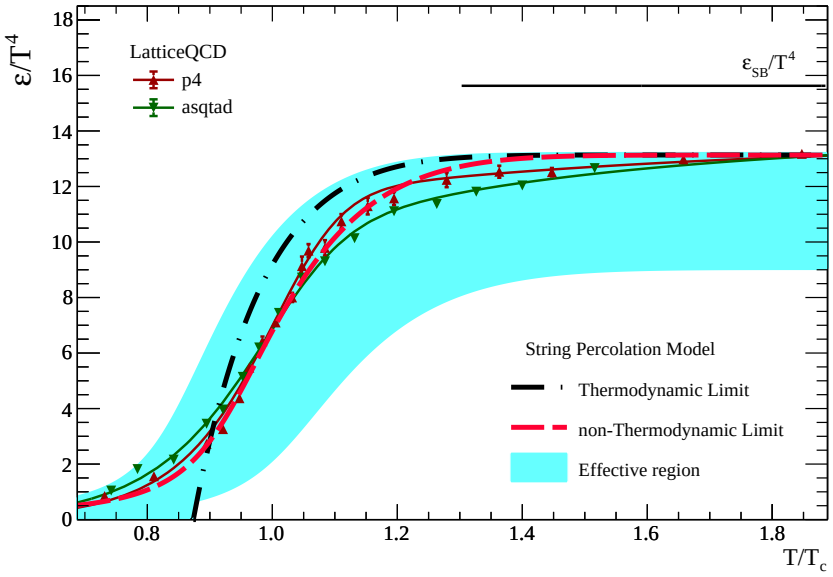

Figure 5.1: Energy density over T^4 behavior respect to T/T_c. The cyan area shows the effective region estimated with shifts in the Color Reduction Factor. The red dashed line shows the energy density computed in nonTL with $F_s(\xi)$, Eq. (3.24) [201]. While the black dotted-dashed line is the TL calculation using $F(\xi)$, Eq. (3.22) [141]. We include a comparison with Lattice QCD computations using staggered fermion actions p4 (maroon triangles) and asqtad (green triangles) with their respective parametrization (continuum lines) [202].

5.3 Shear viscosity

The observable behavior of the elliptic flow suggests that matter created in AA collisions behaves as a near-perfect fluid with a very low viscosity [53–56, 73–77]. It was proposed the indirect measurement of the shear viscosity over entropy density as a probe of the viscosity of the medium created in the collision. More recently, this probe has shown signs of a strongly interacting medium in small collision systems as well [78–80, 203, 204].

It is possible to estimate the transport coefficients not in thermodynamic equilibrium, assuming that the medium expands as a function of the initial state properties, as was initially proposed in [199].

For computing the ratio of shear viscosity, over entropy density η/s in terms of the SPM parameters we considered the relation given by the relativistic kinetic

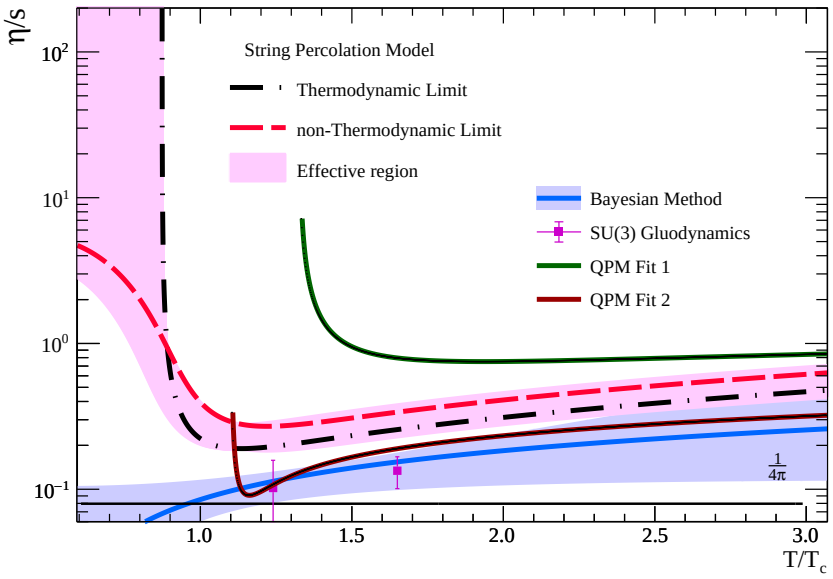

Figure 5.2: Ratio of shear viscosity over entropy density as a function of T/T_c calculated on the SPM framework, the red dashed line corresponds to the η/s computation on the nonTL using $F_s(\xi)$ that considers geometry effects on the mean free path, the black dotted-dashed line is the computation in TL using $F(\xi)$ as reported in [149], and the pink area is the estimate effective region [201]. The results from Bayesian Method [205] are shown in the violet region. The limit of AdS/CFT ($\eta/s \geq 1/(4\pi)$) from [66] is included (black continuum line). The magenta squares correspond to the Lattice calculation in SU(3) gauge theory [206]. The green and red solid lines corresponds to the fits for quasiparticle excitations with medium-dependent self-energies (QPM) [207].

theory [208], which was also previously used for small collision systems [149, 150]:

$$\frac{\eta}{s} = \frac{T\lambda}{5}, \tag{5.6}$$

where $\lambda = 1/(n\sigma_{tr})$ is the mean free path, with n the number density of an ideal gas of partons and σ_{tr} the transport cross section of its constituents. The number density is directly extracted from the initial number of strings damped by $F(\xi)$, which gives the collective effects of the medium:

$$n = \frac{N_s F(\xi)}{SL}, \tag{5.7}$$

where $L \sim 1$ fm is the longitudinal extension along the beam axis, with N_s and S as defined previously. In the same way, the transport cross section is given by $\sigma_{tr} = S_0 F(\xi)$, the transverse size of a single string multiplied by $F(\xi)$ [199]. This leads us to estimate the mean free path using the definition of the string density from Eq. (3.13):

$$\lambda = \frac{1}{n\sigma_{tr}} = \frac{SL}{S_0 N_s F^2} = \frac{L}{\xi F^2}. \tag{5.8}$$

From which:

$$\frac{\eta}{s} = \frac{TL}{5\xi F^2}. \tag{5.9}$$

Note that ξF^2 is the area covered by color sources, which is $1 - e^{-\xi}$ in the case of TL [173].

The results on η/s show that its minimum value for TL associated with $F(\xi)$ is reached at $T/T_c = 1.13187$, while the one associated with $F_s(\xi)$ for nonTL is reached at $T/T_c = 1.22508$; the results show an increase in the minimum value of η/s by a factor of 1.4218 from 0.190018 for TL to 0.270179 for nonTL as shown in Fig. 5.2.

Trace anomaly Δ measures the deviation with respect to the conformal behavior and identifies residual interactions in the medium formed [211–213]. It is expected that this observable is related to the medium's viscosity properties. In previous works, it has been observed qualitatively that the trace anomaly can be approximated as the inverse of shear viscosity over entropy density [198, 214]:

$$\Delta \equiv \frac{\varepsilon - 3P}{T^4} \simeq \frac{s}{\eta_s}. \tag{5.10}$$

Trace anomaly as well as the viscosity coefficients are susceptible to QGP phase transition [215]. The behavior of the trace anomaly for nonTL goes accordingly to that reported by Wuppertal-Budapest Collaboration [210] and HotQCD Collaboration [209], showing a maximum for TL in $T/T_c = 1.13621$ and maximum value $T/T_c = 1.21918$ for nonTL (Fig. 5.3).

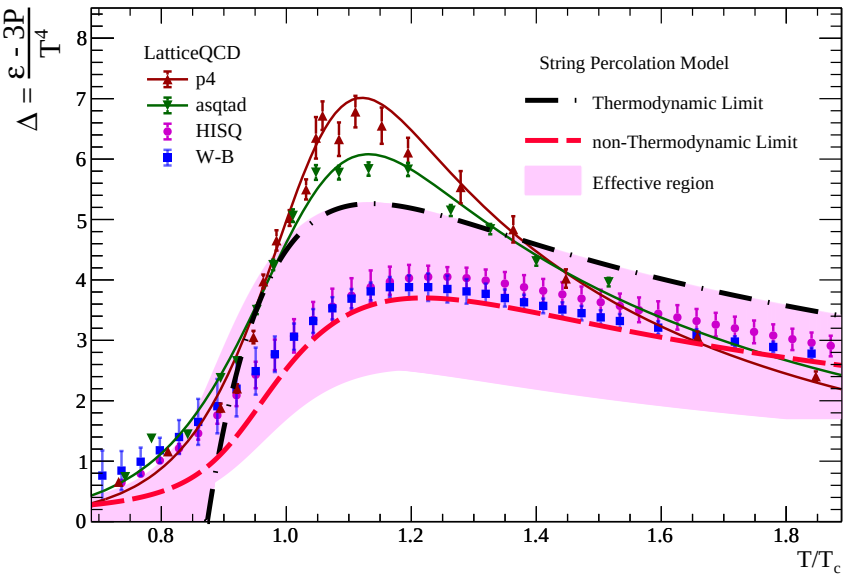

Figure 5.3: Behavior of the trace anomaly respect to T/T_c using the inverse of η/s in TL (black dotted-dashed line) and nonTL (red dashed line) limits and the effective region (pink area) in the SPM framework [201]. The results from Lattice QCD 2+1 flavor QCD-EoS using staggered fermion actions p4 (maroon triangles) and asqtad (green triangles) with their respective parametrization (continuum lines) [202]. The continuum extrapolated results from the HotQCD Collaboration of highly improved staggered quark action (HISQ) [209] and from the Wuppertal-Budapest Collaboration (W-B) using the Symanzik improved gauge and a stout-link improved staggered fermion action [210] are shown in magenta circles and blue squares respectively.

Pressure P is obtained from Eq. (5.10) and from the first law of thermodynamics ($Ts = \varepsilon + P$ [36]) we calculated the entropy density s of the system. See the results of $3P/T^4$ and s/T^3 respectively in Fig. 5.4. A comparison with LQCD [202] is also shown.

However, the SPM results surpass the value of the thermodynamic quantities in the range of temperature below $1.5T_c$. Pressure begins saturation over $3T_c$. For this reason, we can see the less pronounced slope in the decreasing region of trace anomaly, after Fig. 5.3 maximal point.

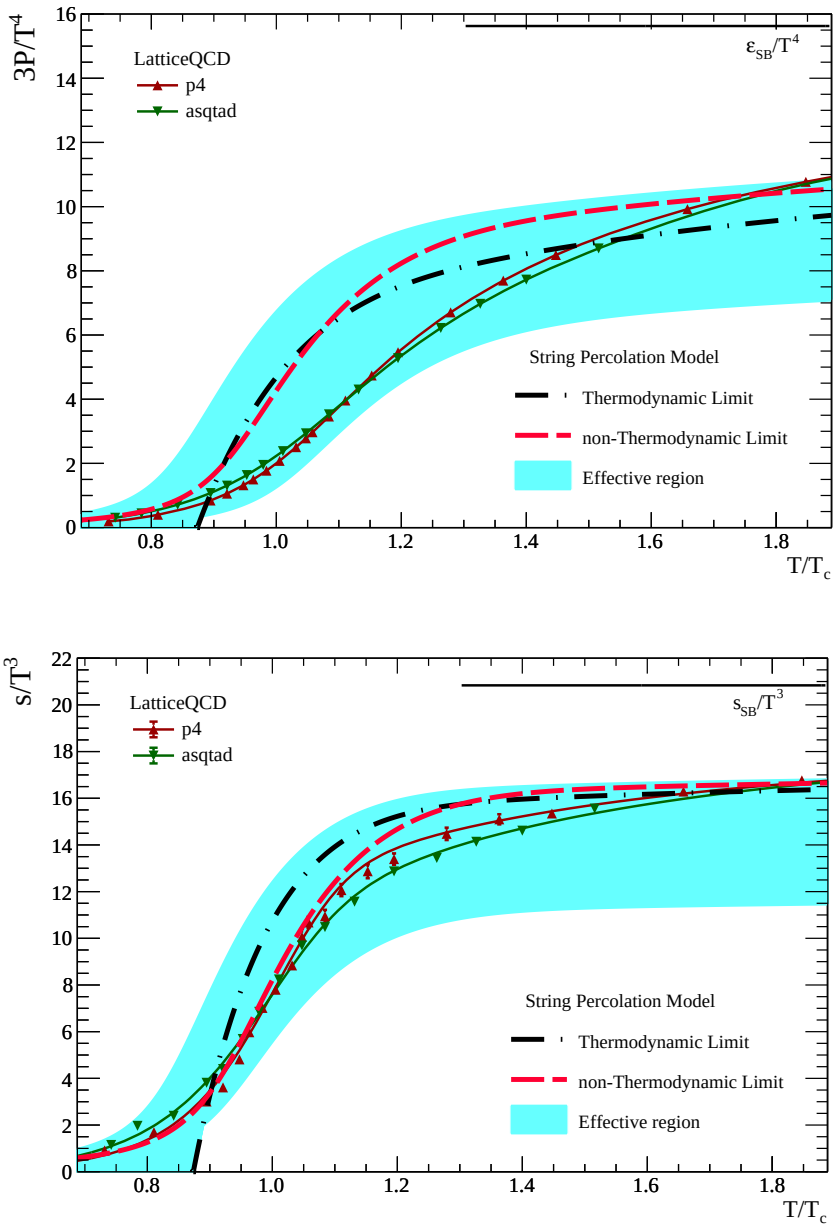

Figure 5.4: Behavior of the pressure over T^4 (upper figure) and entropy density over T^3 (lower figure) against T/T_c, for TL (black dotted-dashed lines) and nonTL (red dashed lines) cases, we show the effective estimate region in the blue area [201]. In both figures, the comparison with Lattice QCD results p4 (maroon triangles) and asqtad (green triangles) actions with their respective parametrization (continuum lines) [202] are included.

5.4 Bulk properties

The effects of bulk viscosity are known to be very small, which in most of the high energy collisions were neglected due to the thermalization of the system. However, great attempts have been made to obtain their value from nuclear collisions from RHIC to LHC [216, 217].

Bulk viscosity corresponds to the resistance to the expansion of the fluid. The radial components seem damped due to the non-zero effect of bulk viscous pressure affecting the energy density profile of the created medium and converting it into pressure gradients changing the speed of sound c_s^2 [200]. This effect is related to the small perturbations produced in the medium formed [200], such as vibrations and rotations of the medium components. In the SPM framework, these effects correspond to the fluctuations of strings (color field, string tension, etc).

5.4.1 Speed of sound

To determine the bulk viscosity we calculate the speed of sound, which is given by a thermodynamic relation [36]:

$$c_s^2 = \left(\frac{\partial P}{\partial \varepsilon}\right)_s = s\left(\frac{\partial T}{\partial \varepsilon}\right)_s = -\frac{sT}{2\varsigma F}\cdot\frac{dF}{d\xi}. \tag{5.11}$$

From Eqs. (3.22) and (3.24) it is simple to obtain $dF/d\xi$ of Eq. (5.11), In Fig. 5.5 we compute the effective region of c_s^2. $F_s(\xi)$ gives a different behavior from what was previously reported in [141, 146, 147, 200], and we also include the results of c_s^2 reported for elliptical geometry [173].

Specifically, we observed a large deviation from TL in the region below the critical temperature, showing a "dip-and-bump" effect, this behavior is in agreement with other phenomenological models [218], and goes accordingly with those reported from the Lattice QCD 2+1 flavor staggered fermion actions p4 and asqtad from [202], the stout-link improved staggered fermion action from Wuppertal-Budapest Collaboration [210] and the highly improved staggered quark action from HotQCD Collaboration [209].

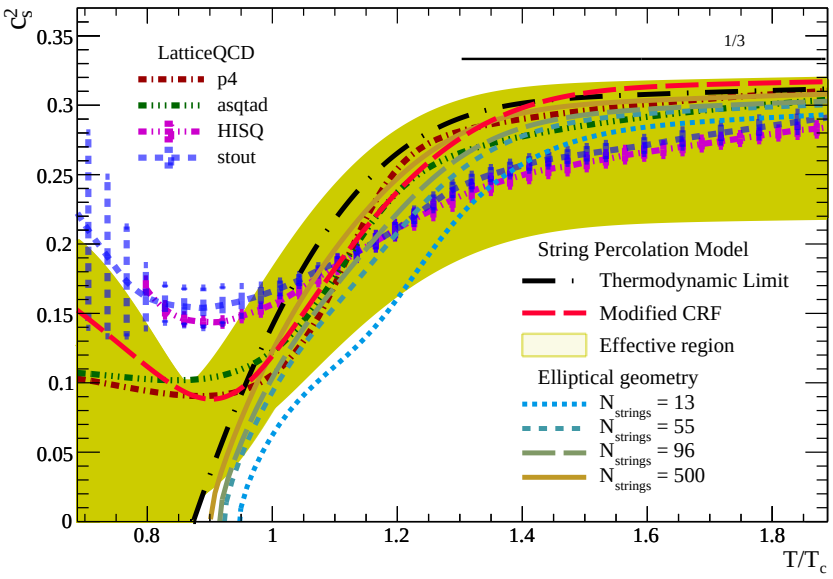

Figure 5.5: Dependence of speed of sound squared with T/T_c calculated in the SPM framework using Eq. (5.11), the effective estimate region (golden area), the nonTL (red dashed line) and TL (black dotted-dashed line) limits are shown [201]. The set of lines (from dotted blue to continuum brown) corresponds to an elliptical initial geometry of a percolating system for different numbers of strings as reported in [173]. The blue squares correspond to the predictions of Lattice QCD 3L-Symanzik/2S stout-link staggered fermions extrapolated results from the Wuppertal-Budapest Collaboration (W-B) [210], the magenta circles are the HIQS action extrapolated results from the HotQCD Collaboration [209]. Meanwhile, the maroon and green triangles correspond to p4 and asqtad staggered fermion actions respectively, with their respective parametrization in continuum lines [202].

5.4.2 Bulk viscosity

The first approximation of bulk viscosity over entropy density ζ/s is given by the simplest kinetic model [219]:

$$\frac{\zeta}{s} = 15\frac{\eta}{s}\left(\frac{1}{3} - c_s^2\right)^2, \tag{5.12}$$

which describes the bulk viscosity coefficient in terms of shear viscosity and speed of sound calculated in the SPM framework. The result of this approach using $F(\xi)$ and $F_s(\xi)$ is shown in dashed lines of Fig. 5.6.

As a second approach, we use the results reported and verified in [220–225] of the projection operator approach to obtain the microscopic formulas for the transport coefficients in causal dissipative relativistic fluid dynamics (CDRF), in terms of the SPM observables T, s, Δ, c_s. The reported microscopic formula of the bulk viscosity ζ with its respective relaxation time τ_Π of CDRF is given by [220–226]:

$$\frac{\zeta}{s} = \left(\frac{1}{3} - c_s^2\right)\tau_\Pi T - \frac{2\tau_\Pi T^4}{9s}\Delta, \tag{5.13}$$

where τ_Π is considered of the order of a fermi and the fraction $2/9$ has to do with the number of fermionic degrees of freedom.

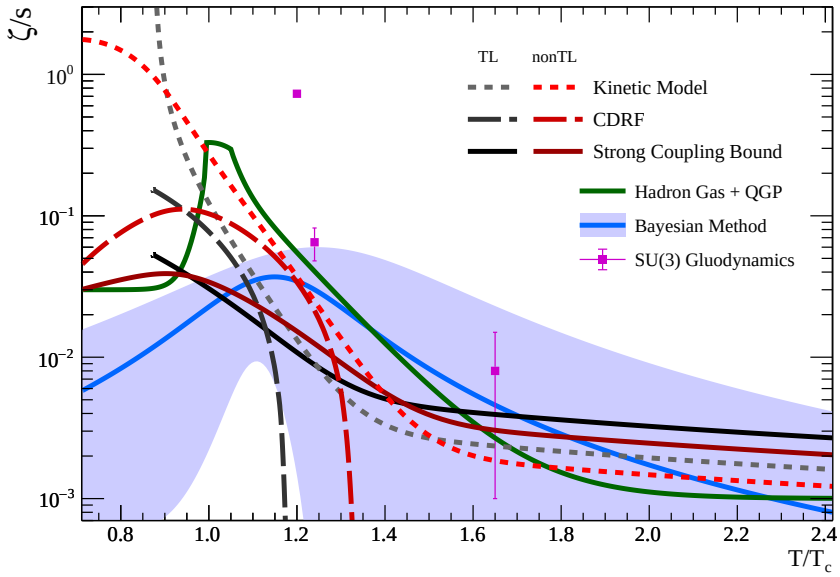

Figure 5.6: Bulk viscosity over entropy density as a function of T/T_C calculated from the kinetic model Eq. (5.12) (dotted lines), the CDRF formalism Eq. (5.13) (dashed lines), and the lower limit of the bulk viscosity over entropy density of gauge theory plasma at strong coupling using Eq. (5.14) (continuum lines) on the SPM framework. Distinguish TL in gray scale lines and nonTL in red lines [201]. Results of ζ/s reported from viscous relativistic hydrodynamics Bayesian Method [205] are included (violet region). The parametrization of Hadron Gas [227] to QGP [228] presented in [229, 230] is shown in the continuum green line. The magenta squares correspond to the Lattice calculation in SU(3) gauge theory [231].

The results of Eq. (5.13) in TL (blue dotted line) and nonTL (red dotted line) are shown in Fig. 5.6 labeled as CDRF.

On the other hand, in [232] is conjectured a lower limit on bulk viscosity of strongly coupled gauge theory plasmas as:

$$\frac{\zeta}{s} \geq 2\left(\frac{1}{3} - c_s^2\right)\frac{\eta}{s} \geq \frac{1}{2\pi}\left(\frac{1}{3} - c_s^2\right), \tag{5.14}$$

considering $\eta/s \geq 1/(4\pi)$ [66]. Which is shown in Fig. 5.6 in solid red for TL and blue lines for nonTL.

	TL		nonTL	
	ζ/s (Max)	T/T_c	ζ/s (Max)	T/T_c
Kinetic	35132.6	0.873553	1.84112	0.146509
CDRF	0.152694	0.873553	0.111427	0.940129
Bound	0.0530515	0.873553	0.0390168	0.903653

Table 5.1: Results of the maximum value of bulk viscosity over entropy density for different approaches in TL and in our parametrization (nonTL).

In Table 5.1, we present the maximum values of ζ/s for the kinetic theory, CDRF formalism, and conjectured bound with its respective T/T_c value for TL and nonTL. We can observe that in all cases ζ/s reaches its maximum value below the critical temperature. And the TL goes much higher than nonTL, reaching its maximum value. For the CDRF formalism, it is reached just 73.54% of the TL. For the lower conjectured bound it is 72.97% and for the case of the simplest kinetic model, we see a discrepancy in the values around 0.0052%, because the value of c_s^2 for TL vanishes at $T/T_c = 0.873553$, Eq. (5.12) gives the same tendency as shear viscosity over entropy density in TL.

In Fig. 5.7 we show the interplay between shear and bulk viscosity, given by the ratio ζ/η computed in the SPM framework, where we can observe a maximum value around the critical temperature region in all cases. For the case of the Kinetic Model, the ζ/η ratio shows its maximum value in $T < T_c$ for TL and nonTL scenarios, and for the CDRF formalism we can see a change in the slope in the region just below $T = T_c$ for TL case, and for nonTL right before $T = T_c$.

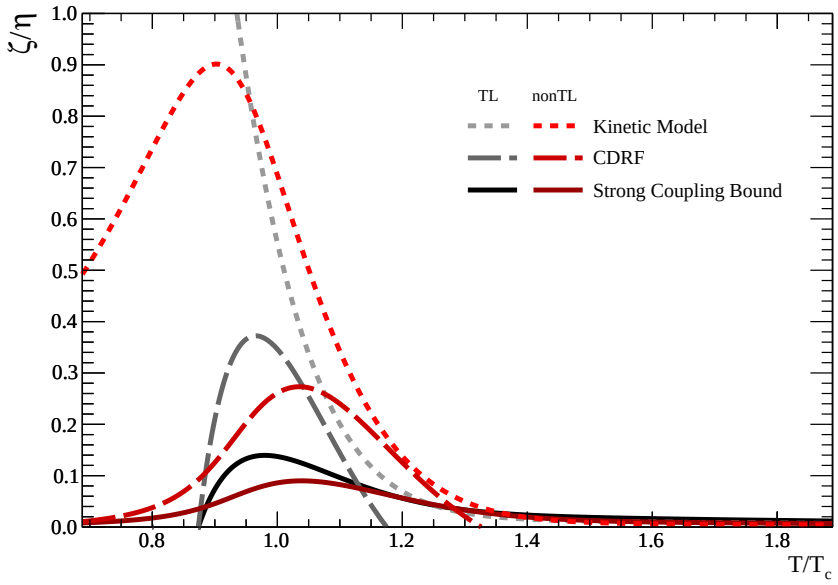

Figure 5.7: The results of the bulk-shear viscosity ratio against T/T_c from the kinetic theory (dotted lines), CDRF (dashed lines), and the gauge theory plasma at strong coupling limit (continuum lines) [232] calculated in the SPM framework. Distinguish TL in gray lines and nonTL in red lines [201].

Conclusions

In this work, recent results were compiled, using Monte Carlo simulation techniques, for the study of the initial state in systems that are created in collisions of ions at relativistic energies. From small systems like proton-proton to heavy ions like PbPb.

In this study, the aim was to investigate the properties of the medium formed in heavy-ion collisions within the framework of the CGC by analyzing the radial distribution function of the gluon configuration in the transverse plane.

To capture the essential features of the CGC, a stochastic CGC framework was employed, taking into account fluctuations in the saturation scale Q_s^2 and their consequences on the running coupling, as well as various characteristics of the CGC, including gluon density, gluon size, and minimum distances between neighboring gluons. The analysis focused on AuAu central collisions at RHIC energies (130 and 200 GeV) and PbPb central collisions at LHC energies (2760 and 5020 GeV).

The results revealed that the gluon distribution in AuAu collisions exhibited characteristics reminiscent of an interacting gas, suggesting a gas-like behavior. On the other hand, for PbPb collisions at LHC energies, evidence pointed towards a liquid-like structure in the system. It is important to note that although the simulations assumed a homogeneous and isotropic representation of the system at the center of the transverse plane, there is a possibility of dilution at the system's edges. This dilution effect could lead to a radial distribution function resembling that of a diluted interacting gas or even an ideal gas, resulting in a relatively flat function.

By employing the analysis of the radial distribution function within the CGC framework, valuable insights were gained regarding the structure and properties of the medium formed in heavy-ion collisions, shedding light on the transition from a gas-like to a liquid-like behavior as the collision energy increased.

On the other hand, by introducing a parametrization for a universal color reduction function in the color string percolation model, denoted as $F(\xi) \rightarrow F_s(\xi)$, the phase transition in the CSPM is considered beyond the thermodynamic limit, accounting for small system effects. This new description of $F_s(\xi)$ enables the estimation of effective regions in the CSPM, incorporating uncertainties through interpolation methods. This approach provides a more comprehensive understanding of transport coefficients and bulk properties.

The study focuses on investigating properties of small collision systems at LHC energies, considering system size effects. Specifically, the results for the bulk viscosity to entropy density ratio and shear viscosity to entropy density ratio are presented in Fig.5.2 and Fig.5.6.

In Fig. 5.2, the effective region of the shear viscosity to entropy density ratio is computed as a function of T/T_c and compared with relativistic hydrodynamics Bayesian Method [205]. The results indicate different minimum values for the thermodynamic limit (TL) and non-thermodynamic limit (nonTL) within the region $T_c < T < 1.23T_c$, consistent with previous findings [149] that identify the phase transition region. Notably, the phase transition occurs at a higher temperature for nonTL.

Fig. 5.3 displays the results for Δ, where TL and nonTL reach their maximum values at $T > T_c$, in agreement with predictions from Lattice QCD [202, 209, 210]. The maximum value for nonTL is attained at a higher temperature compared to TL.

With this new perspective, the speed of sound does not vanish at low temperatures (Fig.5.5) and makes a significant contribution to the calculation of bulk viscosity, as depicted in Fig.5.6.

Both shear and bulk viscosities exhibit similar orders of magnitude compared to previous studies [205, 217, 233–237] and display similar behaviors in the vicinity of the critical temperature region, as shown in Fig.5.6 and Fig.5.2.

Two formalisms were employed to calculate the bulk viscosity to entropy density ratio (ζ/s) and compare it to the strong coupling bound. In the color reduction function (CDRF) formalism, the bulk viscosity vanishes at $T/T_c = 1.17$ for TL and at $T/T_c = 1.32$ for nonTL, as depicted in Fig. 5.6. In the kinetic model, ζ/s reaches higher values below the critical temperature, as summarized in Table 5.1. Both formalisms exceed the strong coupling bound for $T/T_c < 1.1$, where the maximum values are reached. This indicates that in this temperature region, the contribution

of ζ becomes relevant, implying a strong influence of vibrational and rotational effects in the phase transition, driven by string fluctuations (e.g., color field, string tension).

Furthermore, the ratio of bulk viscosity to shear viscosity for TL and nonTL scenarios exhibits a shift in the location of the maximum point, with the maximum value reached at a higher temperature for nonTL. This suggests that nonTL requires a higher temperature to undergo the phase transition due to fluctuations arising from bulk contributions.

The aforementioned description provides a consistent scenario for a possible phase transition in a non-equilibrium medium in small collision systems.

Bibliography

[1] M. Herrero, The Standard Model, Vol. 534, Springer Netherlands, 1999, Ch. 1, pp. 1–59. arXiv:hep-ph/9812242, doi:10.1007/978-94-011-4689-0_1.

[2] D. H. Perkins, Introduction to High Energy Physics, 4th Edition, Cambridge University Press, 2000. doi:10.1017/CBO9780511809040.

[3] T. Nakano, K. Nishijima, Charge Independence for V-particles, Prog. Theor. Phys. 10 (5) (1953) 581–582, academic.oup:article-pdf/10/5/581/5364926/10-5-581. doi:10.1143/PTP.10.581.

[4] K. Nishijima, Charge Independence Theory of V Particles, Prog. Theor. Phys. 13 (3) (1955) 285–304, academic.oup:article-pdf/13/3/285/5425869/13-3-285. doi:10.1143/PTP.13.285.

[5] M. Gell-Mann, The interpretation of the new particles as displaced charge multiplets, Nuovo Cim. 4 (S2) (1956) 848–866. doi:10.1007/BF02748000.

[6] M. Gell-Mann, The Eightfold Way: A Theory of strong interaction symmetry, Tech. rep., California Institute of Technology, Holi (1961). doi:10.2172/4008239.

[7] M. Gell-Mann, A schematic model of baryons and mesons, Phys. Lett. 8 (3) (1964) 214–215, sciencedirect:S0031916364920013. doi:10.1016/S0031-9163(64)92001-3.

[8] G. Zweig, An SU_3 model for strong interaction symmetry and its breaking; Version 2, Tech. rep., CERN, Version 1 (1964). doi:10.17181/CERN-TH-412.

[9] A. Petermann, Propriétés de l'étrangeté et une formule de masse pour les mésons vectoriels, Nucl. Phys. 63 (2) (1965) 349–352, sciencedirect:0029558265903482. doi:10.1016/0029-5582(65)90348-2.

[10] O. W. Greenberg, Spin and Unitary Spin Independence in a Paraquark Model of Baryons and Mesons, Phys. Rev. Lett. 13 (20) (1964) 598–602. doi:10.1103/PhysRevLett.13.598.

[11] W. A. Bardeen, H. Fritzsch, M. Gell-Mann, Light-Cone current Algebra, π^0 Decay and e^+e^- Annihilation, Tech. rep., CERN, Geneva, cds.cern.ch/record/593283 (1972). arXiv:hep-ph/0211388.

[12] H. Fritzsch, M. Gell-Mann, H. Leutwyler, Advantages of the color octet gluon picture, Phys. Lett. B 47 (4) (1973) 365–368, sciencedirect:0370269373906254. doi:10.1016/0370-2693(73)90625-4.

[13] Particle Data Group, Review of Particle Physics, PTEP 2022 (2022) 083C01, academic.oup:article-pdf/2022/8/083C01/49175539/ptac097. doi:10.1093/ptep/ptac097.

[14] M. Eidemuller, H. G. Dosch, M. Jamin, The field strength correlator from QCD sum rules, Nucl. Phys. B Proc. Suppl. 86 (1) (2000) 421–425. arXiv:hep-ph/9908318, doi:10.1016/S0920-5632(00)00598-3.

[15] D. J. Gross, F. Wilczek, Ultraviolet Behavior of Non-Abelian Gauge Theories, Phys. Rev. Lett. 30 (26) (1973) 1343–1346. doi:10.1103/PhysRevLett.30.1343.

[16] H. D. Politzer, Reliable Perturbative Results for Strong Interactions?, Phys. Rev. Lett. 30 (26) (1973) 1346–1349. doi:10.1103/PhysRevLett.30.1346.

[17] CMS Collaboration, Measurement of the inclusive 3-jet production differential cross section in proton–proton collisions at 7 TeV and determination of the strong coupling constant in the TeV range, Eur. Phys. J. C 75 (5) (2015) 186. arXiv:1412.1633, doi:10.1140/epjc/s10052-015-3376-y.

[18] J. S. Schwinger, On Gauge Invariance and Vacuum Polarization, Phys. Rev. 82 (5) (1951) 664–679. doi:10.1103/PhysRev.82.664.

[19] P. Pascual, R. Tarrach, QCD: Renormalization for the Practitioner, Vol. 194, Springer-Verlag, 1984. doi:10.1007/3-540-12908-1.

[20] P. A. Kovalenko, L. V. Laperashvili, The Effective QCD Lagrangian and Renormalization Group Approach, Phys. Atom. Nucl. 62 (10) (1999) 1729–1738. arXiv:hep-ph/9711390.

[21] F. Herzog, B. Ruijl, T. Ueda, J. A. M. Vermaseren, A. Vogt, The five-loop beta function of Yang-Mills theory with fermions, J. High Energ. Phys. 2017 (2) (2017) 90. arXiv:1701.01404, doi:10.1007/JHEP02(2017)090.

[22] G. 't Hooft, When was asymptotic freedom discovered? or The rehabilitation of quantum field theory, Nucl. Phys. B Proc. Suppl. 74 (1) (1999) 413–425. arXiv:hep-th/9808154, doi:10.1016/S0920-5632(99)00207-8.

[23] S. Durr, Z. Fodor, C. Hoelbling, S. D. Katz, S. Krieg, T. Kurth, L. Lellouch, T. Lippert, K. K. Szabo, G. Vulvert, Lattice QCD at the physical point: Light quark masses, Phys. Lett. B 701 (2) (2011) 265–268. arXiv:1011.2403, doi:10.1016/j.physletb.2011.05.053.

[24] A. Dobado, A. Gómez-Nicola, A. L. Maroto, J. R. Peláez, Effective Lagrangians for the Standard Model, Springer-Verlag, 1997. doi:10.1007/978-3-642-59191-4.

[25] J. Goldstone, Field theories with ≪ Superconductor ≫ solutions, Nuovo Cim. 19 (1) (1961) 154–164. doi:10.1007/BF02812722.

[26] T. Lee, Vacuum energy and trace anomaly (2018). arXiv:1810.08910.

[27] J. C. Collins, A. Duncan, S. D. Joglekar, Trace and dilatation anomalies in gauge theories, Phys. Rev. D 16 (2) (1977) 438–449. doi:10.1103/PhysRevD.16.438.

[28] R. S. Chivukula, The Origin of Mass in QCD, eConf C040802 (2004) L010. arXiv:hep-ph/0411198.

[29] Y. Taniguchi, S. Ejiri, R. Iwami, K. Kanaya, M. Kitazawa, H. Suzuki, T. Umeda, N. Wakabayashi, Exploring N_f = 2+1 QCD thermodynamics from the gradient flow, Phys. Rev. D 96 (1) (2017) 014509. arXiv:1609.01417, doi:10.1103/PhysRevD.96.014509.

[30] T. D. Lee, G. C. Wick, Vacuum stability and vacuum excitation in a spin-0 field theory, Phys. Rev. D 9 (8) (1974) 2291–2316. doi:10.1103/PhysRevD.9.2291.

[31] J. C. Collins, M. J. Perry, Superdense Matter: Neutrons Or Asymptotically Free Quarks?, Phys. Rev. Lett. 34 (21) (1975) 1353–1356. doi:10.1103/PhysRevLett.34.1353.

[32] W. Scheid, H. Muller, W. Greiner, Nuclear Shock Waves in Heavy-Ion Collisions, Phys. Rev. Lett. 32 (13) (1974) 741–745. doi:10.1103/PhysRevLett.32.741.

[33] B. A. Freedman, L. D. McLerran, Fermions and gauge vector mesons at finite temperature and density. I. Formal techniques, Phys. Rev. D 16 (4) (1977) 1130–1146. doi:10.1103/PhysRevD.16.1130.

[34] E. V. Shuryak, Quark-gluon plasma and hadronic production of leptons, photons and psions, Phys. Lett. B 78 (1) (1978) 150–153, sciencedirect:0370269378903702. doi:10.1016/0370-2693(78)90370-2.

[35] L. D. McLerran, B. Svetitsky, Quark liberation at high temperature: A Monte Carlo study of SU(2) gauge theory, Phys. Rev. D 24 (1981) 450. doi:10.1103/PhysRevD.24.450.

[36] J. D. Bjorken, Highly relativistic nucleus-nucleus collisions: The central rapidity region, Phys. Rev. D 27 (1) (1983) 140–151. doi:10.1103/PhysRevD.27.140.

[37] F. Karsch, Recent lattice results on finite temperature and density QCD. Part I., PoS CPOD07 (2007) 026. arXiv:0711.0656, doi:10.22323/1.047.0026.

[38] F. Karsch, Recent lattice results on finite temperature and density QCD. Part II., PoS LATTICE2007 (2007) 015. arXiv:0711.0661, doi:10.22323/1.042.0015.

[39] F. Karsch, Lattice QCD at High Temperature and Density, Vol. 583, Springer Berlin Heidelberg, 2002, Ch. 6, pp. 209–249. arXiv:hep-lat/0106019, doi:10.1007/3-540-45792-5_6.

[40] Wuppertal-Budapest Collaboration, Is there still any T_c mystery in lattice QCD? Results with physical masses in the continuum limit III, J. High Energ. Phys. 2010 (9) (2010) 73. arXiv:1005.3508, doi:10.1007/JHEP09(2010)073.

[41] HotQCD Collaboration, The chiral and deconfinement aspects of the QCD transition, Phys. Rev. D 85 (5) (2012) 054503. arXiv:1111.1710, doi:10.1103/PhysRevD.85.054503.

[42] P. Petreczky, Lattice QCD at non-zero temperature, J. Phys. G 39 (9) (2012) 093002. arXiv:1203.5320, doi:10.1088/0954-3899/39/9/093002.

[43] C. P. Singh, Signals of quark-gluon plasma, Phys. Rept. 236 (3) (1993) 147–224, sciencedirect:037015739390172A. doi:10.1016/0370-1573(93)90172-A.

[44] T. Boeckel, J. Schaffner-Bielich, Little inflation at the cosmological QCD phase transition, Phys. Rev. D 85 (10) (2012) 103506. arXiv:1105.0832, doi:10.1103/PhysRevD.85.103506.

[45] ALICE Collaboration, Centrality dependence of the charged-particle multiplicity density at mid-rapidity in Pb-Pb collisions at $\sqrt{s_{NN}} = 2.76$ TeV, Phys. Rev. Lett. 106 (2011) 032301. arXiv:1012.1657, doi:10.1103/PhysRevLett.106.032301.

[46] ALICE Collaboration, Centrality Dependence of the Charged-Particle Multiplicity Density at Midrapidity in Pb-Pb Collisions at $\sqrt{s_{\mathrm{NN}}}$ = 5.02 TeV, Phys. Rev. Lett. 116 (22) (2016) 222302. arXiv:1512.06104, doi:10.1103/PhysRevLett.116.222302.

[47] ALICE Collaboration, Charged-particle multiplicities in proton–proton collisions at $\sqrt{s} = 0.9$ to 8 TeV, Eur. Phys. J. C 77 (1) (2017) 33. arXiv:1509.07541, doi:10.1140/epjc/s10052-016-4571-1.

[48] ALICE Collaboration, Pseudorapidity density of charged particles in p + Pb collisions at $\sqrt{s_{NN}} = 5.02$ TeV, Phys. Rev. Lett. 110 (3) (2013) 032301. arXiv:1210.3615, doi:10.1103/PhysRevLett.110.032301.

[49] ALICE Collaboration, Measurement of transverse energy at midrapidity in Pb-Pb collisions at $\sqrt{s_{\mathrm{NN}}} = 2.76$ TeV, Phys. Rev. C 94 (3) (2016) 034903. arXiv:1603.04775, doi:10.1103/PhysRevC.94.034903.

[50] STAR Collaboration, Measurements of transverse energy distributions in Au + Au collisions at $\sqrt{s_{NN}} = 200$ GeV, Phys. Rev. C 70 (2004) 054907. arXiv:nucl-ex/0407003, doi:10.1103/PhysRevC.70.054907.

[51] PHENIX Collaboration, Measurement of the midrapidity transverse energy distribution from $\sqrt{s_{\rm NN}} = 130$GeV $au + au$ collisions at rhic, Phys. Rev. Lett. 87 (2001) 052301. arXiv:nucl-ex/0104015, doi:10.1103/PhysRevLett.87.052301.

[52] S. S. Adler, et al., Systematic studies of the centrality and $\sqrt{s_{NN}}$ dependence of the $de_T/d\eta$ and $dn_{\rm ch}/d\eta$ in heavy ion collisions at midrapidity, Phys. Rev. C 71 (2005) 034908, [Erratum: Phys.Rev.C 71, 049901 (2005)]. arXiv:nucl-ex/0409015, doi:10.1103/PhysRevC.71.034908.

[53] PHENIX Collaboration, Formation of dense partonic matter in relativistic nucleus-nucleus collisions at RHIC: Experimental evaluation by the PHENIX collaboration, Nucl. Phys. A 757 (2005) 184–283. arXiv:nucl-ex/0410003, doi:10.1016/j.nuclphysa.2005.03.086.

[54] PHOBOS Collaboration, The PHOBOS perspective on discoveries at RHIC, Nucl. Phys. A 757 (1) (2005) 28–101. arXiv:nucl-ex/0410022, doi:10.1016/j.nuclphysa.2005.03.084.

[55] BRAHMS Collaboration, Quark gluon plasma and color glass condensate at RHIC? The perspective from the BRAHMS experiment, Nucl. Phys. A 757 (1) (2005) 1–27. arXiv:nucl-ex/0410020, doi:10.1016/j.nuclphysa.2005.02.130.

[56] STAR Collaboration, Experimental and theoretical challenges in the search for the quark gluon plasma: The STAR Collaboration's critical assessment of the evidence from RHIC collisions, Nucl. Phys. A 757 (1) (2005) 102–183. arXiv:nucl-ex/0501009, doi:10.1016/j.nuclphysa.2005.03.085.

[57] M. Gyulassy, L. McLerran, New forms of QCD matter discovered at RHIC, Nucl. Phys. A 750 (1) (2005) 30–63. arXiv:nucl-th/0405013, doi:10.1016/j.nuclphysa.2004.10.034.

[58] F. Becattini, A Thermodynamical approach to hadron production in e^+e^- collisions, Z. Phys. C 69 (3) (1995) 485–492. doi:10.1007/BF02907431.

[59] F. Becattini, Hadrosynthesis at SPS and RHIC and the statistical model, J. Phys. G 28 (7) (2002) 1553–1560. arXiv:hep-ph/0202071, doi:10.1088/0954-3899/28/7/305.

[60] J. Cleymans, B. Kampfer, M. Kaneta, S. Wheaton, N. Xu, Centrality dependence of thermal parameters deduced from hadron multiplicities in Au + Au collisions at $\sqrt{s_{\mathrm{NN}}} = 130$GeV, Phys. Rev. C 71 (5) (2005) 054901. arXiv:hep-ph/0409071, doi:10.1103/PhysRevC.71.054901.

[61] G.-Y. Qin, Anisotropic flow and jet quenching in relativistic nuclear collisions, Int. J. Mod. Phys. E 24 (02) (2015) 1530001. arXiv:1502.02554, doi:10.1142/S0218301315300015.

[62] J.-Y. Ollitrault, Anisotropy as a signature of transverse collective flow, Phys. Rev. D 46 (1) (1992) 229–245. doi:10.1103/PhysRevD.46.229.

[63] T. Hirano, Y. Nara, Pseudorapidity dependence of parton energy loss in relativistic heavy ion collisions, Phys. Rev. C 68 (6) (2003) 064902. arXiv:nucl-th/0307087, doi:10.1103/PhysRevC.68.064902.

[64] D. Molnar, S. A. Voloshin, Elliptic Flow at Large Transverse Momenta from Quark Coalescence, Phys. Rev. Lett. 91 (9) (2003) 092301. arXiv:nucl-th/0302014, doi:10.1103/PhysRevLett.91.092301.

[65] NA49 Collaboration, Directed and elliptic flow of charged pions and protons in Pb + Pb collisions at 40A and 158AGeV, Phys. Rev. C 68 (3) (2003) 034903. arXiv:nucl-ex/0303001, doi:10.1103/PhysRevC.68.034903.

[66] G. Policastro, D. T. Son, A. O. Starinets, Shear Viscosity of Strongly Coupled $N = 4$ Supersymmetric Yang-Mills Plasma, Phys. Rev. Lett. 87 (8) (2001) 081601. arXiv:hep-th/0104066, doi:10.1103/PhysRevLett.87.081601.

[67] J. D. Bjorken, Energy loss of energetic partons in quark-gluon plasma: possible extinction of high p_T jets in hadron-hadron collisions, Tech. rep., FERMILAB, https://cds.cern.ch/record/141477 (1982).

[68] N. Armesto, Nuclear shadowing, J. Phys. G 32 (11) (2006) R367–R394. arXiv:hep-ph/0604108, doi:10.1088/0954-3899/32/11/R01.

[69] PHENIX Collaboration, High transverse momentum η meson production in $p+p$, d+Au, and Au+Au collisions at $\sqrt{s_{NN}} = 200$ GeV, Phys. Rev. C 75 (2) (2007) 024909. arXiv:nucl-ex/0611006, doi:10.1103/PhysRevC.75.024909.

[70] R. Baier, D. Schiff, B. G. Zakharov, Energy Loss in Perturbative QCD, Ann. Rev. Nucl. Part. Sci. 50 (1) (2000) 37–69. arXiv:hep-ph/0002198, doi:10.1146/annurev.nucl.50.1.37.

[71] M. Gyulassy, I. Vitev, X.-N. Wang, B.-W. Zhang, JET QUENCHING AND RADIATIVE ENERGY LOSS IN DENSE NUCLEAR MATTER, World Scientific Publishing Co Pte Ltd, 2003, Ch. 3, pp. 123–191. arXiv:nucl-th/0302077, doi:10.1142/9789812795533_0003.

[72] A. Kovner, U. A. Wiedemann, GLUON RADIATION AND PARTON ENERGY LOSS, World Scientific Publishing Co Pte Ltd, 2003, Ch. 4, pp. 192–248. arXiv:hep-ph/0304151, doi:10.1142/9789812795533_0004.

[73] ALICE Collaboration, Elliptic Flow of Charged Particles in Pb-Pb Collisions at $\sqrt{s_{NN}} = 2.76$ TeV, Phys. Rev. Lett. 105 (25) (2010) 252302. arXiv:1011.3914, doi:10.1103/PhysRevLett.105.252302.

[74] CMS Collaboration, Measurement of the elliptic anisotropy of charged particles produced in PbPb collisions at $\sqrt{s_{NN}}$=2.76 TeV, Phys. Rev. C 87 (1) (2013) 014902. arXiv:1204.1409, doi:10.1103/PhysRevC.87.014902.

[75] ATLAS Collaboration, Measurement of the pseudorapidity and transverse momentum dependence of the elliptic flow of charged particles in lead-lead collisions at $\sqrt{s_{NN}} = 2.76$ TeV with the ATLAS detector, Phys. Lett. B 707 (3) (2012) 330–348. arXiv:1108.6018, doi:10.1016/j.physletb.2011.12.056.

[76] ALICE Collaboration, Higher Harmonic Anisotropic Flow Measurements of Charged Particles in Pb-Pb Collisions at $\sqrt{s_{NN}} = 2.76$ TeV, Phys. Rev. Lett. 107 (3) (2011) 032301. arXiv:1105.3865, doi:10.1103/PhysRevLett.107.032301.

[77] CMS Collaboration, Studies of azimuthal dihadron correlations in ultra-central PbPb collisions at $\sqrt{s_{NN}} = 2.76$ TeV, J. High Energ. Phys. 2014 (02) (2014) 88. arXiv:1312.1845, doi:10.1007/JHEP02(2014)088.

[78] ALICE Collaboration, Long-range angular correlations on the near and away side in p-Pb collisions at $\sqrt{s_{NN}} = 5.02$ TeV, Phys. Lett. B 719 (1) (2013) 29–41. arXiv:1212.2001, doi:10.1016/j.physletb.2013.01.012.

[79] CMS Collaboration, Observation of long-range, near-side angular correlations in proton-proton collisions at the LHC, J. High Energ. Phys. 2010 (9) (2010) 91. arXiv:1009.4122, doi:10.1007/JHEP09(2010)091.

[80] CMS Collaboration, Observation of long-range, near-side angular correlations in pPb collisions at the LHC, Phys. Lett. B 718 (3) (2013) 795–814. arXiv:1210.5482, doi:10.1016/j.physletb.2012.11.025.

[81] CMS Collaboration, Multiplicity and transverse momentum dependence of two- and four-particle correlations in pPb and PbPb collisions, Phys. Lett. B 724 (4) (2013) 213–240. arXiv:1305.0609, doi:10.1016/j.physletb.2013.06.028.

[82] L. D. McLerran, R. Venugopalan, Computing quark and gluon distribution functions for very large nuclei, Phys. Rev. D 49 (5) (1994) 2233–2241. arXiv:hep-ph/9309289, doi:10.1103/PhysRevD.49.2233.

[83] A. L. Ayala, M. B. Gay Ducati, E. M. Levin, QCD evolution of the gluon density in a nucleus, Nucl. Phys. B 493 (1) (1997) 305–353. arXiv:hep-ph/9604383, doi:10.1016/S0550-3213(97)00002-3.

[84] D. Kharzeev, M. Nardi, Hadron production in nuclear collisions at RHIC and high-density QCD, Phys. Lett. B 507 (2001) 121–128. arXiv:nucl-th/0012025, doi:10.1016/S0370-2693(01)00457-9.

[85] A. M. Staśto, K. Golec-Biernat, J. Kwieciński, Geometric Scaling for the Total $\gamma^* p$ Cross Section in the Low x Region, Phys. Rev. Lett. 86 (4) (2001) 596–599. arXiv:hep-ph/0007192, doi:10.1103/PhysRevLett.86.596.

[86] N. Armesto, C. A. Salgado, U. A. Wiedemann, Relating High-Energy Lepton-Hadron, Proton-Nucleus, and Nucleus-Nucleus Collisions through Geometric Scaling, Phys. Rev. Lett. 94 (2) (2005) 022002. arXiv:hep-ph/0407018, doi:10.1103/PhysRevLett.94.022002.

[87] T. Lappi, L. McLerran, Some features of the glasma, Nucl. Phys. A 772 (3) (2006) 200–212. arXiv:hep-ph/0602189, doi:10.1016/j.nuclphysa.2006.04.001.

[88] J. L. Albacete, C. Marquet, Gluon saturation and initial conditions for relativistic heavy ion collisions, Prog. Part. Nucl. Phys. 76 (2014) 1–42, sciencedirect:S0146641014000052. doi:10.1016/j.ppnp.2014.01.004.

[89] L. V. Gribov, E. M. Levin, M. G. Ryskin, Semihard Processes in QCD, Phys. Rept. 100 (1) (1983) 1–150, sciencedirect:0370157383900224. doi:10.1016/0370-1573(83)90022-4.

[90] A. H. Mueller, Small-x behavior and parton saturation: A QCD model, Nucl. Phys. B 335 (1) (1990) 115–137, sciencedirect:055032139090173B. doi:10.1016/0550-3213(90)90173-B.

[91] J. P. Blaizot, A. H. Mueller, The early stage of ultra-relativistic heavy ion collisions, Nucl. Phys. B 289 (1987) 847–860, sciencedirect:0550321387904081. doi:10.1016/0550-3213(87)90408-1.

[92] L. D. McLerran, R. Venugopalan, Green's functions in the color field of a large nucleus, Phys. Rev. D 50 (3) (1994) 2225–2233. doi:10.1103/PhysRevD.50.2225.

[93] I. Balitsky, Operator expansion for high-energy scattering, Nucl. Phys. B 463 (1) (1996) 99–157, sciencedirect:0550321395006389. doi:10.1016/0550-3213(95)00638-9.

[94] Y. V. Kovchegov, Small-x F_2 structure function of a nucleus including multiple Pomeron exchanges, Phys. Rev. D 60 (3) (1999) 034008. doi:10.1103/PhysRevD.60.034008.

[95] J. Jalilian-Marian, A. Kovner, A. Leonidov, H. Weigert, Wilson renormalization group for low x physics: Towards the high density regime, Phys. Rev. D 59 (1) (1998) 014014. doi:10.1103/PhysRevD.59.014014.

[96] J. Jalilian-Marian, A. Kovner, A. Leonidov, H. Weigert, The BFKL equation from the Wilson renormalization group, Nucl. Phys. B 504 (1) (1997) 415–431, sciencedirect:S0550321397004409. doi:10.1016/S0550-3213(97)00440-9.

[97] E. Iancu, A. Leonidov, L. D. McLerran, The Renormalization group equation for the color glass condensate, Phys. Lett. B 510 (1) (2001) 133–144, sciencedirect:S037026930100524X. doi:10.1016/S0370-2693(01)00524-X.

[98] E. Iancu, A. Leonidov, L. D. McLerran, Nonlinear gluon evolution in the color glass condensate: I, Nucl. Phys. A 692 (3) (2001) 583–645, sciencedirect:S037594740100642X. doi:10.1016/S0375-9474(01)00642-X.

[99] H. Weigert, Unitarity at small Bjorken x, Nucl. Phys. A 703 (3) (2002) 823–860, sciencedirect:S0375947401016682. doi:10.1016/S0375-9474(01)01668-2.

[100] A. Dumitru, D. E. Kharzeev, E. M. Levin, Y. Nara, Gluon saturation in pA collisions at energies available at the CERN Large Hadron Collider: Predictions for hadron multiplicities, Phys. Rev. C 85 (2012) 044920. doi:10.1103/PhysRevC.85.044920.

[101] A. Dumitru, Y. Nara, Scaling of fluctuations in pp and pA collisions, and eccentricities in relativistic heavy-ion collisions, Phys. Rev. C 85 (3) (2012) 034907. doi:10.1103/PhysRevC.85.034907.

[102] B. Schenke, P. Tribedy, R. Venugopalan, Fluctuating Glasma Initial Conditions and Flow in Heavy Ion Collisions, Phys. Rev. Lett. 108 (25) (2012) 252301. doi:10.1103/PhysRevLett.108.252301.

[103] H. Kowalski, D. Teaney, Impact parameter dipole saturation model, Phys. Rev. D 68 (11) (2003) 114005. doi:10.1103/PhysRevD.68.114005.

[104] B. Schenke, P. Tribedy, R. Venugopalan, Event-by-event gluon multiplicity, energy density, and eccentricities in ultrarelativistic heavy-ion collisions, Phys. Rev. C 86 (3) (2012) 034908. doi:10.1103/PhysRevC.86.034908.

[105] L. D. McLerran, R. Venugopalan, Gluon distribution functions for very large nuclei at small transverse momentum, Phys. Rev. D 49 (7) (1994) 3352–3355. doi:10.1103/PhysRevD.49.3352.

[106] F. Gelis, E. Iancu, J. Jalilian-Marian, R. Venugopalan, The Color Glass Condensate, Ann. Rev. Nucl. Part. Sci. 60 (1) (2010) 463–489. doi:10.1146/annurev.nucl.010909.083629.

[107] B. Schenke, P. Tribedy, R. Venugopalan, Multiplicity distributions in $p + p$, $p + A$, and $A + A$ collisions from Yang-Mills dynamics, Phys. Rev. C 89 (2) (2014) 024901. doi:10.1103/PhysRevC.89.024901.

[108] C. Gale, S. Jeon, B. Schenke, P. Tribedy, R. Venugopalan, Event-by-Event Anisotropic Flow in Heavy-ion Collisions from Combined Yang-Mills and Viscous Fluid Dynamics, Phys. Rev. Lett. 110 (1) (2013) 012302. doi:10.1103/PhysRevLett.110.012302.

[109] K. Dusling, R. Venugopalan, Azimuthal Collimation of Long Range Rapidity Correlations by Strong Color Fields in High Multiplicity Hadron-Hadron Collisions, Phys. Rev. Lett. 108 (26) (2012) 262001. doi:10.1103/PhysRevLett.108.262001.

[110] L. McLerran, P. Tribedy, Intrinsic fluctuations of the proton saturation momentum scale in high multiplicity p+p collisions, Nucl. Phys. A 945 (2016) 216–225, sciencedirect:S0375947415002316. doi:10.1016/j.nuclphysa.2015.10.008.

[111] B. Schenke, C. Shen, P. Tribedy, Running the gamut of high energy nuclear collisions, Phys. Rev. C 102 (4) (2020) 044905. doi:10.1103/PhysRevC.102.044905.

[112] Y. V. Kovchegov, Non-Abelian Weizsäcker-Williams field and a two-dimensional effective color charge density for a very large nucleus, Phys. Rev. D 54 (9) (1996) 5463–5469. doi:10.1103/PhysRevD.54.5463.

[113] D. Kharzeev, E. Levin, M. Nardi, Color glass condensate at the LHC: hadron multiplicities in pp, pA and AA collisions, Nucl. Phys. A 747 (2) (2005) 609–629, sciencedirect:S0375947404010991. doi:10.1016/j.nuclphysa.2004.10.018.

[114] A. Capella, U. Sukhatme, C.-I. Tan, J. Tran Thanh Van, Dual parton model, Phys. Rept. 236 (4) (1994) 225–329, sciencedirect:0370157394900647. doi:10.1016/0370-1573(94)90064-7.

[115] A. Capella, U. Sukhatme, C.-I. Tan, J. Tran Thanh Van, Jets in small-p_T hadronic collisions, universality of quark fragmentation, and rising rapidity

plateaus, Phys. Lett. B 81 (1) (1979) 68–74, sciencedirect:0370269379907184. doi:10.1016/0370-2693(79)90718-4.

[116] K. Werner, Strings, pomerons, and the venus model of hadronic interactions at ultrarelativistic energies, Phys. Rept. 232 (2) (1993) 87–299, sciencedirect:037015739390078R. doi:10.1016/0370-1573(93)90078-R.

[117] A. B. Kaidalov, K. A. Ter-Martirosian, Pomeron as quark-gluon strings and multiple hadron production at SPS-Collider energies, Phys. Lett. B 117 (3) (1982) 247–251, sciencedirect:0370269382905561. doi:10.1016/0370-2693(82)90556-1.

[118] K. Werner, T. Hirano, I. Karpenko, T. Pierog, S. Porteboeuf, M. Bleicher, S. Haussler, Gribov-Regge theory, partons, remnants, strings - and the EPOS model for hadronic interactions, Nucl. Phys. B Proc. Suppl. 196 (2009) 36–43, sciencedirect:S0920563209006422. doi:10.1016/j.nuclphysbps.2009.09.006.

[119] F. W. Bopp, J. Ranft, R. Engel, S. Roesler, Learning from RHIC data with DPMJET-III, Acta Phys. Polon. B 35 (1) (2004) 303–307, actaphys.uj.edu.pl/R/35/1/303/pdf.

[120] X.-N. Wang, M. Gyulassy, HIJING: A Monte Carlo model for multiple jet production in pp, pA, and AA collisions, Phys. Rev. D 44 (11) (1991) 3501–3516. doi:10.1103/PhysRevD.44.3501.

[121] T. Sjöstrand, S. Mrenna, P. Z. Skands, A brief introduction to PYTHIA 8.1, Comput. Phys. Commun. 178 (11) (2008) 852–867. arXiv:0710.3820, doi:10.1016/j.cpc.2008.01.036.

[122] Z.-W. Lin, C. M. Ko, B.-A. Li, B. Zhang, S. Pal, Multiphase transport model for relativistic heavy ion collisions, Phys. Rev. C 72 (6) (2005) 064901. arXiv:nucl-th/0411110, doi:10.1103/PhysRevC.72.064901.

[123] M. Bleicher, E. Zabrodin, C. Spieles, S. A. Bass, C. Ernst, S. Soff, L. Bravina, M. Belkacem, H. Weber, H. Stöcker, W. Greiner, Relativistic hadron-hadron collisions in the ultra-relativistic quantum molecular dynamics model, J. Phys.

G 25 (9) (1999) 1859–1896. arXiv:hep-ph/9909407, doi:10.1088/0954-3899/25/9/308.

[124] N. Armesto, M. A. Braun, E. G. Ferreiro, C. Pajares, Percolation Approach to Quark-Gluon Plasma and J/ψ Suppression, Phys. Rev. Lett. 77 (18) (1996) 3736–3738. arXiv:hep-ph/9607239, doi:10.1103/PhysRevLett.77.3736.

[125] M. Nardi, H. Satz, String clustering and J/ψ suppression in nuclear collisions, Phys. Lett. B 442 (1) (1998) 14–19. arXiv:hep-ph/9805247, doi:10.1016/S0370-2693(98)01234-9.

[126] M. A. Braun, C. Pajares, J. Ranft, FUSION OF STRINGS VS. PERCOLATION AND THE TRANSITION TO THE QUARK–GLUON PLASMA, Int. J. Mod. Phys. A 14 (17) (1999) 2689–2704. arXiv:hep-ph/9707363, doi:10.1142/S0217751X99001354.

[127] M. A. Braun, C. Pajares, Implications of color-string percolation on multiplicities, correlations, and the transverse momentum, Eur. Phys. J. C 16 (2) (2000) 349–359. arXiv:hep-ph/9907332, doi:10.1007/s100520050027.

[128] M. A. Braun, C. Pajares, Transverse Momentum Distributions and Their Forward-Backward Correlations in the Percolating Color String Approach, Phys. Rev. Lett. 85 (23) (2000) 4864–4867. arXiv:hep-ph/0007201, doi:10.1103/PhysRevLett.85.4864.

[129] M. B. Isichenko, Percolation, statistical topography, and transport in random media, Rev. Mod. Phys. 64 (4) (1992) 961–1043. doi:10.1103/RevModPhys.64.961.

[130] J. Dias de Deus, C. Pajares, String percolation and the Glasma, Phys. Lett. B 695 (1) (2011) 211–213. arXiv:1011.1099, doi:10.1016/j.physletb.2010.11.017.

[131] B. Andersson, G. Gustafson, B. Nilsson-Almqvist, A model for low-p_T hadronic reactions with generalizations to hadron-nucleus and nucleus-nucleus collisions, Nucl. Phys. B 281 (1) (1987) 289–309, sciencedirect:0550321387902574. doi:10.1016/0550-3213(87)90257-4.

[132] H. Sorge, H. Stoecker, W. Greiner, Relativistic quantum molecular dynamics approach to nuclear collisions at ultrarelativistic energies, Nucl. Phys. A 498 (1989) 567–576, sciencedirect:0375947489906416. doi:10.1016/0375-9474(89)90641-6.

[133] B. Andersson, G. Gustafson, G. Ingelman, T. Sjostrand, Parton fragmentation and string dynamics, Phys. Rept. 97 (2) (1983) 31–145, sciencedirect:0370157383900807. doi:10.1016/0370-1573(83)90080-7.

[134] T. S. Biro, H. B. Nielsen, J. Knoll, Colour rope model for extreme relativistic heavy ion collisions, Nucl. Phys. B 245 (1984) 449–468, sciencedirect:0550321384904413. doi:10.1016/0550-3213(84)90441-3.

[135] M. A. Braun, C. Pajares, Particle production in nuclear collisions and string interactions, Phys. Lett. B 287 (1) (1992) 154–158, sciencedirect:037026939291892D. doi:10.1016/0370-2693(92)91892-D.

[136] N. S. Amelin, M. A. Braun, C. Pajares, Multiple production in the Monte Carlo string fusion model, Phys. Lett. B 306 (3) (1993) 312–318, sciencedirect:037026939390085V. doi:10.1016/0370-2693(93)90085-V.

[137] N. S. Amelin, M. A. Braun, C. Pajares, tring fusion and particle production at high energies: Monte-Carlo string fusion model, Z. Phys. C 63 (3) (1994) 507–516. doi:10.1007/BF01580331.

[138] D. Stauffer, Scaling theory of percolation clusters, Phys. Rept. 54 (1) (1979) 1–74, sciencedirect:0370157379900607. doi:10.1016/0370-1573(79)90060-7.

[139] S. Kirkpatrick, Percolation and Conduction, Rev. Mod. Phys. 45 (4) (1973) 574–588. doi:10.1103/RevModPhys.45.574.

[140] S. R. Broadbent, J. M. Hammersley, Percolation processes: I. Crystals and mazes, Proc. Cambridge Phil. Soc. 53 (3) (1957) 629–641. doi:10.1017/S0305004100032680.

[141] M. A. Braun, J. Dias de Deus, A. S. Hirsch, C. Pajares, R. P. Scharenberg, B. K. Srivastava, De-confinement and clustering of color sources in nuclear collisions, Phys. Rept. 599 (2015) 1–50. arXiv:1501.01524, doi:10.1016/j.physrep.2015.09.003.

[142] I. Bautista, J. D. de Deus, C. Pajares, Elliptic flow at RHIC and LHC in the string percolation approach, Eur. Phys. J. C 72 (6) (2012) 2038. arXiv:1102.3837, doi:10.1140/epjc/s10052-012-2038-6.

[143] I. Bautista, C. Pajares, J. G. Milhano, J. Dias de Deus, Rapidity dependence of particle densities in pp and AA collisions, Phys. Rev. C 86 (3) (2012) 034909. arXiv:1206.6737, doi:10.1103/PhysRevC.86.034909.

[144] I. Bautista, J. Dias de Deus, C. Pajares, String Percolation and the First LHC Data, Acta Phys. Polon. Supp. 6 (2013) 165–173. doi:10.5506/APhysPolBSupp.6.165.

[145] C. Andrés, M. Braun, C. Pajares, Energy loss as the origin of a universal scaling law of the elliptic flow, Eur. Phys. J. A 53 (3) (2017) 41. arXiv:1609.03927, doi:10.1140/epja/i2017-12226-5.

[146] B. K. Srivastava, Percolation and Deconfinement, Nucl. Phys. A 862-863 (2011) 132–138. arXiv:1102.0754, doi:10.1016/j.nuclphysa.2011.05.031.

[147] R. P. Scharenberg, B. K. Srivastava, A. S. Hirsch, Percolation of color sources and the determination of the equation of state of QGP produced in central Au-Au collisions at $\sqrt{S_{NN}}$= 200-GeV, Eur. Phys. J. C 71 (1) (2011) 1510. arXiv:1006.3260, doi:10.1140/epjc/s10052-010-1510-4.

[148] J. E. Ramírez, B. Díaz, C. Pajares, Interacting color strings as the origin of the liquid behavior of the quark-gluon plasma, Phys. Rev. D 103 (9) (2021) 094029. arXiv:2012.07920, doi:10.1103/PhysRevD.103.094029.

[149] I. Bautista, A. F. Téllez, P. Ghosh, Indication of change of phase in high-multiplicity proton-proton events at LHC in string percolation model, Phys. Rev. D 92 (7) (2015) 071504. arXiv:1509.02278, doi:10.1103/PhysRevD.92.071504.

[150] L. J. Gutay, A. S. Hirsch, C. Pajares, R. P. Scharenberg, B. K. Srivastava, De-Confinement in small systems: Clustering of color sources in high multiplicity $\bar{p}$p collisions at $\sqrt{s}$= 1.8 TeV, Int. J. Mod. Phys. E 24 (12) (2015) 1550101. arXiv:1504.08270, doi:10.1142/S0218301315501013.

[151] R. P. Scharenberg, B. K. Srivastava, C. Pajares, Exploring the initial stage of high multiplicity proton-proton collisions by determining the initial temperature of the quark-gluon plasma, Phys. Rev. D 100 (11) (2019) 114040. arXiv:1803.02301, doi:10.1103/PhysRevD.100.114040.

[152] A. N. Mishra, G. Paić, C. Pajares, R. P. Scharenberg, B. K. Srivastava, Exploring the QGP phase above the deconfinement temperature in pp and $A-A$ collisions at LHC energies (2022). arXiv:2202.12274.

[153] I. Bautista, C. Pajares, J. E. Ramírez, String percolation in AA and p+p collisions, Rev. Mex. Fis. 65 (3) (2019) 197–223. arXiv:1905.06334, doi:10.31349/RevMexFis.65.197.

[154] J. R. A. García, D. R. Herrera, P. Fierro, J. E. Ramírez, A. Fernández Téllez, C. Pajares, Soft and hard scales of the transverse momentum distribution in the Color String Percolation Model (2022). arXiv:2212.10656.

[155] E. G. Ferreiro, F. del Moral, C. Pajares, Transverse momentum fluctuations and percolation of strings, Phys. Rev. C 69 (3) (2004) 034901. arXiv:hep-ph/0303137, doi:10.1103/PhysRevC.69.034901.

[156] J. C. T. García, D. R. Herrera, J. E. Ramírez, A. Fernández Téllez, C. Pajares, Percolation leads to finite-size effects on the transition temperature and center-of-mass energy required for quark-gluon plasma formation, Phys. Rev. D 106 (3) (2022) L031503. arXiv:2208.03769, doi:10.1103/PhysRevD.106.L031503.

[157] J. Dias de Deus, C. Pajares, Percolation of color sources and critical temperature, Phys. Lett. B 642 (5) (2006) 455–458. arXiv:hep-ph/0607101, doi:10.1016/j.physletb.2006.10.018.

[158] UA1 Collaboration, A Study of the General Characteristics of $p\bar{p}$ Collisions at $\sqrt{s}$ = 0.2-TeV to 0.9-TeV, Nucl. Phys. B 335 (2) (1990) 261–287, sciencedirect:055032139090493W. doi:10.1016/0550-3213(90)90493-W.

[159] UA5 Collaboration, UA5: A general study of proton-antiproton physics at $\sqrt{s}$ = 546-GeV, Phys. Rept. 154 (5) (1987) 247–383, sciencedirect:037015738790130X. doi:10.1016/0370-1573(87)90130-X.

[160] STAR Collaboration, Systematic measurements of identified particle spectra in pp, $d+$Au, and Au + Au collisions at the STAR detector, Phys. Rev. C 79 (3) (2009) 034909. arXiv:0808.2041, doi:10.1103/PhysRevC.79.034909.

[161] CDF Collaboration, Pseudorapidity distributions of charged particles produced in $\bar{p}p$ interactions at $\sqrt{s} = 630$ GeV and 1800 GeV, Phys. Rev. D (1989) 119–124doi:10.1103/PhysRevD.41.2330.

[162] ALICE Collaboration, Charged-particle multiplicity measurement in proton-proton collisions at $\sqrt{s} = 0.9$ and 2.36 TeV with ALICE at LHC, Eur. Phys. J. C 68 (1) (2010) 89–108. arXiv:1004.3034, doi:10.1140/epjc/s10052-010-1339-x.

[163] CMS Collaboration, Transverse-momentum and pseudorapidity distributions of charged hadrons in pp collisions at $\sqrt{s} = 0.9$ and 2.36 TeV, J. High Energ. Phys. 02 (2010) 041. arXiv:1002.0621, doi:10.1007/JHEP02(2010)041.

[164] CMS Collaboration, Transverse-Momentum and Pseudorapidity Distributions of Charged Hadrons in pp Collisions at $\sqrt{s} = 7$ TeV, Phys. Rev. Lett. 105 (2) (2010) 022002. arXiv:1005.3299, doi:10.1103/PhysRevLett.105.022002.

[165] ALICE Collaboration, Pseudorapidity and transverse-momentum distributions of charged particles in proton–proton collisions at $\sqrt{s} = 13$ TeV, Phys. Lett. B 753 (2016) 319–329. arXiv:1509.08734, doi:10.1016/j.physletb.2015.12.030.

[166] CMS Collaboration, Pseudorapidity distribution of charged hadrons in proton-proton collisions at $\sqrt{s}$ = 13 TeV, Phys. Lett. B 751 (2015) 143–163. arXiv:1507.05915, doi:10.1016/j.physletb.2015.10.004.

[167] A. Bialas, Fluctuations of string tension and transverse mass distribution, Phys. Lett. B 466 (2) (1999) 301–304. arXiv:hep-ph/9909417, doi:10.1016/S0370-2693(99)01159-4.

[168] A. Di Giacomo, H. Panagopoulos, Field strength correlations in the QCD vacuum, Phys. Lett. B 285 (1) (1992) 133–136, sciencedirect:037026939291311V. doi:10.1016/0370-2693(92)91311-V.

[169] A. Di Giacomo, Extracting physics from lattice artifacts, Acta Phys. Polon. B 25 (1994) 227–244.

[170] G. S. Bali, K. Schilling, C. Schlichter, Observing long color flux tubes in SU(2) lattice gauge theory, Phys. Rev. D 51 (9) (1995) 5165–5198. arXiv:hep-lat/9409005, doi:10.1103/PhysRevD.51.5165.

[171] I. Bautista Guzman, R. Alvarado, P. Fierro, Collectivity in pPb and pp collisions with the string percolation model, PoS ICHEP2016 (2017) 1152. doi:10.22323/1.282.1152.

[172] J. E. Ramírez, A. Fernández Téllez, I. Bautista, String percolation threshold for elliptically bounded systems, Physica A 488 (2017) 8–15. arXiv:1707.06395, doi:10.1016/j.physa.2017.07.002.

[173] J. E. Ramírez, C. Pajares, Area covered by disks in small-bounded continuum percolating systems: An application to the string percolation model, Phys. Rev. E 100 (2) (2019) 022123. arXiv:2004.10067, doi:10.1103/PhysRevE.100.022123.

[174] S. Mertens, C. Moore, Continuum percolation thresholds in two dimensions, Phys. Rev. E 86 (6) (2012) 061109. arXiv:1209.4936, doi:10.1103/PhysRevE.86.061109.

[175] R. P. Scharenberg, B. K. Srivastava, A. S. Hirsch, C. Pajares, Hot Dense Matter: Deconfinement and Clustering of Color Sources in Nuclear Collisions, Universe 4 (9) (2018) 96, MDPI:22181997. doi:10.3390/universe4090096.

[176] STAR Collaboration, Transverse-Momentum and Collision-Energy Dependence of High-p_T Hadron Suppression in Au + Au Collisions at Ultrarelativistic Energies, Phys. Rev. Lett. 91 (17) (2003) 172302. arXiv:nucl-ex/0305015, doi:10.1103/PhysRevLett.91.172302.

[177] ALICE Collaboration, Transverse momentum spectra and nuclear modification factors of charged particles in pp, p-Pb and Pb-Pb collisions at the LHC, J. High Energ. Phys. 2018 (11) (2018) 13. arXiv:1802.09145, doi:10.1007/JHEP11(2018)013.

[178] ALICE Collaboration, Energy dependence of the transverse momentum distributions of charged particles in pp collisions measured by ALICE, Eur. Phys. J. C 73 (12) (2013) 2662. arXiv:1307.1093, doi:10.1140/epjc/s10052-013-2662-9.

[179] ALICE Collaboration, Charged-particle production as a function of multiplicity and transverse spherocity in pp collisions at $\sqrt{s} = 5.02$ and 13 TeV, Eur. Phys. J. C 79 (10) (2019) 857. arXiv:1905.07208, doi:10.1140/epjc/s10052-019-7350-y.

[180] ATLAS Collaboration, Charged-particle distributions in $\sqrt{s}$ = 13 TeV pp interactions measured with the ATLAS detector at the LHC, Phys. Lett. B 758 (2016) 67–88. arXiv:1602.01633, doi:10.1016/j.physletb.2016.04.050.

[181] CMS Collaboration, Study of the inclusive production of charged pions, kaons, and protons in pp collisions at $\sqrt{s} = 0.9, 2.76,$ and 7 TeV, Eur. Phys. J. C 72 (10) (2012) 2164. arXiv:1207.4724, doi:10.1140/epjc/s10052-012-2164-1.

[182] CMS Collaboration, Study of the production of charged pions, kaons, and protons in pPb collisions at $\sqrt{s_{NN}} = 5.02$ TeV, Eur. Phys. J. C 74 (6) (2014) 2847. arXiv:1307.3442, doi:10.1140/epjc/s10052-014-2847-x.

[183] CMS Collaboration, Measurement of charged pion, kaon, and proton production in proton-proton collisions at $\sqrt{s} = 13$ TeV, Phys. Rev. D 96 (11) (2017) 112003. arXiv:1706.10194, doi:10.1103/PhysRevD.96.112003.

[184] D. Chandler, Introduction to Modern Statistical Mechanics, Oxford University Press, New York, 1987.

[185] V. Myroshnychenko, C. Brosseau, Possible manifestation of nonuniversality in some continuum percolation systems, J. Phys. D 41 (9) (2008) 095401. doi:10.1088/0022-3727/41/9/095401.

[186] V. Myroshnychenko, C. Brosseau, Effective complex permittivity and continuum percolation analysis of two-phase composite media, IEEE Trans. Dielectr. Electr. Insul. 16 (4) (2009) 1209–1222. doi:10.1109/TDEI.2009.5211876.

[187] B. I. Halperin, S. Feng, P. N. Sen, Differences between lattice and continuum percolation transport exponents, Phys. Rev. Lett. 54 (22) (1985) 2391–2394. doi:10.1103/PhysRevLett.54.2391.

[188] CMS Collaboration, Centrality dependence of dihadron correlations and azimuthal anisotropy harmonics in PbPb collisions at $\sqrt{s_{NN}} = 2.76$ TeV, Eur. Phys. J. C 72 (5) (2012) 2012. arXiv:1201.3158, doi:10.1140/epjc/s10052-012-2012-3.

[189] PHENIX Collaboration, Creation of quark–gluon plasma droplets with three distinct geometries, Nature Phys. 15 (3) (2019) 214–220. arXiv:1805.02973, doi:10.1038/s41567-018-0360-0.

[190] P. Tribedy, R. Venugopalan, Saturation models of HERA DIS data and inclusive hadron distributions in p+p collisions at the LHC, Nucl. Phys. A 850 (1) (2011) 136–156. arXiv:1011.1895, doi:10.1016/j.nuclphysa.2010.12.006.

[191] P. Tribedy, R. Venugopalan, QCD saturation at the LHC: Comparisons of models to p+p and A+A data and predictions for p+Pb collisions, Phys. Lett. B 710 (1) (2012) 125–133. arXiv:1112.2445, doi:10.1016/j.physletb.2012.02.047.

[192] T. Aste, T. di Matteo, 2 - nanometric architectures: emergence of efficient non-crystalline atomic organization in nanostructures, in: R. Hannink, A. Hill (Eds.), Nanostructure Control of Materials, Woodhead Publishing, 2006, pp. 32–56, sciencedirect:B9781855739338500026. doi:10.1533/9781845691189.32.

[193] J. R. Alvarado García, D. Rosales Herrera, A. Fernández Téllez, B. Díaz, J. E. Ramírez, Structure of the Medium Formed in Heavy Ion Collisions, Universe 9 (6) (2023). arXiv:2305.14860, doi:10.3390/universe9060291.

[194] P. Sahoo, S. K. Tiwari, R. Sahoo, Electrical conductivity of hot and dense QCD matter created in heavy-ion collisions: A color string percolation approach, Phys. Rev. D 98 (5) (2018) 054005. arXiv:1804.07980, doi:10.1103/PhysRevD.98.054005.

[195] P. Sahoo, R. Sahoo, S. K. Tiwari, Wiedemann-Franz law for hot QCD matter in a color string percolation scenario, Phys. Rev. D 100 (5) (2019) 051503. arXiv:1904.06961, doi:10.1103/PhysRevD.100.051503.

[196] Particle Data Group, Review of Particle Physics, Chin. Phys. C 40 (10) (2016) 100001. doi:10.1088/1674-1137/40/10/100001.

[197] J. S. Schwinger, Gauge Invariance and Mass. II., Phys. Rev. 128 (5) (1962) 2425–2429. doi:10.1103/PhysRev.128.2425.

[198] J. Dias de Deus, A. S. Hirsch, C. Pajares, R. P. Scharenberg, B. K. Srivastava, Transport coefficient to trace anomaly in the clustering of color sources approach, Phys. Rev. C 93 (2) (2016) 024915. arXiv:1602.03437, doi:10.1103/PhysRevC.93.024915.

[199] J. Dias de Deus, A. S. Hirsch, C. Pajares, R. P. Scharenberg, B. K. Srivastava, Clustering of color sources and the shear viscosity of the QGP in heavy ion collisions at RHIC and LHC energies, Eur. Phys. J. C 72 (8) (2012) 2123. arXiv:1106.4271, doi:10.1140/epjc/s10052-012-2123-x.

[200] P. Sahoo, S. K. Tiwari, S. De, R. Sahoo, R. P. Scharenberg, B. K. Srivastava, Thermodynamic and transport properties in Au + Au collisions at RHIC energies from the clustering of color strings, Mod. Phys. Lett. A 34 (04) (2019) 1950034. arXiv:1708.06689, doi:10.1142/S0217732319500342.

[201] J. R. A. García, P. Fierro, I. Bautista, A. F. Téllez, Viscosity of non equilibrium hot & dense QCD drop formed at LHC, paper sent to Phys. Rev. D (2023).

[202] A. Bazavov, T. Bhattacharya, M. Cheng, N. H. Christ, C. DeTar, S. Ejiri, S. Gottlieb, R. Gupta, U. M. Heller, K. Huebner, C. Jung, F. Karsch, E. Laermann, L. Levkova, C. Miao, R. D. Mawhinney, P. Petreczky, C. Schmidt, R. A. Soltz, W. Soeldner, R. Sugar, D. Toussaint, P. Vranas, Equation of state and QCD transition at finite temperature, Phys. Rev. D 80 (1) (2009) 014504. arXiv:0903.4379, doi:10.1103/PhysRevD.80.014504.

[203] CMS Collaboration, Evidence for collectivity in pp collisions at the LHC, Phys. Lett. B 765 (2017) 193–220. arXiv:1606.06198, doi:10.1016/j.physletb.2016.12.009.

[204] ATLAS Collaboration, Measurement of multi-particle azimuthal correlations in pp, p+Pb and low-multiplicity Pb+Pb collisions with the ATLAS detector, Eur. Phys. J. C 77 (6) (2017) 428. arXiv:1705.04176, doi:10.1140/epjc/s10052-017-4988-1.

[205] J. E. Bernhard, J. S. Moreland, S. A. Bass, Bayesian estimation of the specific shear and bulk viscosity of quark–gluon plasma, Nature Phys. 15 (11) (2019) 1113–1117. doi:10.1038/s41567-019-0611-8.

[206] H. B. Meyer, Calculation of the shear viscosity in SU(3) gluodynamics, Phys. Rev. D 76 (10) (2007) 101701. arXiv:0704.1801, doi:10.1103/PhysRevD.76.101701.

[207] M. Bluhm, B. Kampfer, K. Redlich, Shear and bulk viscosities of the gluon plasma in a quasiparticle description, Phys. Rev. C 84 (2) (2011) 025201. arXiv:1011.5634, doi:10.1103/PhysRevC.84.025201.

[208] T. Hirano, M. Gyulassy, Perfect fluidity of the quark gluon plasma core as seen through its dissipative hadronic corona, Nucl. Phys. A 769 (2006) 71–94. arXiv:nucl-th/0506049, doi:10.1016/j.nuclphysa.2006.02.005.

[209] HotQCD Collaboration, Equation of state in (2+1)-flavor QCD, Phys. Rev. D 90 (9) (2014) 094503. arXiv:1407.6387, doi:10.1103/PhysRevD.90.094503.

[210] S. Borsanyi, Z. Fodor, C. Hoelbling, S. D. Katz, S. Krieg, K. K. Szabo, Full result for the QCD equation of state with 2+1 flavors, Phys. Lett. B 730 (2014) 99–104. arXiv:1309.5258, doi:10.1016/j.physletb.2014.01.007.

[211] A. D. Gasbarro, Studies of Conformal Behavior in Strongly Interacting Quantum Field Theories, Ph.D. thesis, Yale U. (2019). arXiv:1911.00442.

[212] K. I. Ishikawa, Y. Iwasaki, Y. Nakayama, T. Yoshie, Conformal Behavior in QCD (2013). arXiv:1304.4345.

[213] M. Cheng, S. Ejiri, P. Hegde, F. Karsch, O. Kaczmarek, E. Laermann, R. D. Mawhinney, C. Miao, S. Mukherjee, P. Petreczky, C. Schmidt, W. Soeldner, Equation of state for physical quark masses, Phys. Rev. D 81 (5) (2010) 054504. arXiv:0911.2215, doi:10.1103/PhysRevD.81.054504.

[214] B. K. Srivastava, Percolation approach to initial stage effects in high energy collisions, Nucl. Phys. A 926 (2014) 142–151. arXiv:1402.2306, doi:10.1016/j.nuclphysa.2014.04.029.

[215] T. Schäfer, D. Teaney, Nearly perfect fluidity: from cold atomic gases to hot quark gluon plasmas, Rept. Prog. Phys. 72 (12) (2009) 126001. arXiv:0904.3107, doi:10.1088/0034-4885/72/12/126001.

[216] V. Roy, A. K. Chaudhuri, Bulk viscosity in heavy ion collision (2012). arXiv:1201.4230.

[217] J. E. Parkkila, A. Onnerstad, D. J. Kim, Bayesian estimation of the specific shear and bulk viscosity of the quark-gluon plasma with additional flow harmonic observables, Phys. Rev. C 104 (5) (2021) 054904. arXiv:2106.05019, doi:10.1103/PhysRevC.104.054904.

[218] W.-b. He, G.-y. Shao, X.-y. Gao, X.-r. Yang, C.-l. Xie, Speed of sound in QCD matter, Phys. Rev. D 105 (9) (2022) 094024. arXiv:2205.04614, doi:10.1103/PhysRevD.105.094024.

[219] K. Dusling, T. Schäfer, Bulk viscosity, particle spectra and flow in heavy-ion collisions, Phys. Rev. C 85 (4) (2012) 044909. arXiv:1109.5181, doi:10.1103/PhysRevC.85.044909.

[220] T. Koide, Microscopic formula of transport coefficients for causal hydrodynamics, Phys. Rev. E 75 (6) (2007) 060103. arXiv:nucl-th/0703038, doi:10.1103/PhysRevE.75.060103.

[221] T. Koide, T. Kodama, Transport coefficients of non-Newtonian fluid and causal dissipative hydrodynamics, Phys. Rev. E 78 (5) (2008) 051107. arXiv:0806.3725, doi:10.1103/PhysRevE.78.051107.

[222] T. Koide, E. Nakano, T. Kodama, Shear Viscosity Coefficient and Relaxation Time of Causal Dissipative Hydrodynamics in QCD, Phys. Rev. Lett. 103 (5) (2009) 052301. arXiv:0901.3707, doi:10.1103/PhysRevLett.103.052301.

[223] X.-G. Huang, T. Kodama, T. Koide, D. H. Rischke, Bulk viscosity and relaxation time of causal dissipative relativistic fluid dynamics, Phys. Rev. C 83 (2) (2011) 024906. arXiv:1010.4359, doi:10.1103/PhysRevC.83.024906.

[224] G. S. Denicol, X.-G. Huang, T. Koide, D. H. Rischke, Consistency of field-theoretical and kinetic calculations of viscous transport coefficients for a relativistic fluid, Phys. Lett. B 708 (1) (2012) 174–178. arXiv:1003.0780, doi:10.1016/j.physletb.2012.01.018.

[225] T. Koide, Microscopic derivation of causal diffusion equation using projection operator method, Phys. Rev. E 72 (2) (2005) 026135. arXiv:cond-mat/0501696, doi:10.1103/PhysRevE.72.026135.

[226] X.-G. Huang, T. Koide, Shear viscosity, bulk viscosity, and relaxation times of causal dissipative relativistic fluid-dynamics at finite temperature and chemical potential, Nucl. Phys. A 889 (2012) 73–92. arXiv:1105.2483, doi:10.1016/j.nuclphysa.2012.07.005.

[227] J. Noronha-Hostler, J. Noronha, C. Greiner, Transport Coefficients of Hadronic Matter Near T_c, Phys. Rev. Lett. 103 (17) (2009) 172302. arXiv:0811.1571, doi:10.1103/PhysRevLett.103.172302.

[228] F. Karsch, D. Kharzeev, K. Tuchin, Universal properties of bulk viscosity near the QCD phase transition, Phys. Lett. B 663 (3) (2008) 217–221. arXiv:0711.0914, doi:10.1016/j.physletb.2008.01.080.

[229] G. S. Denicol, T. Kodama, T. Koide, P. Mota, Effect of bulk viscosity on Elliptic Flow near QCD phase transition, Phys. Rev. C 80 (6) (2009) 064901. arXiv:0903.3595, doi:10.1103/PhysRevC.80.064901.

[230] S. Ryu, J. F. Paquet, C. Shen, G. S. Denicol, B. Schenke, S. Jeon, C. Gale, Importance of the Bulk Viscosity of QCD in Ultrarelativistic Heavy-Ion Collisions, Phys. Rev. Lett. 115 (13) (2015) 132301. arXiv:1502.01675, doi:10.1103/PhysRevLett.115.132301.

[231] H. B. Meyer, A Calculation of the bulk viscosity in SU(3) gluodynamics, Phys. Rev. Lett. 100 (16) (2008) 162001. arXiv:0710.3717, doi:10.1103/PhysRevLett.100.162001.

[232] A. Buchel, Bulk viscosity of gauge theory plasma at strong coupling, Phys. Lett. B 663 (3) (2008) 286–289. arXiv:0708.3459, doi:10.1016/j.physletb.2008.03.069.

[233] JETSCAPE Collaboration, Multisystem Bayesian constraints on the transport coefficients of QCD matter, Phys. Rev. C 103 (5) (2021) 054904. arXiv:2011.01430, doi:10.1103/PhysRevC.103.054904.

[234] H. Niemi, K. J. Eskola, R. Paatelainen, Event-by-event fluctuations in a perturbative QCD + saturation + hydrodynamics model: Determining QCD matter shear viscosity in ultrarelativistic heavy-ion collisions, Phys. Rev. C 93 (2) (2016) 024907. arXiv:1505.02677, doi:10.1103/PhysRevC.93.024907.

[235] H. Niemi, K. J. Eskola, R. Paatelainen, K. Tuominen, Predictions for 5.023 TeV Pb + Pb collisions at the CERN Large Hadron Collider, Phys. Rev. C 93 (1) (2016) 014912. arXiv:1511.04296, doi:10.1103/PhysRevC.93.014912.

[236] A. S. Khvorostukhin, V. D. Toneev, D. N. Voskresensky, Viscosity coefficients for hadron and quark–gluon phases, Nucl. Phys. A 845 (1) (2010) 106–146. arXiv:1003.3531, doi:10.1016/j.nuclphysa.2010.05.058.

[237] J. Grefa, M. Hippert, J. Noronha, J. Noronha-Hostler, I. Portillo, C. Ratti, R. Rougemont, Transport coefficients of the quark-gluon plasma at the critical point and across the first-order line, Phys. Rev. D 106 (3) (2022) 034024. arXiv:2203.00139, doi:10.1103/PhysRevD.106.034024.

Monte Carlo study of ion collisions from RHIC to LHC energies

Thesis for the degree of

Doctor of Philosophy (Applied Physics)

by

Jesús Ricardo Alvarado García
219570427

FACULTAD DE CIENCIAS FÍSICO MATEMÁTICAS

BENEMÉRITA UNIVERSIDAD AUTÓNOMA DE PUEBLA